Title

SOME NUCLEAR PROPERTIES OF Bi206, Tl200, Tl201, Tl202, In109, In110m, AND In111 The Nuclear Spins of Bi206, Tl200, Tl201 and Tl202. The Nuclear Spins, Magnetic Dipole, and Electric Quadrupole Interaction Constants of In109, In11Om and In111.

Author

Marino, Lawrence Louis.

Publication Date

1959-04-06

UCRL 8721
C.2

UNIVERSITY OF CALIFORNIA
Ernest O. Lawrence
Radiation Laboratory

SOME NUCLEAR PROPERTIES
Bi^{206}, Tl^{200}, Tl^{201}, Tl^{202}, In^{109}, In^{110m}, AND In^{111}

DISCLAIMER

UCRL-8721
Physics and
Mathematics

UNIVERSITY OF CALIFORNIA

Lawrence Radiation Laboratory
Berkeley, California

Contract No. W-7405-eng-48

SOME NUCLEAR PROPERTIES OF Bi^{206}, Tl^{200}, Tl^{201}, Tl^{202}, In^{109}, In^{110m}, AND In^{111}

The Nuclear Spins of Bi^{206}, Tl^{200}, Tl^{201} and Tl^{202}.

The Nuclear Spins, Magnetic Dipole, and Electric Quadrupole Interaction Constants of In^{109}, In^{110m} and In^{111}.

Lawrence Louis Marino

(Thesis)

April 6, 1959

Printed for the U. S. Atomic Energy Commission

Printed in USA. Price $2.75. Available from the
Office of Technical Services
U.S. Department of Commerce
Washington 25, D. C.

Contents

SOME NUCLEAR PROPERTIES OF Bi^{206}, Tl^{200}, Tl^{201}, Tl^{202}, In^{109}, In^{110m}, AND In^{111}

The Nuclear Spins of Bi^{206}, Tl^{200}, Tl^{201} and Tl^{202}.

The Nuclear Spins, Magnetic Dipole, and Electric Quadrupole Interaction Constants of In^{109}, In^{110m} and In^{111}.

Lawrence Louis Marino

Lawrence Radiation Laboratory and Department of Physics
University of California, Berkeley, California

April 6, 1959

ABSTRACT

The atomic-beam magnetic-resonance flop-in technique using radioactive detection has been employed to measure the nuclear spins of Bi^{206}, Tl^{200}, Tl^{201}, Tl^{202}, In^{109}, In^{110m}, and In^{111}. In addition, the magnetic-dipole and electric-quadrupole interaction constants of In^{109}, In^{110m}, and In^{111} have been determined. The signs of the In^{110m} constants have not been determined. Results are:

Isotope	$t_{1/2}$	I	a (Mc/sec)	b (Mc/sec)
Bi^{206}	6.4 d	6		
Tl^{200}	26.1 hr	2		
Tl^{201}	3.0 d	1/2		
Tl^{202}	12.5 d	2		
In^{109}	4.3 hr	9/2	242.38(56)	462.1(6.4)
In^{110m}	5.0 hr	7	291.4(1.2)	-112(16) for $g_I > 0$
			-301.4(1.3)	120(17) for $g_I < 0$
In^{111}	2.8 d	9/2	241.78(30)	455.3(3.4)

Isotope production took place in the Crocker 60-inch cyclotron. Bismuth was prepared by bombarding lead with deuterons. Thallium was prepared by bombarding mercury with deuterons. Indium was produced by exposing silver to alpha particles.

Chemical separation was employed in all cases to produce a satisfactory atomic beam. Signals were detected by collecting the radioactive atoms on sulfur-coated brass "buttons." These were then placed in scintillation counters containing sodium iodide (thallium-activated) crystals. The counters were adjusted to be most sensitive to the K x-ray emitted following electron capture.

The theory, experimental procedure, and data reduction are presented.

I. THEORY

The techniques of atomic beams, paramagnetic resonance, and microwave spectroscopy as applied to the interaction of the nucleus with the field due to the extra nuclear matter rest upon the following assumptions and properties.[1]

1. The nucleus has a charge Ze and radius $R = r_0 A^{1/3}$.
2. Odd-A nuclei obey Fermi-Dirac statistics (the sign of the wave function of a molecule is reversed if two identical nuclei in the molecule are interchanged).
3. Even-A nuclei obey Einstein-Bose statistics.
4. The nucleus has a spin angular momentum $\vec{M} = \hbar \vec{I}$.
5. The nucleus has a magnetic moment defined by $\vec{I} g_I = \vec{\mu}_I / \mu_0$ and a gyromagnetic ratio defined by $\vec{I} \gamma_I = \vec{\mu}_I / \hbar$. Also $\vec{\mu}_I = \mu_I \vec{I} / I$.
6. Many nuclei have higher-ordered electric and magnetic moments. The highest-ordered moment possible to observe is 2^k, where k = 2I or 2J, whichever is smaller. From parity considerations, odd-k orders are ruled out for electric multipoles and even-k orders are ruled out for magnetic multipoles.

A. Magnetic Dipole Interactions with Internal and External Magnetic Fields

The Hamiltonian is written

$$\mathcal{H} = -\vec{\mu}_I \cdot \vec{B}_J - \vec{\mu}_J \cdot \vec{H}_0 - \vec{\mu}_I \cdot \vec{H}_0 \ , \qquad (1)$$

where $\vec{B}_J$ is the magnetic field at the nucleus due to the external electrons,

$\vec{H}_0$ is the external magnetic field,

$-\vec{\mu}_I \cdot \vec{B}_J$ is the interaction energy of the nucleus with the magnetic field at the nucleus due to the electrons,

$-\vec{\mu}_J \cdot \vec{H}_0$ is the interaction energy of the electronic moment with the external field, and

$-\vec{\mu}_I \cdot \vec{H}_0$ is the interaction energy of the nuclear moment with the external field.

The minus signs are chosen so that the state of lowest energy occurs for the field and moment aligned parallel to each other.

This equation may be rewritten

$$\mathcal{H} = ha\vec{I}\cdot\vec{J} - g_J\mu_0\,\vec{J}\cdot\vec{H}_0 - g_I\mu_0\vec{I}\cdot\vec{H}_0, \tag{2}$$

where $ha = \dfrac{-\mu_I}{I}\,\dfrac{\vec{B}_J\cdot\vec{J}}{\vec{J}\cdot\vec{J}}$ and a is called the interaction constant.

B. Weak External Field

If H_0 is small, the $\vec{I}\cdot\vec{J}$ term in Eq. (2) predominates. $\vec{I}$ and $\vec{J}$ are tightly coupled to form a resultant angular momentum called $\vec{F}$. In this case only the components of $\vec{I}$ and $\vec{J}$ along $\vec{F}$ are effective in their precession about the external field, since the components perpendicular to $\vec{F}$ average to 0 (Fig. 1). We may therefore write Eq. (2) as

$$\mathcal{H} = ha\vec{I}\cdot\vec{J} - g_J\mu_0\left(\frac{\vec{J}\cdot\vec{F}}{|\vec{F}|}\right)\left(\frac{\vec{F}\cdot\vec{H}_0}{|\vec{F}|}\right) - g_I\,\mu_0\left(\frac{\vec{I}\cdot\vec{F}}{|\vec{F}|}\right)\left(\frac{\vec{F}\cdot\vec{H}_0}{|\vec{F}|}\right) \tag{3}$$

In the F, m representation (where m is the projection of F along the field direction), $W(F,m) = \langle Fm|\mathcal{H}|Fm\rangle$, and since

$$\begin{aligned} \vec{F} &= \vec{I} + \vec{J}, \\ I^2 &= F^2 + J^2 - 2\vec{J}\cdot\vec{F}, \\ J^2 &= F^2 + I^2 - 2\vec{I}\cdot\vec{F}, \\ F^2 &= I^2 + J^2 + 2\vec{I}\cdot\vec{J}, \end{aligned} \tag{4}$$

Equation (3) becomes

$$W = ha\left[\frac{F(F+1) - I(I+1) - J(J+1)}{2}\right]$$

$$- \frac{\mu_0 H_0 m}{2F(F+1)}\left[\left\{F(F+1) + J(J+1) - I(I+1)\right\}g_J + \left\{F(F+1) + I(I+1) - J(J+1)\right\}g_I\right] \tag{5}$$

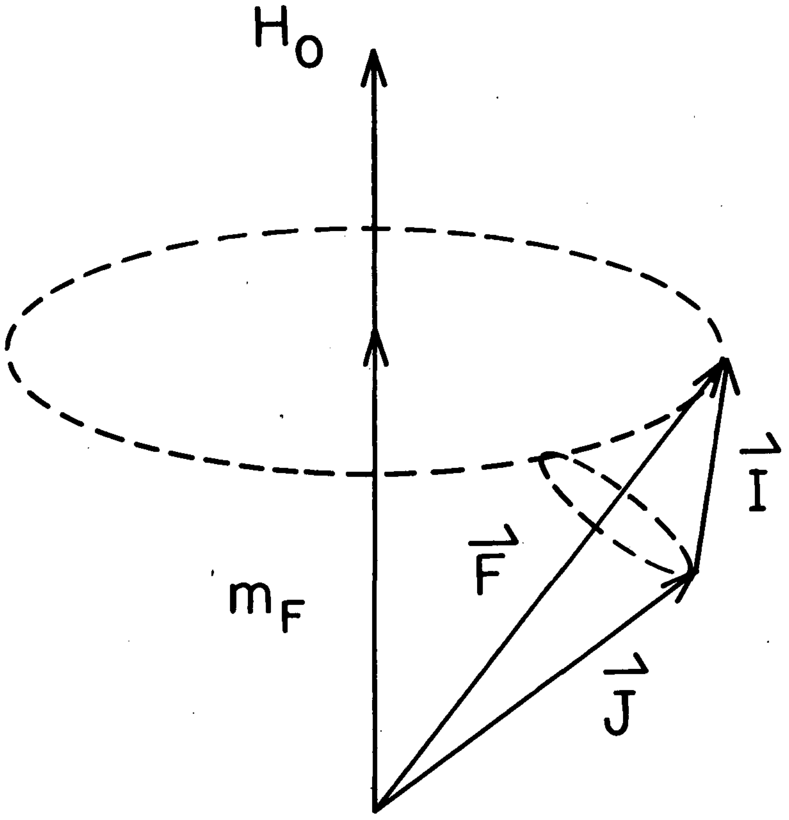

MU-17220

Fig. 1. Weak-field coupling of $\vec{I}$ and $\vec{J}$.

Setting

$$g_F = g_J \left\{\frac{F(F+1)+J(J+1)-I(I+1)}{2F(F+1)}\right\} + g_I \left\{\frac{F(F+1)+I(I+1)-J(J+1)}{2F(F+1)}\right\}, \tag{6}$$

we have

$$W = ha\left\{\frac{F(F+1)-I(I+1)-J(J+1)}{2}\right\} - g_F \mu_0 H_0 m. \tag{7}$$

At $H_0 = 0$ we have

$$\Delta W = h\Delta\nu = W(F) - W(F-1) = haF . \tag{8}$$

This equation is known as the interval rule and $\Delta\nu$ as the hyperfine-structure separation, i. e., the separation of two adjacent F levels at vanishing external magnetic field.

C. Strong External Field

If H_0 is large, $\vec{I}$ and $\vec{J}$ are decoupled and separately precess about H_0. F is no longer a good quantum number, but the projections of $\vec{I}$ and $\vec{J}$ (denoted by m_I and m_J respectively) along the field direction are good quantum numbers (Fig. 2).

The energy is then given approximately by

$$W = \left\langle m_I, m_J \left| \mathcal{H} \right| m_I m_J \right\rangle = ha\, m_I m_J - g_J \mu_0 H_0 m_J - g_I \mu_0 H_0 m_I, \tag{9}$$

where use has been made in the first term of the fact that only I_z and J_z have nonzero diagonal matrix elements.

D. Intermediate Fields

At intermediate fields in general, one cannot select an obvious representation in which the energy matrix is diagonal. If a representation can be found in which the off-diagonal terms are small compared with the diagonal terms, a perturbation technique may be employed. If such a representation cannot be found, then all elements of the matrix must be calculated and the secular equation solved in order to compute the energy levels. In the latter method, solutions may be obtained accurately by high-speed computer techniques. All three methods of solution are illustrated.

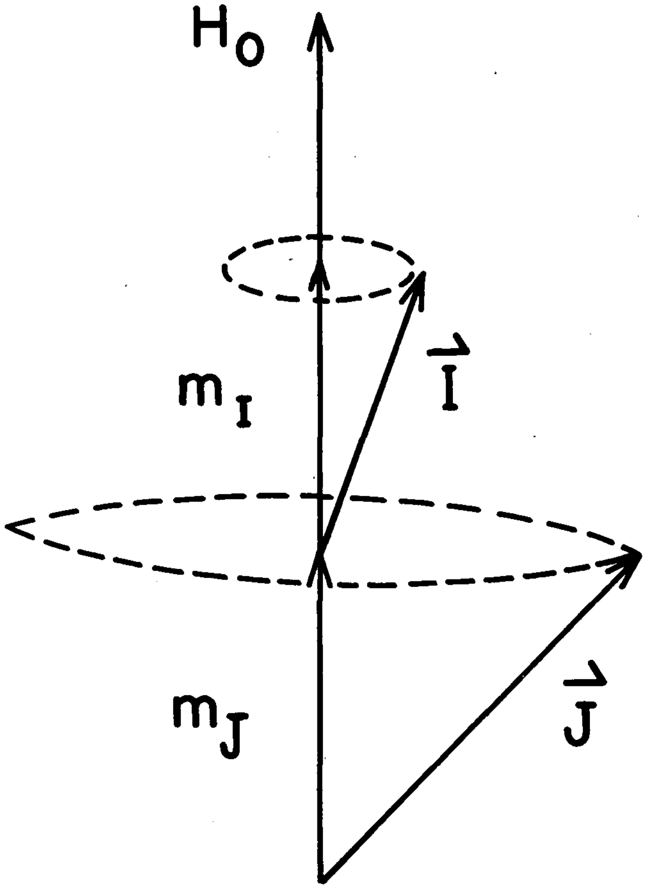

MU-17221

Fig. 2. Strong-field coupling of $\vec{I}$ and $\vec{J}$.

Exact Solution

For the case of J = 1/2, exact solutions of the energy matrix are possible. The Hamiltonian may be placed in the form

$$\mathcal{H} = -d I_z - c\, J_z + ha I_z J_z + 1/2\, ha\, (L_I L_J^* + L_I^* L_J) \tag{10}$$

where

$$\begin{aligned} d &= g_I \mu_0 H_z, & c &= g_J \mu_0 H_z, \\ L_I &= I_x + i\, I_y, & L_I^* &= I_x - i\, I_y, \\ L_J &= J_x + i\, J_y, & L_J^* &= J_x - i J_y . \end{aligned} \tag{11}$$

Since m and H commute, the only nonzero matrix elements that occur in the energy matrix are those having the same m. The energy matrix is given in Fig. 3, where the m_I, m_J representation is used to order the elements. Appendix I contains some properties of matrices of this type. The matrix elements $\langle m_I, m_J | \mathcal{H} | m'_I, m'_J \rangle$ may be calculated by using the relations

$$\begin{aligned} \langle I, m_I - 1 | L_I^* | I, m_I \rangle &= \left[(I + m_I)(I - m_I + 1)\right]^{1/2}, \\ \langle I, m_I + 1 | L_I | I, m_I \rangle &= \left[(I - m_I)(I + m_I + 1)\right]^{1/2}, \\ \langle I, m_I | I_z | I, m_I \rangle &= m_I, \end{aligned} \tag{12}$$

and similarly for J.

Next the matrix is diagonalized and the Breit-Rabi equation results after some manipulation:

$$W(F, m) = - g_I \mu_0 H_0 m - \frac{\Delta W}{2(2I+1)} \pm \frac{\Delta W}{2} \left(1 + \frac{4m}{2I+1} x + x^2\right)^{1/2}, \tag{13}$$

where

$$x = \frac{(g_I - g_J)\, \mu_0 H_0}{\Delta W} .$$

The positive square root in Eq. (13) is associated with the energy level designated by F = I + 1/2, and the negative square root with the energy level designated by F = I - 1/2.

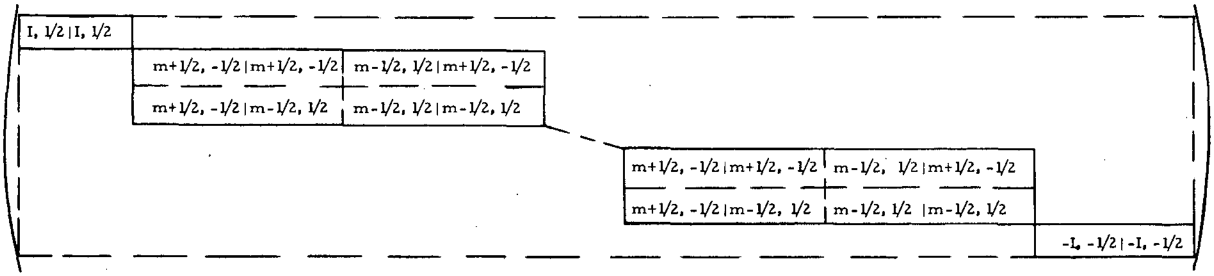

MU-17156

Fig. 3. Energy matrix for $J = 1/2$ in the $m_I m_J$ representation.
The terms are $\langle m_I, m_J \,|\, H \,|\, m_I' \; m_J' \rangle$.

E. Some Properties of the Breit-Rabi Equation

Weak-Field Limit

It may be demonstrated that this equation gives the weak-field expression, Eq. (5) with $F = I \pm 1/2$, by placing it in the form

$$W = -\frac{ha}{4} - g_I \mu_0 m H_0 \pm (A + B H_0 + C H_0^2)^{1/2}, \tag{14}$$

where

$$A = \left(\frac{ha}{2}\right)^2 (I + 1/2)^2,$$

$$B = \frac{h a m}{2} \mu_0 (g_I - g_J),$$

and

$$C = \frac{\mu_0^2}{4} (g_I - g_J)^2,$$

and expanding the radical, retaining only first-order terms in H_0.

Strong-Field Limit

Similarly it may be shown that the Breit-Rabi equation gives the strong-field expression, Eq. (9), by placing it in the form

$$W = -\frac{ha}{4} - g_I \mu_0 (m_I + m_J) H_0 \pm H_0 \left[A + B\left(\frac{1}{H_0}\right) + C\left(\frac{1}{H_0}\right)^2\right]^{1/2}, \tag{15}$$

where

$$A = \frac{\mu_0^2}{4} (g_I - g_J)^2$$

$$B = \frac{ha\,\mu_0}{2} (m_I + m_J)(g_I - g_J),$$

and

$$C = \left(\frac{ha}{2}\right)^2 (I + 1/2)^2.$$

Expanding the radical and retaining only first-order terms in $\left(\frac{1}{H_0}\right)$ results in Eq. (9) with $m_J = \pm 1/2$.

Energy-Level Diagram for I = 1/2, J = 1/2

Some interesting information can be extracted from the Breit-Rabi equation by forming

$$\frac{d(W/\Delta W)}{dx} = -\frac{mg_I}{(g_I - g_J)} \pm \frac{1}{4}\left(1 + \frac{4m}{2I+1}\, x + x^2\right)^{-1/2} \left(\frac{4m}{2I+1} + 2x\right). \qquad (16)$$

Setting Eq. (16) equal to zero, one can observe that for $m = 0$, a minimum occurs at $x = 0$. Also

$$\frac{W}{\Delta W} = + 1/4 \text{ for } F = 1/2 + 1/2 = 1,$$

$$\frac{W}{\Delta W} = - 3/4 \text{ for } F = 1/2 - 1/2 = 0.$$

Linearity of the Highest and Lowest m Levels

For $m = \pm 1$ we have

$$\frac{W}{\Delta W} = \pm \left(1/2 - \frac{g_I}{g_I - g_J}\right) x + 1/4. \qquad (17)$$

It is apparent that for these levels the energies are linear in the magnetic field with slopes of $\pm\left(1/2 - \frac{g_I}{g_I - g_J}\right)$. This is expected since no other levels of the same m exist to perturb the highest and lowest levels.

Slopes of the Levels at Strong Fields

In the Breit-Rabi diagram, where $W/\Delta W$ is plotted against x, it can be shown that at strong fields the slopes of the levels are equal to m_J, the projection of $\vec{J}$ along the field direction.

From the strong-field Eq. (9), the following quantity may be formed:

$$\frac{d(W/\Delta W)}{dx} = ha\, \frac{m_I m_J}{(g_I - g_J)\mu_0 H_0} - \frac{m_J g_J}{g_I - g_J} - \frac{m_I g_I}{g_I - g_J}\ ; \qquad (18)$$

since H_0 is large and $\frac{g_J}{g_I} \approx 2000$,

$$\frac{d(W/\Delta W)}{dx} \approx m_J. \qquad (19)$$

It may also be concluded from Eq. (7) that levels of the same F have equal frequency spacings at low field. All the above features are apparent in the plot of the Breit-Rabi equation for I = 1/2 = J in Fig. 4.

F. Induced Transitions

Under the appropriate conditions, transitions between levels are possible. For reasons to be explained later, transitions between the levels m = -I + 1/2 and m = -I - 1/2, F = I + J are very important. Placing these values in the Breit-Rabi Eq. (13) and subtracting the two energies results in the expression

$$\Delta\nu = \frac{-(h\nu + g_I \mu_0 H_0)(h\nu + g_J \mu_0 H_0)}{h\left[\frac{2H_0\mu_0}{2I+1}(g_J J + g_I I) + h\nu\right]}, \tag{20}$$

where ν is the frequency of the transition between the levels noted.

It is possible to derive an alternate form for the frequency in terms of a series expansion. This is achieved by expanding the radical in the Breit-Rabi equation for each of the levels of interest and subtracting. The result is to third order in field:

$$h\nu = -g_I \mu_0 H_0 + f + \frac{2I}{h\Delta\nu} f^2 + \frac{2I(2I-1)}{(h\Delta\nu)^2} f^3, \tag{21}$$

where

$$f = \frac{\mu_0(g_I - g_J)}{2I+1} H_0.$$

At low fields, this becomes

$$\nu = -\frac{g_J\mu_0}{(2I+1)h} H_0 \approx -\frac{1.4\, g_J}{(2I+1)} H_0 \tag{22}$$

for $g_I \ll g_J$.

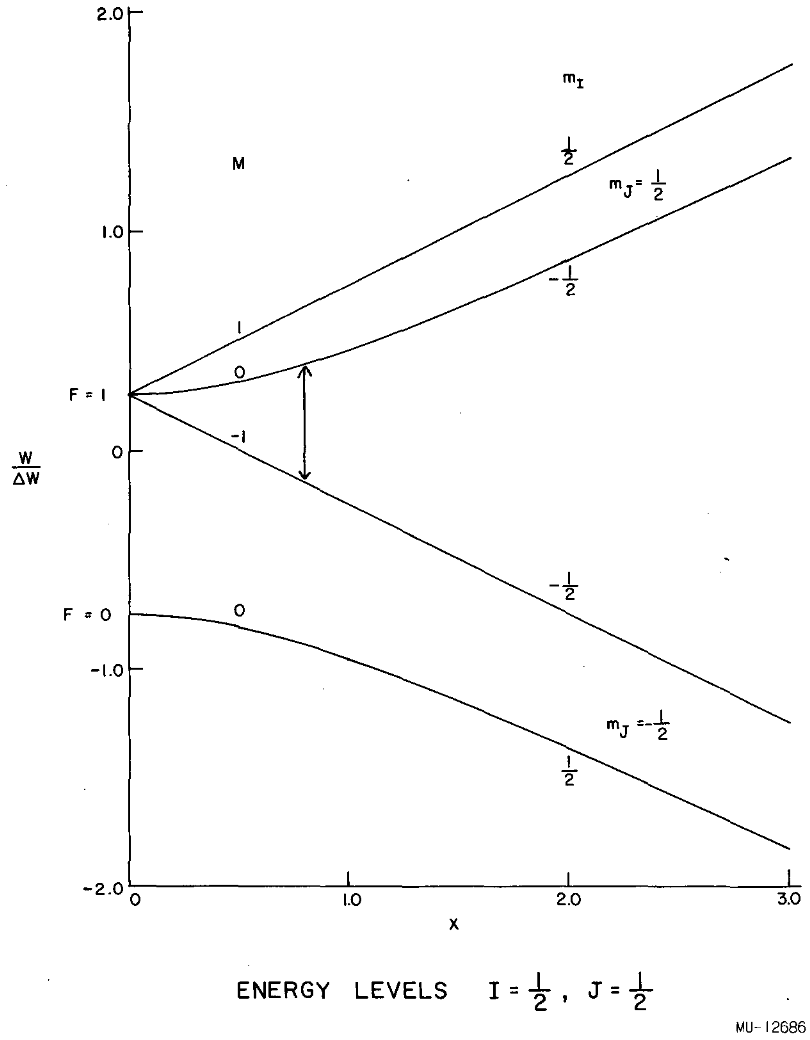

Fig. 4. Breit-Rabi drawing.

For two isotopes having J = 1/2, two conclusions may be drawn from Eq. (22).

(a)
$$\frac{\nu_1}{\nu_2} = \frac{g_{J_1}}{g_{J_2}} \frac{(2I_2+1)}{(2I_1+1)} \tag{23}$$

i. e. at the same magnetic field, the lower spin will be at the higher frequency, assuming the g_J's are comparable.

(b) At the same frequency, the lower spin will be at the lower field, again assuming g_J's are comparable.

$$\frac{H_1}{H_2} = \frac{g_{J_2}}{g_{J_1}} \frac{(2I_1+1)}{(2I_2+1)} \tag{24}$$

Much the same results occur for $J > 1/2$. For this case, the energies at low fields are given by Eq. (7). If a transition among levels characterized by the same F value and $\Delta m = \pm 1$ is assumed, this equation becomes

$$\nu = g_F \frac{\mu_0}{h} H \quad . \tag{25}$$

For J = 3/2 usually transitions occurring in the two largest F levels are of interest.

From Eq. (6)

$$g_F^+ = g_J \frac{3}{2I+3} + g_I \frac{2I}{2I+3} \text{ , where the + stands for } F = I + J;$$

$$(26)$$

$$g_F^- = g_J \frac{2I+9}{(2I+1)(2I+3)} + g_I \frac{2(2I^2+3I-3)}{(2I+1)(2I+3)} \text{ where the - stands for}$$

$F = I + J - 1$

Bearing in mind that $g_I << g_J$, one may draw the same conclusions here as were drawn from Eqs. (23) and (24).

G. Perturbation Calculations

In the case of $J = 3/2$, $I > 1/2$, exact solutions of the secular equation do not exist in general. This problem may be attacked by utilizing a perturbation technique. A treatment up to and including second order was employed with some of the isotopes investigated.

The Hamiltonian used is

$$\mathcal{H} = ha\vec{I}\cdot\vec{J} + hb\left[\frac{3(\vec{I}\cdot\vec{J})^2 + 3/2(\vec{I}\cdot\vec{J}) - I^2J^2}{2I(2I-1)J(2J-1)}\right] - \mu_0 g_J \vec{J}\cdot\vec{H}_0 - \mu_0 g_I \vec{I}\cdot\vec{H}_0, \tag{27}$$

where the second term represents the interaction of the nucleus with the gradient of the electric field at the nucleus due to the electrons. It is called the electric quadrupole interaction energy.

Equation (27) may be split into two parts: A zero-field part $= \mathcal{H}_0$ and a perturbing portion $= \mathcal{H}'$:

$$\left.\begin{aligned} &\mathcal{H} = \mathcal{H}_0 + \mathcal{H}', \\ &\text{where} \\ &\mathcal{H}_0 = ha\vec{I}\cdot\vec{J} + hb\left[\frac{3(\vec{I}\cdot\vec{J})^2 + 3/2(\vec{I}\cdot\vec{J}) - I^2J^2}{2I(2I-1)\,J(2J-1)}\right] \\ &\text{and} \\ &\mathcal{H}' = -\mu_0 g_J \vec{J}\cdot\vec{H}_0 - \mu_0 g_I \vec{I}\cdot\vec{H}_0. \end{aligned}\right\} \tag{28}$$

Choosing the F, m representation to work in, one can write the energy as

$$W = W^0_{Fm} + W^1_{Fm} + W^2_{Fm},$$

where the superscripts refer to the order of the perturbation, and

$$\begin{aligned} W^0_{Fm} &= \langle F, m | \mathcal{H}_0 | F, m \rangle, \\ W^1_{Fm} &= \langle F, m | \mathcal{H}' | F, m \rangle, \\ W^2_{Fm} &= \sum_{F,m}{}' \frac{\langle F, m | \mathcal{H}' | F', m' \rangle \langle F', m' | \mathcal{H}' | F, m \rangle}{W^0_{Fm} - W^0_{F'm'}}. \end{aligned} \tag{29}$$

The prime on the summation sign signifies that states of $F'm' = Fm$ are not permitted in the sum. Were they to occur, the denominator would vanish, making the second-order perturbing energy infinite. A similar consideration results in the "no-m-crossing rule," which states that levels of the same m cannot cross. Furthermore, the matrix elements in W^2_{Fm} are nonzero only for $m = m'$ and $F' = F \pm 1$.

Therefore the sum reduces to only two parts:

$$W^2_{Fm} = \frac{\langle F|\mathcal{H}'|F+1\rangle\langle F+1|\mathcal{H}'|F\rangle}{W_F^0 - W_{F+1}^0} + \frac{\langle F|\mathcal{H}'|F-1\rangle\langle F-1|\mathcal{H}'|F\rangle}{W_F^0 - W_{F-1}^0}. \tag{30}$$

For $J = 3/2$ and $I > J$, four F levels are possible. They are designated as follows:

$$\begin{aligned} &W(4) && F = I + 3/2, \\ &W(3) && F = I + 1/2, \\ &W(2) && F = I - 1/2, \\ &W(1) && F = I - 3/2. \end{aligned} \tag{31}$$

To compute W^0, W^1, and W^2, where the Fm subscripts have been omitted, the following relations are required:

$$\langle F|\vec{I}\cdot\vec{H}_0|F-1\rangle = -H\left[\frac{(F+I+J+1)(I+J+1-F)(F+I-J)(F+J-I)(F^2-m^2)}{4F^2(2F-1)(2F+1)}\right]^{1/2},$$

$$\langle F|\vec{I}\cdot\vec{H}_0|F+1\rangle = -H\left[\frac{(F+I+J+2)(I+J-F)(F+I-J+1)(F+J-I+1)\{(F+1)^2-m^2\}}{4(F+1)^2(2F+1)(2F+3)}\right]^{1/2}$$

$$\langle F|\vec{I}\cdot\vec{H}_0|F-1\rangle = \langle F-1|\vec{I}\cdot\vec{H}_0|F\rangle = -\langle F|\vec{J}\cdot\vec{H}_0|F-1\rangle, \tag{32}$$

and Eq. (4).

Pertinent results are:

$$\left.\begin{aligned}
W^0(4) &= \frac{3}{2}\,haI + \frac{hb}{4}\,, \\
W^0(3) &= \frac{ha(I-3)}{2} - \frac{hb(I+3)}{4I}\,, \\
W^0(2) &= \frac{-ha(I+4)}{2} - \frac{hb(2I+3)(I-2)}{4I(2I-1)}\,, \\
W^0(1) &= -\frac{3(I+1)}{2}\,ha + \frac{(2I+3)(I+1)}{4I(2I-1)}\,hb\,;
\end{aligned}\right\} \qquad (33)$$

$$\left.\begin{aligned}
\frac{W^0(4)-W^0(3)}{h} &= \Delta\nu_{43} = \frac{(2I+3)}{2}\left(a+\frac{b}{2I}\right), \\
\frac{W^0(3)-W^0(2)}{h} &= \Delta\nu_{32} = \frac{(2I+1)}{2}\left[a-\frac{3b}{2I(2I-1)}\right], \\
\frac{W^0(2)-W^0(1)}{h} &= \Delta\nu_{21} = \frac{1}{2}\left[(2I-1)\,a-\frac{(2I+3)}{2I}\,b\right];
\end{aligned}\right\} \qquad (34)$$

$$\frac{W(4)^{m=-I+\frac{1}{2}} - W(4)^{m=-I-\frac{1}{2}}}{h} \equiv \nu_\infty^+ + \delta\nu^+, \quad \text{where}$$

$$\nu_\infty^+ = -\frac{3}{2I+3}\,g_J\,\frac{\mu_0}{h}\,H \quad \text{and} \quad \delta\nu^+ = \frac{2I^2}{3(I+1)}\,\frac{(\nu_\infty^+)^2}{\Delta\nu_{43}}\,,$$

$$\frac{W(3)^{m=-I+3/2} - W(3)^{m=-I+1/2}}{h} \equiv \nu_\infty^- + \delta\nu^-, \quad \text{where} \qquad (35)$$

$$\nu_\infty^- = -\frac{(2I+9)g_J\,\mu_0}{(2I+3)(2I+1)h}\,H \quad \text{and} \quad \delta\nu^- = \frac{2(I-1)(\nu_\infty^-)^2}{(I+1)(2I+9)^2}\left[-\frac{3I(2I+1)^2}{\Delta\nu_{43}}+\frac{(2I-1)(2I+3)^3}{I\quad\Delta\nu_{32}}\right].$$

The results of this perturbation calculation are generally useful for regions immediately above that covered by the low-field expressions. The frequencies predicted for the two transitions rapidly become inaccurate because of the effect of neglecting the higher-ordered terms. For two isotopes studied, it was observed that at a frequency of about 100 Mc/sec the perturbation calculation to second order predicted a frequency 1 Mc/sec lower than the more exact method outlined below.

H. Numerical Methods

Two programs utilizing the IBM 653 high-speed computer were constructed by Professor W. A. Nierenberg in order to permit more accurate analysis of experimental results. The following information is abstracted from Professor Nierenberg's program guides.[2]

The first program discussed computes improved values of a and b (see Eq. (27)), the uncertainties in each, the χ^2 of fit, and the quantity $(X_1 - X_2) - f$, where $X_1 - X_2$ is computed by the program and f is the input frequency. The input data are the frequency f of a transition observed; the magnetic field $H' = (-g_J + g_I)\frac{\mu_0}{h} H$; m_1, m_2; the energy levels X_1, X_2; and the statistical weight $w = \frac{1}{(\Delta f)^2 + \left(\frac{\partial f}{\partial H}\right)^2 (\Delta H)^2}$. Further Δf is the uncertainty of the resonance peak, $\frac{\partial f}{\partial H}$ is the variation of frequency with magnetic field (estimated from the second program to be described), and ΔH is the estimated uncertainty of the magnetic field, computed from the estimated uncertainty in the calibration frequency (to be described later).

The Hamiltonian used is a slightly different form of Eq. (27):

$$\mathcal{H} = a\vec{I} \cdot \vec{J} + b\,\frac{3(\vec{I} \cdot \vec{J})^2 + 3/2(\vec{I} \cdot \vec{J}) - I(I+1)J(J+1)}{2I(2I-1)\quad J(2J-1)} + H' J_z - \frac{g_I \mu_0}{h}\, H m. \tag{36}$$

The program does not include the g_I term. It is a correction to be considered separately.

The following relations already exhibited must be used to compute the matrix elements involved:

$$\left.\begin{aligned} \langle F, m | \vec{I} \cdot \vec{J} | F, m \rangle &\equiv a_p \\ \langle F, m | J_z | F, m \rangle &\equiv c_p \end{aligned}\right\} \text{(see Eq. (4) for the explicit form),} \tag{37}$$

$$\langle F, m | J_z | F+1, m \rangle \equiv d_p \quad \text{(see Eq. (32) for the explicit form).}$$

One further relation is required:

$$\langle F, m | Q | F, m \rangle = \{3/4 [F(F+1) - I(I+1) - J(J+1)][F(F+1) - I(I+1) - J(J+1) + 1] - I(I+1)J(J+1)\} \frac{1}{2I(2I-1)J(2J-1)} \equiv b_p, \quad (38)$$

where Q is written for the coefficient of b in Eq. (36).

As an example, consider the case in which J = 3/2 and I is arbitrary. The matrix involved is shown in Fig. 5, where submatrices are illustrated only up to the point of repetition. If, in addition, we specify I, the entire matrix may be drawn. Figure 6 illustrates the case for I = 5/2, J = 3/2. For further facts about these matrices, see Appendix I.

From Eqs. (36), (37), and (38), we observe that the diagonal elements of the matrix may be written

$$A_p = a\, a_p + b\, b_p + H' \, c_p, \quad (39)$$

and the elements one off the diagonal (the only nonvanishing ones),

$$E_p \equiv e_p^2 = (H')^2 \, d_p. \quad (40)$$

These quantities were evaluated for J = 3/2, I arbitrary, and are listed below:

$$\left.\begin{aligned} a_4 &= 3/2\, I \\ a_3 &= 1/2\, (I-3) \\ a_2 &= -1/2\, (I+4) \\ a_1 &= -3/2\, (I+1) \end{aligned}\right\} \quad (41)$$

$$\left.\begin{aligned} b_4 &= 1/4 \\ b_3 &= \frac{-(I+3)}{4I} \\ b_2 &= \frac{-(2I+3)(I-2)}{4I(2I-1)} \\ b_1 &= \frac{(I+1)(2I+3)}{4I\,(2I-1)} \end{aligned}\right\} \quad (42)$$

	m	I + 3/2	I + 1/2		I - 1/2			I - 3/2			
m'	F' \ F	I + 3/2	I + 1/2	I + 3/2	I - 1/2	I + 1/2	I + 3/2	I - 3/2	I - 1/2	I + 1/2	I + 3/2
I+3/2	I + 3/2	I+3/2, I+3/2									
I+1/2	I + 1/2		I+1/2, I+1/2	I+3/2, I+1/2							
	I + 3/2		I+1/2, I+3/2	I+3/2, I+3/2							
I-1/2	I - 1/2				I-1/2, I-1/2	I+1/2, I-1/2					
	I + 1/2				I-1/2, I+1/2	I+1/2, I+1/2	I+3/2, I+1/2				
	I + 3/2					I+1/2, I+3/2	I+3/2, I+3/2				
I-3/2	I - 3/2							I-3/2, I-3/2	I-1/2, I-3/2		
	I - 1/2							I-3/2, I-1/2	I-1/2, I-1/2	I+1/2, I-1/2	
	I + 1/2								I-1/2, I+1/2	I+1/2, I+1/2	I+3/2, I+1/2
	I + 3/2									I+1/2, I+3/2	I+3/2, I+3/2

MU-17152

Fig. 5. Energy matrix for J = 3/2, I arbitrary. Elements are $\langle F, m | H | F' m' \rangle$, where F and F' are indicated in the submatrices. Only submatrices up to the point of repetition are presented.

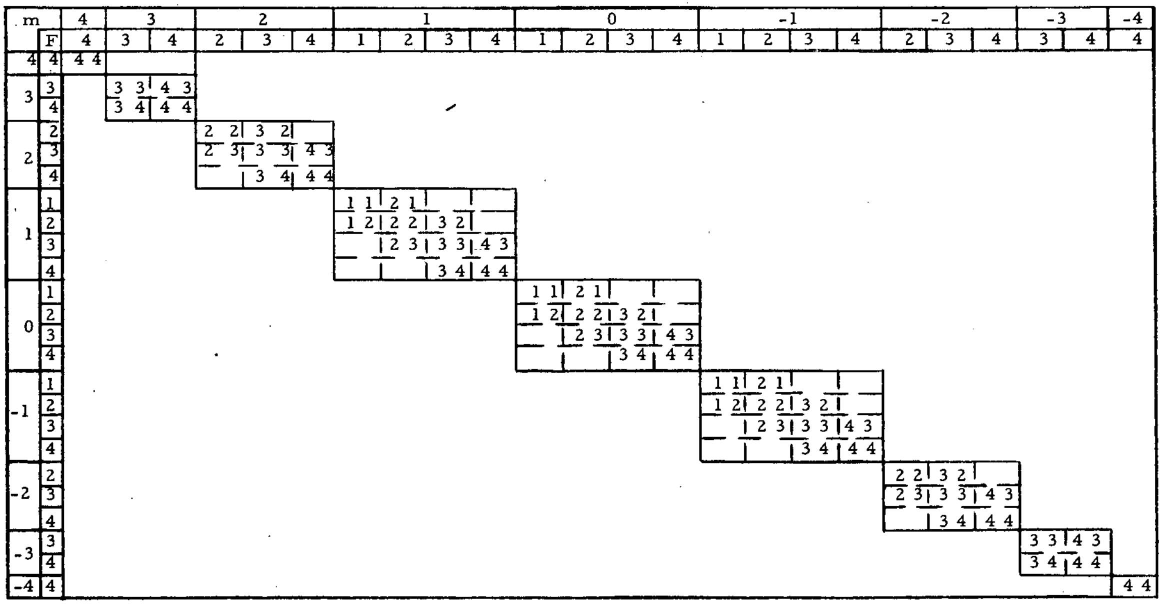

MU-17153

Fig. 6. Energy matrix for I = 5/2, J = 3/2 in the Fm representation. F values are indicated in the submatrices.

$$\left.\begin{aligned} c_4 &= \frac{3}{2I+3}\; m \\ c_3 &= \frac{(2I+9)}{(2I+1)\,(2I+3)}\; m \\ c_2 &= \frac{-\,(2I-7)}{(2I-1)\,(2I+1)}\; m \\ c_1 &= -\frac{3}{(2I-1)}\; m \end{aligned}\right\} \tag{43}$$

$$\left.\begin{aligned} d_3 &= \frac{3I}{4(I+1)} \left[1 - \frac{4m^2}{(2I+3)^2}\right] \\ d_2 &= \frac{(2I-1)\,(2I+3)}{4I(I+1)} \left[1 - \frac{4m^2}{(2I+1)^2}\right] \\ d_1 &= \frac{3(I+1)}{4I} \left[1 - \frac{4m^2}{(2I-1)^2}\right] \end{aligned}\right\} \tag{44}$$

$$\left.\begin{aligned} A_4 &= \frac{3}{2}\, I\, a + \frac{1}{4}\, b + \frac{3}{(2I+3)}\; H'm \\ A_3 &= \frac{(I-3)}{2}\, a - \frac{(I+3)}{4I}\, b + \frac{(2I+9)}{(2I+1)(2I+3)}\; H'm \\ A_2 &= -\frac{(I+4)}{2}\, a - \frac{(2I+3)(I-2)}{4I(2I-1)}\, b - \frac{(2I-7)}{(2I-1)(2I+1)}\; H'm \\ A_1 &= -\frac{3}{2}\,(I+1)\, a + \frac{(I+1)(2I+3)}{4I(2I-1)}\, b - \frac{3}{(2I-1)}\; H'm \end{aligned}\right\} \tag{45}$$

$$\left.\begin{aligned} e_3 &= \sqrt{E_3} = \left\{\frac{3I}{4(I+1)} \left[1 - \frac{4m^2}{(2I+3)^2}\right]\right\}^{1/2} H' \\ e_2 &= \sqrt{E_2} = \left\{\frac{(2I-1)(2I+3)}{4I(I+1)} \left[1 - \frac{4m^2}{(2I+1)^2}\right]\right\}^{1/2} H' \\ e_1 &= \sqrt{E_1} = \left\{\frac{3(I+1)}{4I} \left[1 - \frac{4m^2}{(2I-1)^2}\right]\right\}^{1/2} H' \end{aligned}\right\} \tag{46}$$

The positions of the elements in the largest submatrix are shown in Fig. 7, where the meanings of the subscripts are indicated by the same ordering as in Figs. 5 and 6. In addition, the eigenvalue X that diagonalizes the matrix has been included.

The determinant D_n is defined as $D_n = |H_n - 1X|$, where H_n is the submatrix in question. It may be evaluated by the method of cofactors:

$$D_4 = (A_4 - X)\begin{vmatrix} A_1 - X & e_1 & 0 \\ e_1 & A_2 - X & e_2 \\ 0 & e_2 & A_3 - X \end{vmatrix} - e_3 \begin{vmatrix} A_1 - X & e_1 & 0 \\ e_1 & A_2 - X & e_2 \\ 0 & 0 & e_3 \end{vmatrix}, \quad (47)$$

$$D_4 = (A_4 - X) D_3 - E_3 \begin{vmatrix} A_1 - X & e_1 \\ e_1 & A_2 - X \end{vmatrix}, \quad (48)$$

$$D_4 = (A_4 - X)\, D_3 - E_3 D_2. \quad (49)$$

In general,

$$D_p = (A_p - X)\, D_{p-1} - E_{p-1} D_{p-2}, \quad (50)$$

where $D_0 = 1$, $E_0 = 0$ and $D_{-1} = 0$.

The problem then is to solve for X from the equation

$$D_p(a, b, X) = 0. \quad (51)$$

Newton's method is used. Initial values of a and b must be given, plus trial values of X (to aid in the root identification). An improved value of X is given by

$$X' = X - \delta X, \quad (52)$$

where δX is computed from

$$D_p(a, b, X) = \frac{\partial D_p(a, b, X)}{\partial X} \quad \delta X \quad (53)$$

$$\begin{array}{|c|c|c|c|}
\hline
A_1-X & e_1 & & \\
\hline
e_1 & A_2-X & e_2 & \\
\hline
 & e_2 & A_3-X & e_3 \\
\hline
 & & e_3 & A_4-X \\
\hline
\end{array}$$

MU-17222

Fig. 7. The largest submatrix for J = 3/2.

and $\frac{\partial D_p}{\partial X}$ is obtained from Eq. (50), as follows:

$$\frac{\partial D_p}{\partial X} \doteq (A_p - X) \frac{\partial D_{p-1}}{\partial X} - E_{p-1} \frac{\partial D_{p-2}}{\partial X} - D_{p-1}. \tag{54}$$

This procedure is repeated until the improved value of X approaches the exact value within the desired accuracy (nominally 0.001 Mc/sec.). Once the energy of each level desired has been computed to the desired accuracy, the second part of the problem is undertaken. The task then is to find the minimum of the function

$$N = \sum_i \left\{ f^i - (X_1^{\,i} - X_2^{\,i}) \right\}^2 w_i, \tag{55}$$

where f^i is the frequency observed at the ith observation.

The procedure chosen is a quadratic method for minimizing a function of n variables.[3] In its general form, the function to be minimized is

$$f = \sum_{a=1}^{m} \left[M_a - f_a(x_i) \right]^2 p_a, \tag{56}$$

where p_a is the statistical weight of the ath measure M_a. If the x_i are trial values, then the next improved trial values are

$$x_i' = x_i - dx_i, \tag{57}$$

where the dx_i are solutions of the linear equations;

$$\sum_{i=1}^{n} \frac{\partial^2 f}{\partial x_i \partial x_j} dx_i = \frac{\partial f}{\partial x_j} \tag{58}$$

where the $\frac{\partial^2 f}{\partial x_i \partial x_j}$ form a matrix G of which the elements are

$$G_{ij} = \frac{\partial^2 f}{\partial x_i \partial x_j} \quad . \tag{59}$$

The standard deviation of x_i' about its minimum value x_i^0 is

$$\overline{(\Delta x'_i)^2} = \frac{\Delta_{ii}}{G}\,, \tag{60}$$

where Δ_{ij} is the cofactor of G_{ij}. This method is employed in preference to the more usual linear method since it is capable of convergence over a wide range of parameters, whereas the latter method does not guarantee convergence in all cases.

Applying Eqs. (57), (58), and (59) to Eq. (55), we arrive at the expressions

$$\left.\begin{aligned} a' &= a - \delta a, \\ b' &= b - \delta b, \end{aligned}\right\} \tag{61}$$

where δa and δb are given from the solution of

$$\left.\begin{aligned} \frac{\partial^2 N}{\partial a^2}\,\delta a + \frac{\partial^2 N}{\partial a \partial b}\,\delta b &= \frac{\partial N}{\partial a}\,, \\ \frac{\partial^2 N}{\partial b \partial a}\,\delta a + \frac{\partial^2 N}{\partial b^2}\,\delta b &= \frac{\partial N}{\partial b}, \end{aligned}\right\} \tag{62}$$

$$\left.\begin{aligned} \overline{(\Delta a')^2} &= \frac{\dfrac{\partial^2 N}{\partial a^2}}{G}\,, \\ \overline{(\Delta b')^2} &\quad \frac{\dfrac{\partial^2 N}{\partial a^2}}{G}\,, \end{aligned}\right\} \tag{63}$$

where

$$G = \begin{vmatrix} \dfrac{\partial^2 N}{\partial a^2} & \dfrac{\partial^2 N}{\partial a \partial b} \\ \dfrac{\partial^2 N}{\partial b \partial a} & \dfrac{\partial^2 N}{\partial b^2} \end{vmatrix}. \tag{64}$$

The derivatives appearing in Eq. (62) may be placed in the form

$$\frac{\partial N}{\partial a} = 2 \sum_i (f^i - X_1^i + X_2^i) \left(- \frac{\partial X_1^i}{\partial a} + \frac{\partial X_2^i}{\partial a} \right) w_i \,, \tag{65}$$

$$\frac{\partial N}{\partial b} = 2 \sum_i (f^i - X_1^i + X_2^i) \left(- \frac{\partial X_1^i}{\partial b} + \frac{\partial X_2^i}{\partial b} \right) w_i \tag{66}$$

$$\frac{\partial^2 N}{\partial a^2} = 2 \sum_i \left[(f^i - X_1^i + X_2^i) \left(- \frac{\partial^2 X_1^i}{\partial a^2} + \frac{\partial^2 X_2^i}{\partial a^2} \right) + \left(- \frac{\partial X_1^i}{\partial a} + \frac{\partial X_2^i}{\partial a} \right)^2 \right] w_i \tag{67}$$

$$\frac{\partial^2 N}{\partial b^2} = 2 \sum_i \left[(f^i - X_1^i + X_2^i) \left(- \frac{\partial^2 X_1^i}{\partial b^2} + \frac{\partial^2 X_2^i}{\partial b^2} \right) + \left(- \frac{\partial X_1^i}{\partial b} + \frac{\partial X_2^i}{\partial b} \right)^2 \right] w_i \tag{68}$$

$$\begin{aligned} \frac{\partial^2 N}{\partial b \partial a} &= 2 \sum_i \left[(f^i - X_1^i + X_2^i) \left(- \frac{\partial^2 X_1^i}{\partial b \partial a} + \frac{\partial^2 X_2^i}{\partial b \partial a} \right) + \right. \\ &\qquad \left. \left(- \frac{\partial X_1^i}{\partial a} + \frac{\partial X_2^i}{\partial a} \right) \left(- \frac{\partial X_1^i}{\partial b} + \frac{\partial X_2^i}{\partial b} \right) \right] w_i \\ &= \frac{\partial^2 N}{\partial a \partial b} \; . \end{aligned} \tag{69}$$

The derivatives on the right-hand side of Eqs. (65) through (69) are written as

$$\frac{\partial X}{\partial a} = - \frac{\dfrac{\partial D_n}{\partial a}}{\dfrac{\partial D_n}{\partial X}} \; ; \tag{70}$$

$$\frac{\partial X}{\partial b} = - \frac{\dfrac{\partial D_n}{\partial b}}{\dfrac{\partial D_n}{\partial X}} \; ; \tag{71}$$

$$\frac{\partial^2 X}{\partial a^2} = - \frac{\dfrac{\partial^2 D_n}{\partial a^2} + \dfrac{\partial^2 D_n}{\partial X \partial a} \dfrac{\partial X}{\partial a}}{\dfrac{\partial D_n}{\partial X}} + \frac{\dfrac{\partial D_n}{\partial a} \left(\dfrac{\partial^2 D_n}{dX^2} \dfrac{\partial X}{\partial a} + \dfrac{\partial^2 D_n}{\partial a \partial X} \right)}{\left(\dfrac{\partial D_n}{\partial X} \right)^2} \; ; \tag{72}$$

$$\frac{\partial^2 X}{\partial b^2} = - \frac{\dfrac{\partial^2 D_n}{\partial b^2} + \dfrac{\partial^2 D_n}{\partial X \partial b} \dfrac{\partial X}{\partial b}}{\dfrac{\partial D_n}{\partial X}} + \frac{\dfrac{\partial D_n}{\partial b} \left(\dfrac{\partial^2 D_n}{\partial X^2} \dfrac{\partial X}{\partial b} + \dfrac{\partial^2 D_n}{\partial b \partial X} \right)}{\left(\dfrac{\partial D_n}{\partial X} \right)^2} \; ; \tag{73}$$

$$\frac{\partial^2 X}{\partial a \partial b} = - \frac{\dfrac{\partial^2 D_n}{\partial a \partial b} + \dfrac{\partial^2 D_n}{\partial X \partial b} \dfrac{\partial X}{\partial a}}{\dfrac{\partial D_n}{\partial X}} + \frac{\dfrac{\partial D_n}{\partial b} \left(\dfrac{\partial^2 D_n}{\partial X^2} \dfrac{\partial X}{\partial a} + \dfrac{\partial^2 D_n}{\partial a \partial X} \right)}{\left(\dfrac{\partial D_n}{\partial X} \right)^2} \; . \tag{74}$$

The quantities on the right-hand side of Eqs. (70) through (74) may be computed from the matrix already treated in the first part of the program in the following way:

$$\frac{\partial D_p}{\partial X} = (A_p - X) \frac{\partial D_{p-1}}{\partial X} - E_{p-1} \frac{\partial D_{p-2}}{\partial X} - D_{p-1}; \tag{75}$$

$$\frac{\partial^2 D_p}{\partial X^2} = (A_p - X) \frac{\partial^2 D_{p-1}}{\partial X^2} - E_{p-1} \frac{\partial^2 D_{p-2}}{\partial X^2} - 2 \frac{\partial D_{p-1}}{\partial X} ; \tag{76}$$

$$\frac{\partial D_p}{\partial a} = (A_p - X) \frac{\partial D_{p-1}}{\partial a} - E_{p-1} \frac{\partial D_{p-2}}{\partial a} + a_p D_{p-1}; \tag{77}$$

$$\frac{\partial D_p}{\partial b} = (A_p - X) \frac{\partial D_{p-1}}{\partial b} - E_{p-1} \frac{\partial D_{p-2}}{\partial b} + b_p D_{p-1}; \tag{78}$$

$$\frac{\partial^2 D_p}{\partial a^2} = (A_p - X) \frac{\partial^2 D_{p-1}}{\partial a^2} - E_{p-1} \frac{\partial^2 D_{p-2}}{\partial a^2} + 2a_p \frac{\partial D_{p-1}}{\partial a} ; \tag{79}$$

$$\frac{\partial^2 D_p}{\partial b^2} = (A_p - X) \frac{\partial^2 D_{p-1}}{\partial b^2} - E_{p-1} \frac{\partial^2 D_{p-2}}{\partial b^2} + 2b_p \frac{\partial D_{p-1}}{\partial b}; \tag{80}$$

$$\frac{\partial^2 D_p}{\partial a \partial b} = (A_p - X) \frac{\partial^2 D_{p-1}}{\partial a \partial b} - E_{p-1} \frac{\partial^2 D_{p-2}}{\partial a \partial b} + a_p \frac{\partial D_{p-1}}{\partial b} + b_p \frac{\partial D_{p-1}}{\partial a} ; \tag{81}$$

$$\frac{\partial^2 D_p}{\partial a \partial X} = (A_p - X) \frac{\partial^2 D_{p-1}}{\partial a \partial X} - E_{p-1} \frac{\partial^2 D_{p-2}}{\partial a \partial X} - \frac{\partial D_{p-1}}{\partial a} + a_p \frac{\partial D_{p-1}}{\partial X} ; \tag{82}$$

$$\frac{\partial^2 D_p}{\partial b \partial X} = (A_p - X) \frac{\partial^2 D_{p-1}}{\partial b \partial X} - E_{p-1} \frac{\partial^2 D_{p-2}}{\partial b \partial X} - \frac{\partial D_{p-1}}{\partial b} + b_p \frac{\partial D_{p-1}}{\partial X} . \tag{83}$$

Thus, to summarize, the program first diagonalizes the energy matrix using given values of a and b, plus a starting value for X. It then uses this improved eigenvalue to compute the derivatives (all of which are calculated numbers) to determine improved values of a and b with their associated uncertainties. The starting value for the energy levels are obtained from the second program.

The second program computes the frequency of a desired transition for a number of magnetic fields, the energy levels from which the frequency is derived, the frequency divided by the field, and the variation of the frequency with field at the magnetic fields chosen. The input information required is I, J, F_1, m_1, F_2, m_2, b/a, and the field steps to be taken, Δh.

The Hamiltonian is that of Eq. (36) divided by a,

$$\mathcal{H} = \vec{I} \cdot \vec{J} + \frac{b}{a} \left[\frac{3(\vec{I} \cdot \vec{J})^2 + 3/2\,(\vec{I} \cdot \vec{J}) - I(I+1)J(J+1)}{2I(2I-1)\,J(2J-1)} \right] + H' J_z - g_I \frac{\mu_0}{ah} Hm, \tag{84}$$

where

$$H' = \frac{(-g_J + g_I)\mu_0}{ah} H,$$

and again the g_I terms are neglected. The calculation proceeds as in the first part of the first program. In addition the quantity

$$\frac{\partial D_p}{\partial H'} = (A_p - X) \frac{\partial D_{p-1}}{\partial H'} - (E_p)^2 \frac{\partial D_{p-2}}{\partial H'} + c_p D_{p-1} - 2H' d_{p-1} D_{p-2} \tag{85}$$

is calculated in order to compute the statistical weight for the first program, since

$$\frac{\partial f}{\partial H} = \frac{\partial (X_1 - X_2)}{\partial H},$$

where

$$\frac{\partial X}{\partial H} = - \frac{\dfrac{\partial D_n}{\partial H}}{\dfrac{\partial D_n}{\partial X}} \quad .$$

The X and H' are dimensionless. No starting value is needed for X. Since the program starts at magnetic field equal to zero, root identification is not difficult, provided small steps are taken (initially at least) in magnetic field.

The second program is used to predict the frequency at which a particular resonance will occur and to give input information to the first program. The first program is used to calculate improved values of a and b and to see how well the experimental data fit the functional form assumed. This is measured by χ^2, the value of Eq. (55) at minimum.

To Make g_I Corrections to the Second Program

1. Enter the field table with
$$H' = \frac{(-g_J + g_I)}{ha} \mu_0 H.$$

2. Extract the dimensionless frequency and convert to Mc/sec by multiplying by a.

3. Apply the correction $\frac{g_I \mu_0}{h} H(m_1 - m_2)$, with the correct sign to arrive at the predicted frequency (for $g_I > 0$,
$$\nu_{\text{predicted}} = \nu_{\text{program}} - \frac{g_I \mu_0}{h} H[m_1 - m_2]) \quad .$$

To Make g_I Corrections to the First Program

1. Form $\nu_{\text{program}} = \nu_{\text{observed}} + \frac{g_I \mu_0}{h} H(m_1 - m_2)$ (for $g_I > 0$).

2. Form $H' = \frac{(-g_J + g_I)}{h} \mu_0 H.$

3. Use starting values of X_1 and X_2 calculated from the second program, assuming $g_I > 0$ and $g_I < 0$.

If in a region of high enough field, the χ^2 of fit will indicate which set of data fits best, $g_I > 0$ or $g_I < 0$.

I. Zero-Field Level Sequences

Up to this point, the energy levels have been assumed to be in normal order at vanishing magnetic field. This is for $J = 3/2$, in order of decreasing energy $F = I + 3/2$, $I + 1/2$, $I - 1/2$, $I - 3/2$. This sequence can be inverted if the nuclear moment is negative, i. e., $F = I - 3/2$, $I - 1/2$, $I + 1/2$, $I + 3/2$. Regardless of the sign of the nuclear moment, it is even possible for these levels to lie in almost any given order. The ordering at zero magnetic field is determined by the sign and magnitude of the ratio $b/a = \xi$. From Eq. (33) it is possible to determine the value of ξ at which any two levels will cross. Table I presents the level ordering for each of the critical values of ξ for $J = 3/2$, $I \geq 3/2$. The two levels crossing are indicated at the top of each column. The value of ξ at which the crossover occurs is listed next. Finally, the complete ordering is given between this critical point and the next.

Table II lists the exact value of ξ and the energy at which levels cross for $I = 3/2$ to $I = 9$, where the energy is written as $W' = W/ha$. Figures A1 through A16 (Appendix II) present the information of Table II in graphic form. The intersections are given to the nearest tenth in ξ and W'.

Table I

Zero-field level sequences at critical values of ξ

$W_{nm} = 0$	W_{42}	W_{43}	Normal order	W_{21}	W_{31}	W_{32}	W_{41}
ξ	$-\frac{4I(2I-1)}{2I-3}$	$-2I$	0	$\frac{2I(2I-1)}{2I+3}$	$\frac{4I(2I-1)}{2I+5}$	$\frac{2I(2I-1)}{3}$	$2I(2I-1)$
F level sequence	$I+1/2$	$I+1/2$	$I+3/2$	$I+3/2$	$I+3/2$	$I+3/2$	$I-3/2$
	$I-1/2$	$I+3/2$	$I+1/2$	$I+1/2$	$I-3/2$	$I-3/2$	$I+3/2$
	$I+3/2$	$I-1/2$	$I-1/2$	$I-3/2$	$I+1/2$	$I-1/2$	$I-1/2$
	$I-3/2$	$I-3/2$	$I-3/2$	$I-1/2$	$I-1/2$	$I+1/2$	$I+1/2$

Table II

Critical values of W' and ξ vs I.

$$W' = \frac{W}{ha}$$

W'_{nm} ξ	W'_{41}	$2I(2I-1)$	W'_{32}	$\frac{2I(2I-1)}{3}$	W'_{31}	$\frac{4I(2I-1)}{2I+5}$	W'_{21}	$\frac{2I(2I-1)}{2I+3}$	W'_{43}	$-2I$	W'_{42}	$\frac{-4I(2I-1)}{2I-3}$
I=3/2	15/4	6	-9/4	2	-15/8	3/2	-5/2	1	3/2	-3	-∞	-∞
2	6	12	-3	4	-13/6	8/3	-3	12/7	2	-4	-3	-24
5/2	35/4	20	-47/12	20/3	-49/20	4	-7/2	5/2	5/2	-5	-5/4	-20
3	12	30	-5	10	-30/11	60/11	-4	10/3	3	-6	-1/2	-20
7/2	63/4	42	-25/4	14	-3	7	-9/2	21/5	7/2	-7	0	-21
4	20	56	-23/3	56/3	-85/26	112/13	-5	56/11	4	-8	2/5	-112/5
9/2	99/4	72	-37/4	24	-99/28	72/7	-11/2	6	9/2	-9	3/4	-24
5	30	90	-11	30	-19/5	12	-6	90/13	5	-10	15/14	-180/7
11/2	143/4	110	-155/12	110/3	-65/16	55/4	-13/2	55/7	11/2	-11	11/8	-55/2
6	42	132	-15	44	-147/34	264/17	-7	44/5	6	-12	5/3	-88/3
13/2	195/4	156	-69/4	52	-55/12	52/3	-15/2	39/4	13/2	-13	39/20	-156/5
7	56	182	-59/3	182/3	-92/19	364/19	-8	182/17	7	-14	49/22	-364/11
15/2	255/4	210	-89/4	70	-51/10	21	-17/2	70/6	15/2	-15	5/2	-35
8	72	240	-25	80	-75/14	160/7	-9	240/19	8	-16	36/13	-480/13
17/2	323/4	272	-335/12	272/3	-247/44	272/11	-19/2	68/5	17/2	-17	85/28	-272/7
9	90	306	-31	102	-135/23	612/23	-10	102/7	9	-18	33/10	-204/5

$I = 1$, $J = 3/2$ is a special case and is treated separately in Table III and in Fig. A17 of Appendix II.

Table III

Critical values of W' and ξ for $I = 1$

$-2I = -2$	$\xi = 0$	$\frac{2I(2I-1)}{3} = \frac{2}{3}$	$\frac{-4I(2I-1)}{2I-3} = 4$
$W'_{43} = 1$	Normal order	$W'_{32} = -5/3$	$W'_{42} = 5/2$
$I+1/2$	$I+3/2$	$I+3/2$	$I-1/2$
$I+3/2$	$I+1/2$	$I-1/2$	$I+3/2$
$I-1/2$	$I-1/2$	$I+1/2$	$I+1/2$

J. Shell Model of the Nucleus

The experimentally determined nuclear spins are interpreted with the aid of the shell model of the nucleus.[4, 5] The concept of nuclear shells arises in much the same manner as the concept of electron shells in atomic spectra. Some evidence of nuclear shell structure is presented by:

(a) The fact that the binding energies of nuclei are relatively large at the so-called proton or neutron magic numbers 2, 8, 20, 28, 50, 82, 126 and 184.

(b) The existence of delayed neutron emitters. This phenomenon occurs for isotopes having one neutron in excess of a closed shell. The small binding energy of the odd neutron makes its emission possible if the nucleus is excited. Examples are ${}_{36}Kr_{51}$, ${}_{54}Xe_{83}$, and ${}_{8}O_{9}$.

(c) The fact that neutron absorption cross sections are small for nuclei having 50, 82, and 126 neutrons.

(d) Natural abundance.

The shell model predicts the magic numbers. It is based on the following observations and assumptions:

(a) The magic numbers are the same for protons as for neutrons.

The nucleons retain a degree of individuality, and therfore individual nucleon orbits may be considered.

(b) The nucleons are assumed to be noninteracting. Each one moves in an average field of force that is spherically symmetric.

(c) The sequence of energy levels predicted might be slightly different for protons and neutrons, since orbits of lower orbital angular momentum penetrate deeper into the nuclear core. The proton interaction with the repulsive Coulomb field is stronger in these orbits. Therefore, nuclei with high numbers of protons tend to have neutrons in the lower-angular-momentum orbits.

A potential function intermediate to the harmonic oscillator and the rectangular well predicts the magic numbers. The predominant feature of this model is the strong interaction of the nucleon spin and orbital angular momentum. Figure 8 presents the sequence of energy levels predicted for protons successively filling shells. Figure 9 presents the same information for neutrons. The numbers in parentheses represent the total number of nucleons in all levels filled to that point in the figure. The numbers immediately to the left represent the degeneracies of the particular levels.

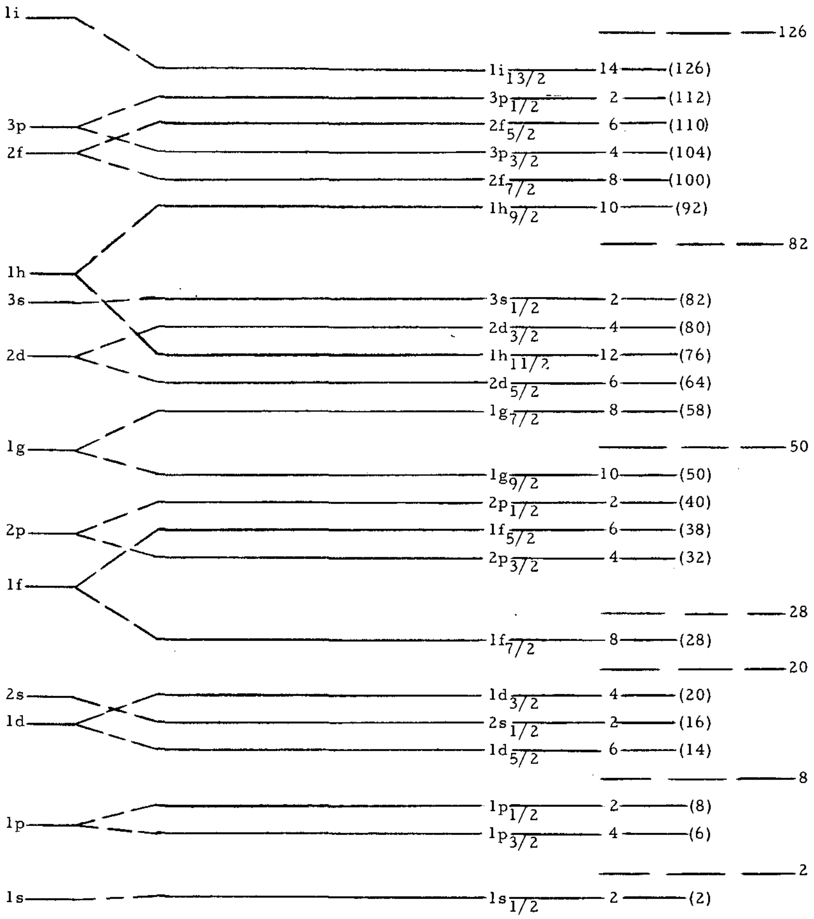

MU-17154

Fig. 8. Shell-model energy-level sequence for protons. Numbers in parentheses are total numbers of nucleons. The degeneracies are shown to the left.

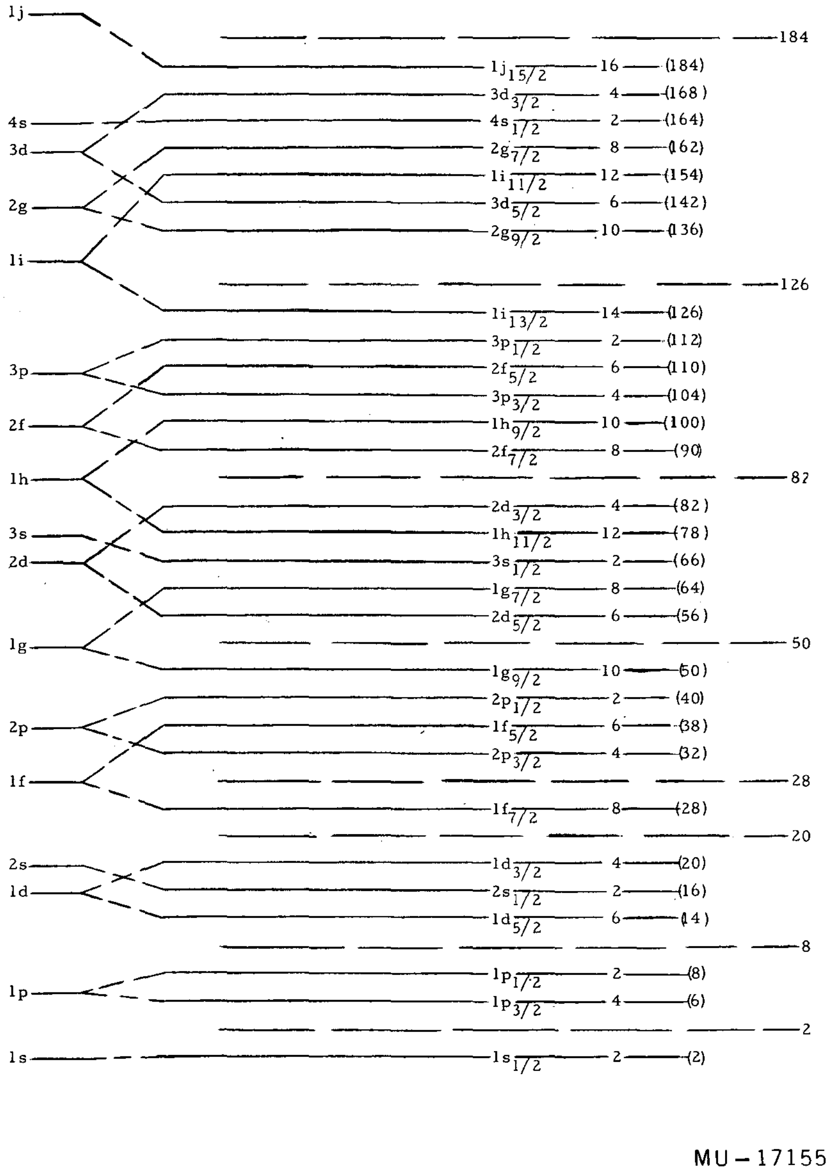

Fig. 9. Shell-model energy-level sequence for neutrons. Numbers in parentheses are total numbers of nucleons. The degeneracies are shown to the left.

II. MEASUREMENT TECHNIQUE

Figure 10 is a schematic sketch of the apparatus. Three magnetic fields are involved. The A and B magnets supply inhomogeneous fields. The field gradient and field are both in the same direction. The C magnet provides a homogeneous field, also in the same direction as the A and B fields. An atom enters the A-field region from the oven O. A force acts upon it as a consequence of the A-field inhomogeneity,

$$\vec{F} = \nabla W = - \frac{\partial W}{\partial H} \frac{\partial H}{\partial z} = \mu_{eff} \frac{\partial H}{\partial z} , \tag{87}$$

where μ_{eff} is the effective magnetic moment of the atom.

From Eq. (9) it may be seen that this moment is of the order of a Bohr magneton. It is apparent that the effective moments are equal to the negative slopes of the lines on the energy-level diagram. Assume that the sign of the effective moment is changed by causing the atom to make a transition between the appropriate quantum states. The transition is caused by applying the proper radio-frequency to a hairpin in the C field (Appendix III). Then the atom is deflected in a path bringing it toward the apparatus axis and reaches the detector D. If the effective moment does not change sign, then the atom is deflected further from the apparatus axis in the B field and strikes the pole tips. Thus, a signal appears at the detector if and only if a transition has occurred. The stop wire S serves to prevent the nonmagnetic molecules and high-velocity atoms from reaching the detector. The detector for radioactive species consists of sulfur-coated brass "buttons" to which the atoms adhere. The buttons are then analyzed with a system consisting of a sodium iodide (thallium-activated) crystal, photomultiplier, and pulse-height analyzer. The counting equipment, radio-frequency equipment, and electron bombardment loader are discussed in the thesis of H. A. Shugart.[6] The apparatus design and construction are discussed in the thesis of R. J. Sunderland.[7] See Fig. 11 for a photograph of the apparatus.

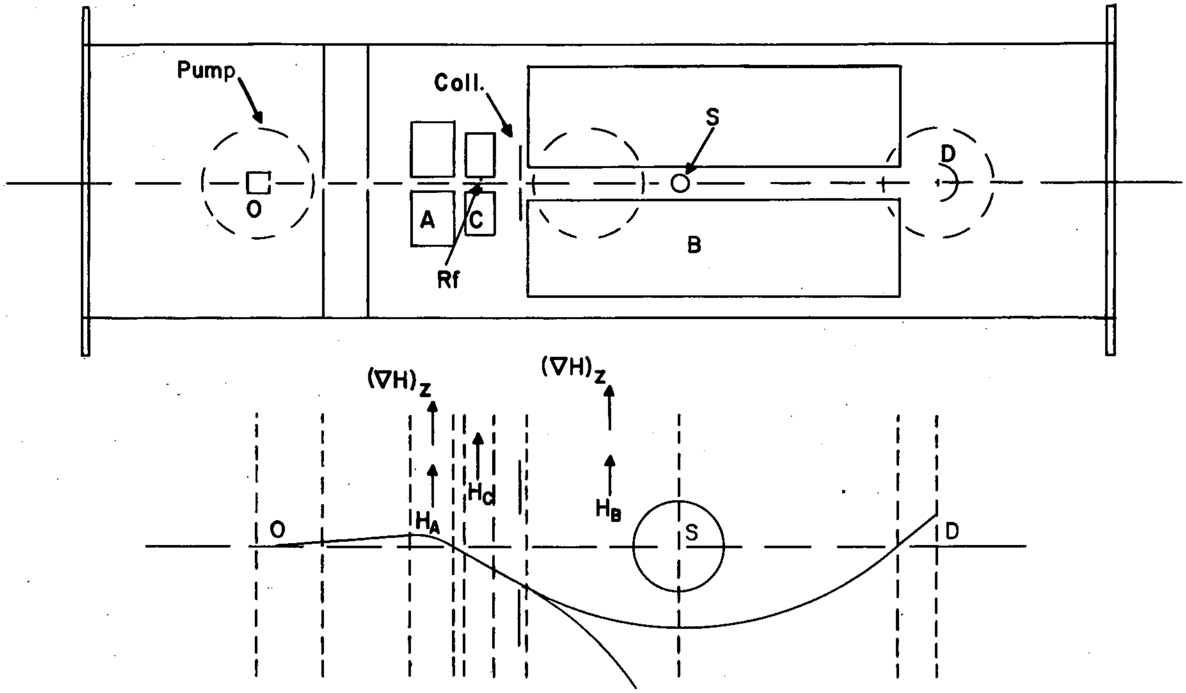

MU-12688

Fig. 10. Schematic sketch of atomic-beam apparatus.

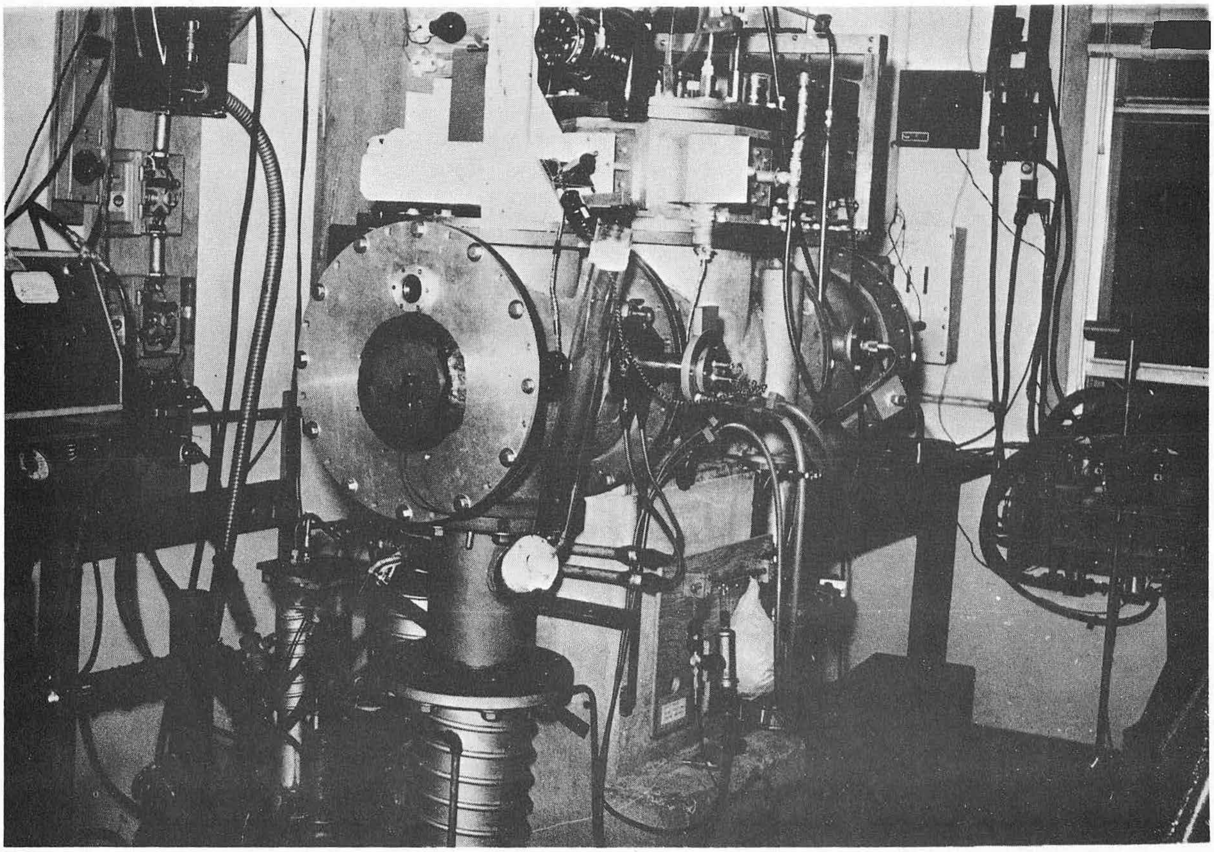

ZN-2135

Fig. 11. Atomic beam apparatus.

Pi transitions were utilized. This type is characterized by the selection rule $\Delta F = 0$, $\Delta m = \pm 1$. The beam passes through the hairpin and at right angles to it. The oscillating magnetic field is perpendicular to the C field. For $J = 1/2$, the quantum numbers associated with the transition are $F = I + 1/2$, $m = -I + 1/2 \leftrightarrow -I - 1/2$. For $J = 3/2$, in the normal order, two transitions are possible, characterized by

$$\begin{aligned} F &= I + 3/2 \qquad & m &= -I + 1/2 \leftrightarrow -I - 1/2, \\ F &= I + 1/2 \qquad & m &= -I + 3/2 \leftrightarrow -I + 1/2. \end{aligned} \tag{88}$$

These transition frequencies were computed in Eqs. (20) and (35).

III. EXPERIMENTAL PROCEDURE

The nuclear spin is determined from the weak-field approximation

$$\nu = -g_F \frac{\mu_0}{h} H(m_1 - m_2), \tag{89}$$

where g_F is defined in Eq. (6). For a particular transition, $m_1 \leftrightarrow m_2$, there exists a unique frequency for a given spin I. Thus, buttons are exposed at frequencies corresponding to the probable spin values and the counting rate of each button is measured. All buttons save one will have the same counting rate, called the apparatus background, due to gas scattering in the apparatus. The button corresponding to the spin, however, will possess a higher counting rate due to the appearance of a signal as described in the preceding section.

As an equivalent to a direct measurement of the magnetic field in Eq. (89), the transition frequency of a calibration isotope, such as cesium or rubidium, is set at the desired value. These two materials are chosen because they are easily detectable with a hot-wire ionization detector. Their ground-state J value is equal to 1/2, so that the frequency is given by Eq. (22).

Thus, we have

$$\nu_x = \frac{g_F}{g_J} (2I + 1)\, \nu_{cal}, \tag{90}$$

where the g_F refers to isotope x and the I and g_J are constants of the calibration isotope. Table IV presents the transition frequencies for bismuth isotopes when the transition frequency of Rb^{85} or Rb^{87} is set at 1 Mc/sec; here ν^+ refers to the transition $F = I + 3/2$, $m = -I + 1/2 \leftrightarrow -I - 1/2$, ν^- refers to the transition $F = I + 1/2$, $m = -I + 3/2 \leftrightarrow -I + 1/2$.

Caution must be exercised in interpreting experimental results since, for high spins, the frequencies lie close together and certain transitions may not be resolved because of the resonance line width. Experiments are conducted at higher fields until the second-order terms in the field become important. At this point, the results of the perturbation calculation are useful (Eqs. (34) and (35)). The quantities

Table IV

Transition frequency versus I for bismuth.

$\nu^+ \rightarrow F = I+3/2, m = -I+1/2 \leftrightarrow -I-1/2$; $\nu^- \rightarrow F = I+1/2, m = -I+3/2 \leftrightarrow -I+1/2$

		$\nu_{Bi}(Rb^{85} = 1$ Mc/sec)		$\nu_{Bi}(Rb^{87} = 1$ Mc/sec)	
I	F	ν^+	ν^-	ν^+	ν^-
0	3/2	4.9299		3.2866	
1/2	2	3.6975		2.4650	
1	5/2	2.9580		1.9720	
1	3/2		3.6153		2.4102
3/2	3	2.4651		1.6434	
3/2	2		2.4651		1.6434
2	7/2	2.1129		1.4086	
2	5/2		1.8312		1.2208
5/2	4	1.8486		1.2324	
5/2	3		1.4379		0.9586
3	9/2	1.6434		1.0956	
3	7/2		1.1739		0.7826
7/2	5	1.4790		0.9860	
7/2	4		0.9861		0.6574
4	11/2	1.3446		0.8964	
4	9/2		0.8466		0.5644
9/2	6	1.2324		0.8216	
9/2	5		0.7395		0.4930
5	13/2	1.1376		0.7584	
5	11/2		0.6549		0.4366
11/2	7	1.0563		0.7042	
11/2	6		0.5868		0.3912
6	15/2	0.9861		0.6574	
6	13/2		0.5309		0.3540
13/2	8	0.9243		0.6162	
13/2	7		0.4842		0.3228
7	17/2	0.8700		0.5800	
7	15/2		0.4446		0.2964
15/2	9	0.8217		0.5478	
15/2	8		0.4107		0.2738
8	19/2	0.7785		0.5190	
8	17/2		0.3816		0.2544
17/2	10	0.7395		0.4930	
17/2	9		0.3561		0.2374
9	21/2	0.7044		0.4696	
9	19/2		0.3336		0.2224

ν^{+}_{∞} and ν^{-}_{∞} may be calculated, $\delta\nu^{+}$ and $\delta\nu^{-}$ are the shifts of the resonances from the ν_{∞} values and may be measured experimentally. Thus, $\Delta\nu_{43}$ and $\Delta\nu_{32}$ may be computed. Values of a and b may then be calculated from Eq. (34). When approximate values of a and b are known, the more useful IBM programs may be used. Another way of arriving at starting values of a and b exists. If the appropriate quantities are known for at least two isotopes of the element of interest, it is possible to predict approximate values of a and b for the isotope of interest.

A Fermi-Segre type of relation connects a and g_I in the following manner:[8]

$$a = \frac{c\, R_y\, \alpha^2 z^3 g_I}{n^3 (M/m)(L+1/2) J(J+1)} ,$$

where

$$R_y = \frac{me^4}{4\pi\hbar^3 c} \quad \text{and} \quad \alpha = \frac{e^2}{\hbar c} .$$

Thus, for two isotopes of the same element,

$$\frac{a_1}{a_2} = \frac{g_{I_1}}{g_{I_2}} ,$$

or, for $I_1 = I_2$,

$$\frac{a_1}{a_2} = \frac{\mu_{I_1}}{\mu_{I_2}} \tag{92}$$

A similar relation between the quadrupole moment Q and the quadrupole interaction constant b is

$$\frac{b_1}{b_2} = \frac{Q_1}{Q_2} . \tag{93}$$

IV. PREPARATION AND SEPARATION; RESULTS

A. Bismuth

Isotope Production

The nuclear spin of (6.4-day)Bi^{206} was investigated. Figure 12 presents a decay scheme.[9, 10, 11] In the references from which this is taken, an underlined spin means that it has been measured directly. A spin designated by its quantum number without any other modification means that its value has been determined uniquely by other means. Parentheses indicate probable spin values. Double arrows indicate that a level has been Coulomb-excited from the ground state.

The isotope was produced in the Crocker 60-inch cyclotron by bombardment of 0.015-inch lead foils, measuring 1-3/4 by 1-1/2 in., with 24-Mev deuterons. The reaction is

$$(26\%)Pb^{206}(d, 2n)Bi^{206}.$$

That this is the dominant reaction may be seen by reference to Fig. 13. The lead target was placed in the direct beam of the cyclotron and cooled with water. A 20-μa beam was allowed to strike the target for 3 hours. Since the activity was distributed most densely over the center of the foil, this portion was removed for the chemistry procedure.

Chemistry

The radioactive bismuth was separated from the lead by the method of internal electrolysis[12] (Fig. 14). The target, together with 5 mg of bismuth, was dissolved with 60 ml of 20% nitric acid. The solution was heated gently and neutralized with about 20 ml of concentrated ammonium hydroxide. Three ml of concentrated nitric acid was added and the volume increased to between 200 and 250 ml of liquid. The lead anodes were surrounded with dialyzing tubing. These two compartments were filled with a 5% solution of lead nitrate acidified with nitric acid. The solution containing the dissolved target was stirred and heated to about 85° C and a platinum electrode inserted. The electrode and the two anodes were connected together.

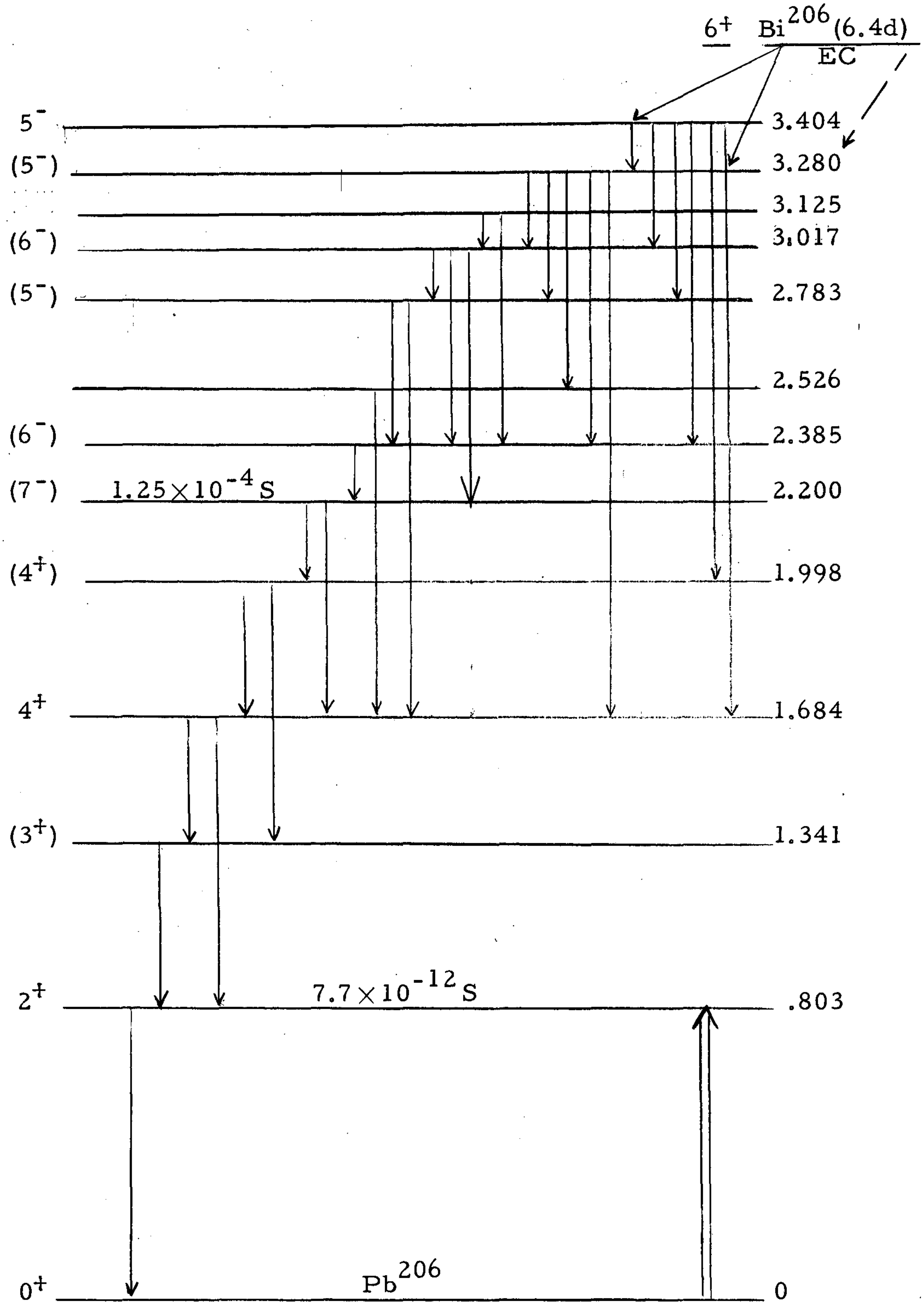

Fig. 12. Decay scheme of Bi^{206}.

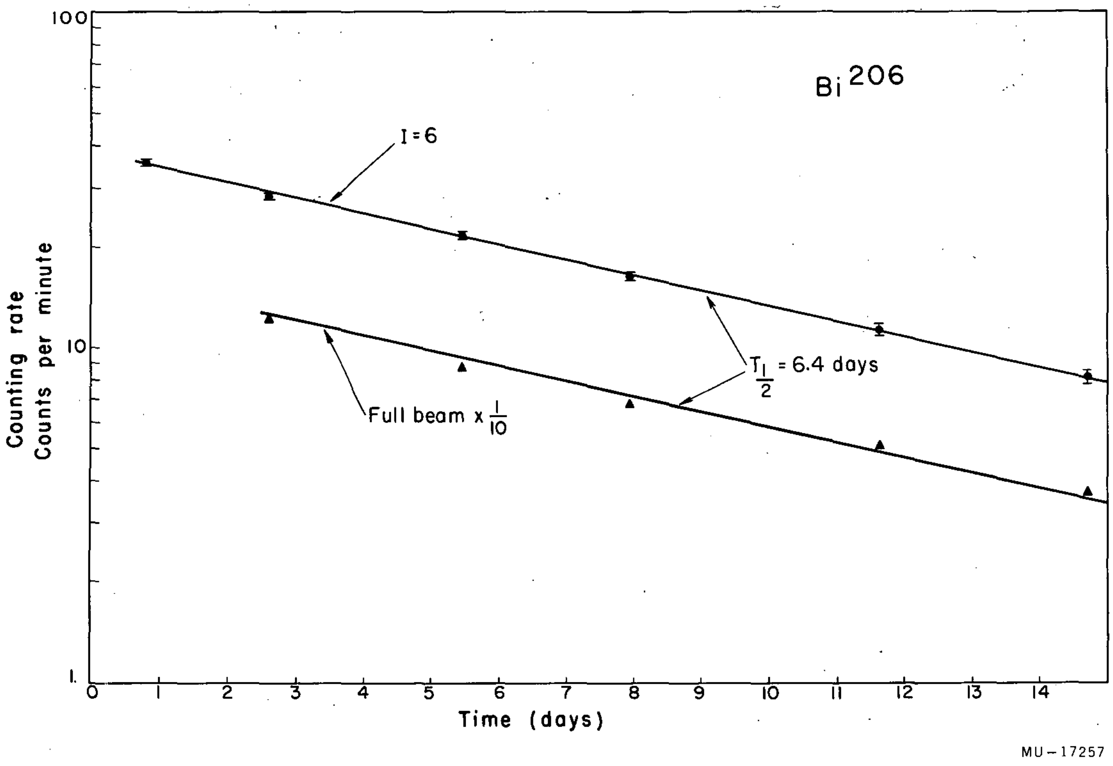

Fig. 13. Decay plot of Bi^{206}.

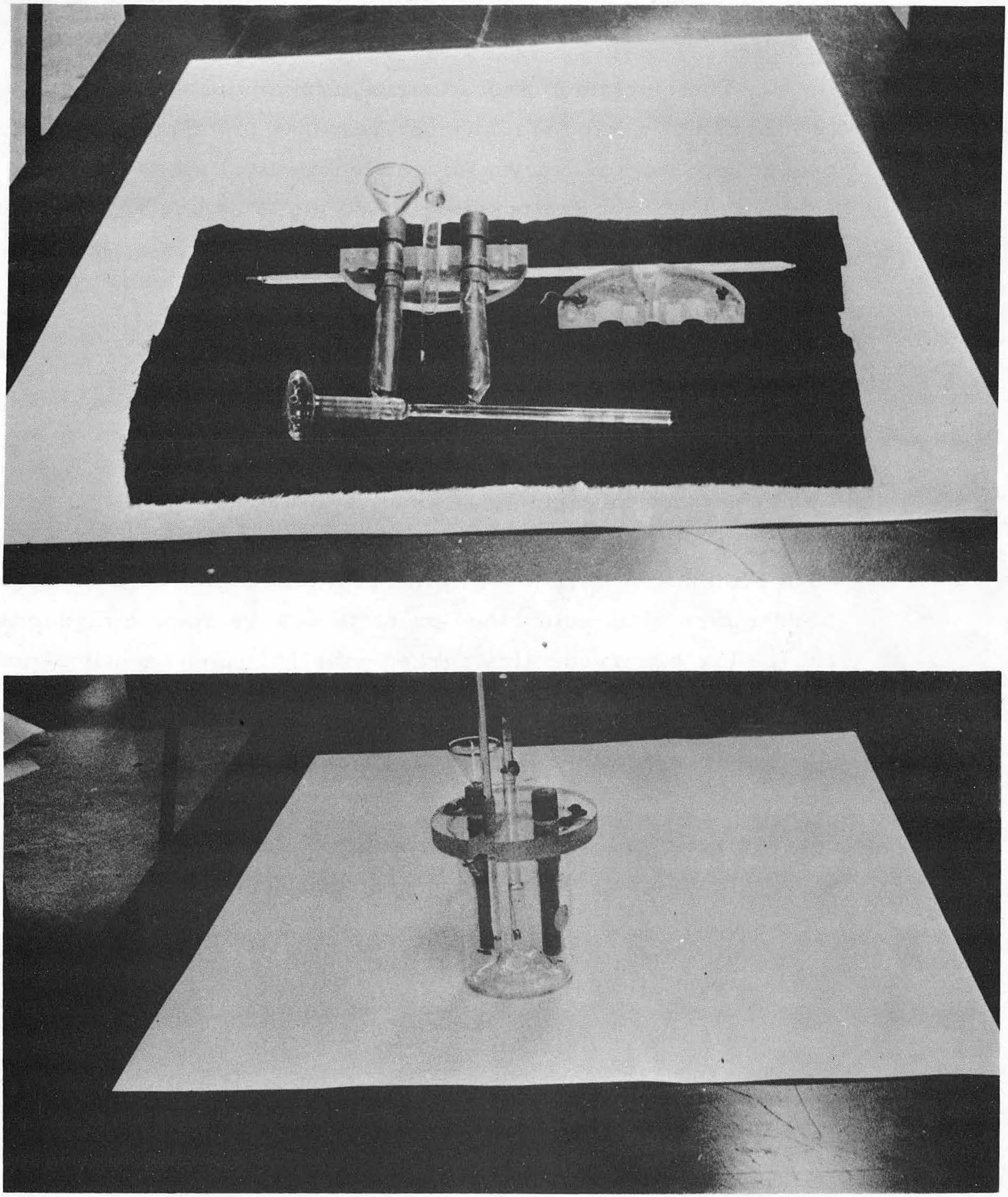

ZN-2137

Fig. 14. The internal-electrolysis apparatus used to separate bismuth from lead.

The bismuth plated out on the platinum and was introduced into the oven by snipping the wire, allowing it to fall into the oven below.

Results

The electronic ground state of bismuth is $^4S_{3/2}$, therefore, two focusing π type transitions are possible. The ground-state properties are well known for stable Bi^{209}. Its g_J value is $1.6433 \pm .0002$.[13] The results of a spin search are shown in Fig. 15. The transition

$$F = 15/2,\ m = -11/2 \leftrightarrow -13/2$$

is represented by ν^+ and

$$F = 13/2,\ m = -9/2 \leftrightarrow -11/2 \text{ by } \nu^-.$$

The presence of a signal at I = 6 is evident. This spin value was confirmed by taking a resonance sweep at a higher magnetic field (Fig. 16). The spin can be made plausible[14] by coupling the 83rd proton in a $h_{9/2}$ level to the 123rd neutron in the $f_{5/2}$ level. Nordheim's weak rule[4] then predicts a large spin no higher than I = 7. The observed value agrees with that subsequently reported by Lindgren and Johansson.[15, 16]

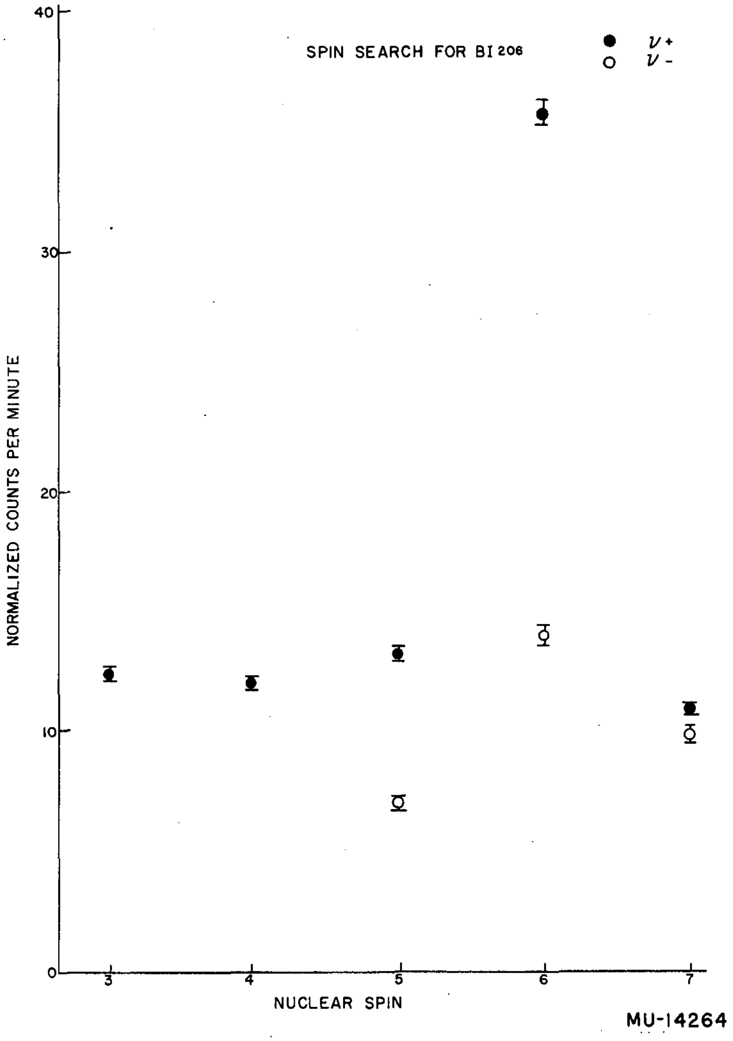

Fig. 15. Bi^{206} spin search.

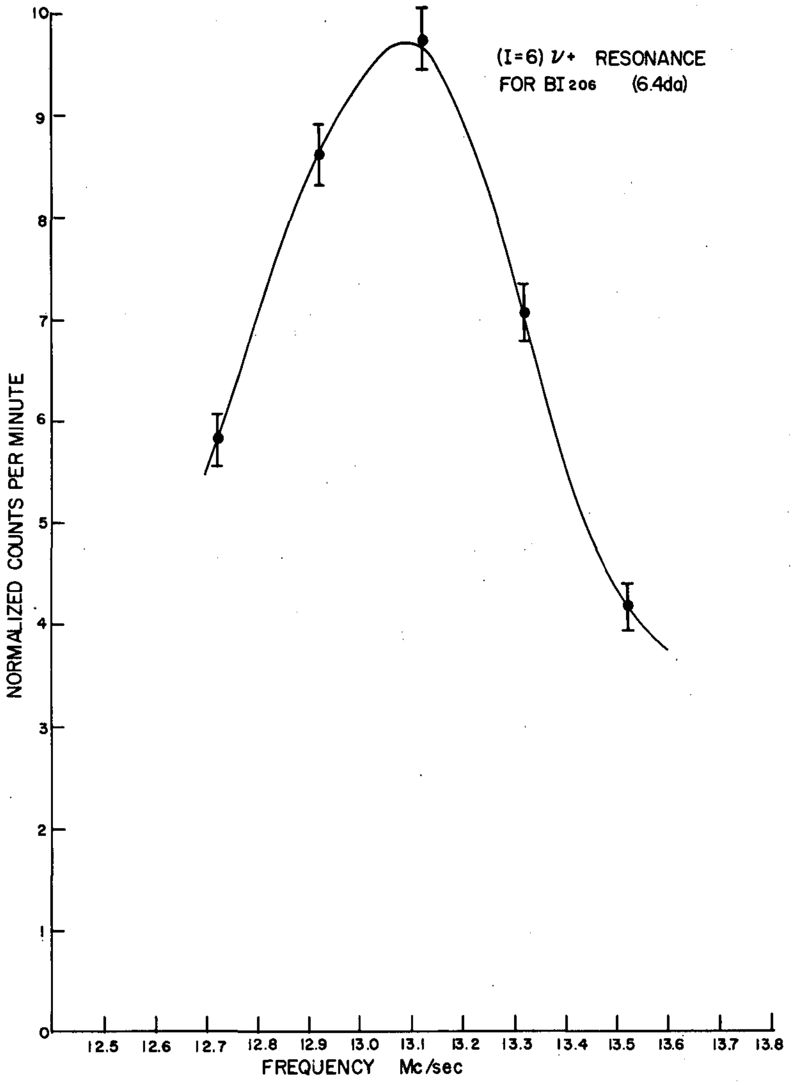

MU-17168

Fig. 16. Bi^{206} resonance.

B. Thallium

Isotope Production

The nuclear spins were measured for (26.1-hr) Tl^{200},[17] (3.0-day) Tl^{201},[18] and (12.5-da) Tl^{202}.[19] Figures 17, 18, and 19 present the decay schemes of these isotopes.[10, 20-23] The isotopes were produced in the 60-inch cyclotron by bombarding mercury with 24-Mev deuterons. A beam current of 35 μa for 3 hours was employed. The mercury was mounted in target form by placing droplets in small holes drilled in a standard aluminum external-target mount. The droplets were sealed in with successive teflon and aluminum gaskets.

The following reactions occur:

(23%) $Hg^{200}(d, 2n) Tl^{200}$(26.1 hr),

(17%) $Hg^{199}(d, 1n) Tl^{200}$(26.1 hr),

(13%) $Hg^{201}(d, 2n) Tl^{201}$(3 da),

(23%) $Hg^{200}(d, 1n) Tl^{201}$(3 da),

(13%) $Hg^{201}(d, 1n) Tl^{202}$(12.5 da),

(30%) $Hg^{202}(d, 2n) Tl^{202}$(12.5 da),

(17%) $Hg^{199}(d, 2n) Tl^{199}$(7.4 hr),

(10%) $Hg^{198}(d, 1n) Tl^{199}$(7.4 hr),

(10%) $Hg^{198}(d, 2n) Tl^{198m}$(1.9 hr),

(10%) $Hg^{198}(d, 2n) Tl^{198}$(5 hr),

(.15%) $Hg^{196}(d, 1n) Tl^{197m}$(0.54 sec),

(.15%) $Hg^{196}(d, 1n) Tl^{197}$(2.8 hr),

(.15%) $Hg^{196}(d, 2n) Tl^{196}$(4 hr),

(6.8%) $Hg^{204}(d, 2n) Tl^{204}$(4.1 yr).

Evidence was also found for

(29.8%) $Hg^{202}(d,p) Hg^{203}$(48 da).

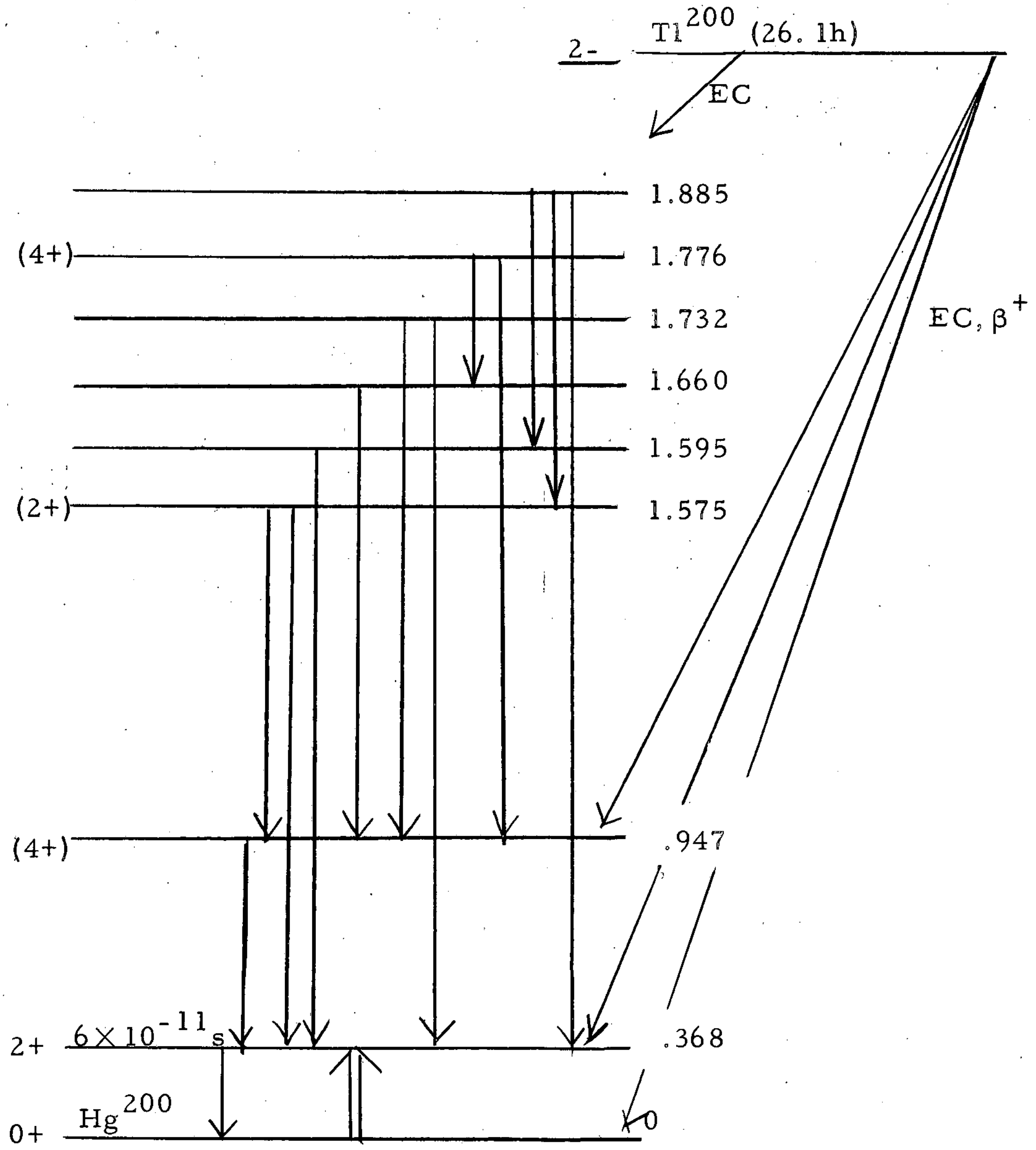

Fig. 17. Decay scheme of Tl^{200}.

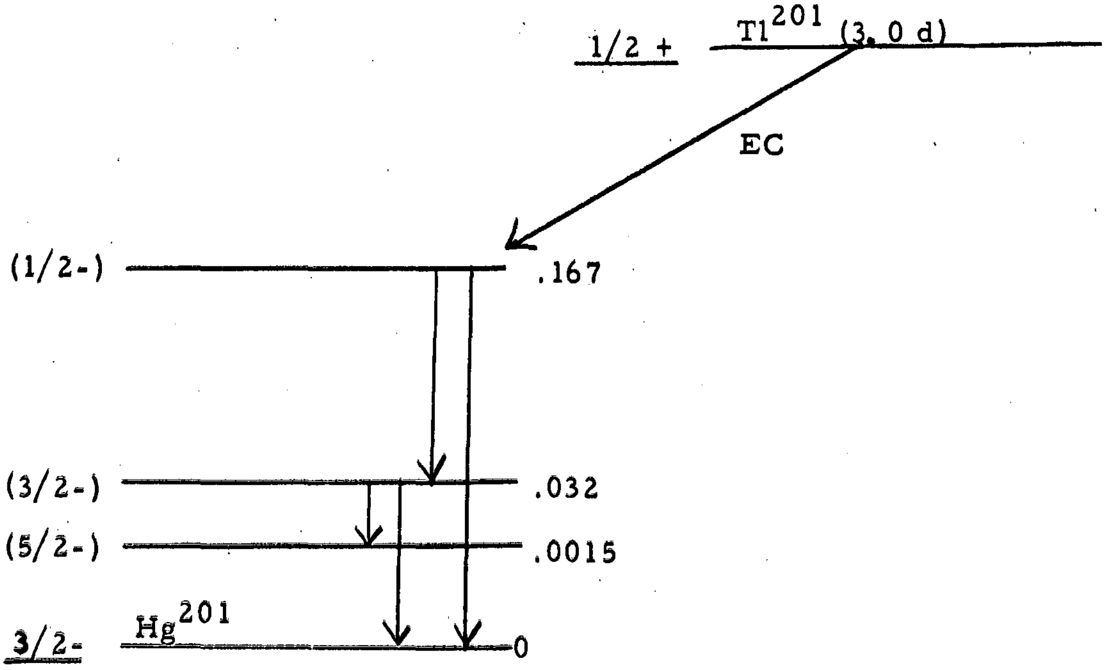

Fig. 18. Decay scheme of Tl^{201}.

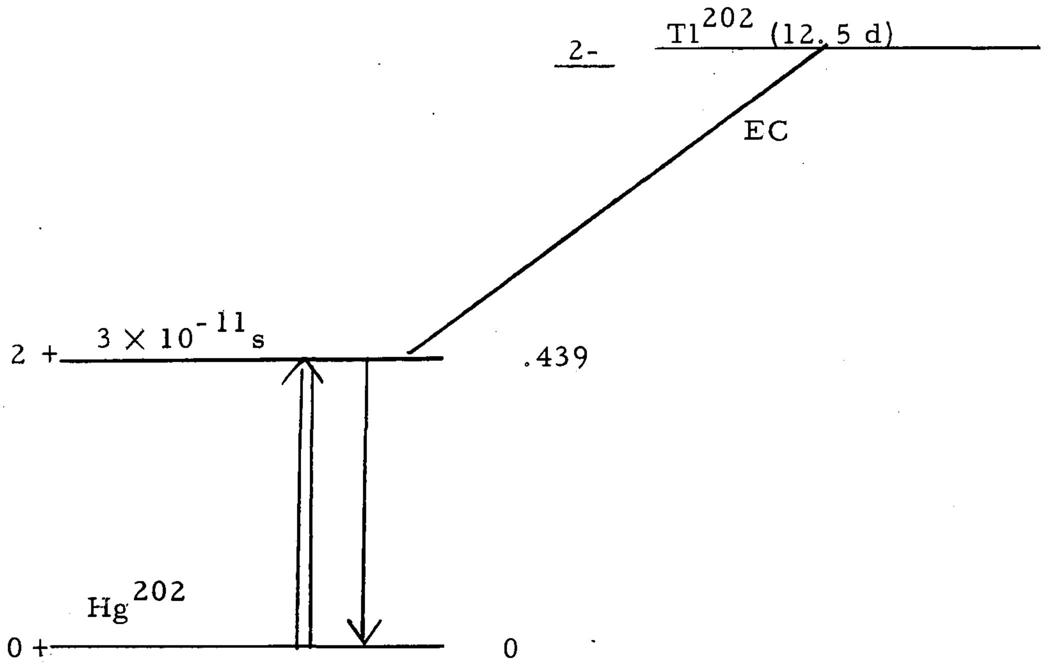

Fig. 19. Decay scheme of Tl^{202}.

The composite decay of a chemistry sample is shown in Fig. 20. Each target was allowed to "cool" for about 24 hours prior to an experiment in order to allow the shorter-lived isotopes to decay appreciably.

Chemistry

The boiling points of mercury and thallium are 357°C and 1457°C, respectively, at atmospheric pressure, thus suggesting an evaporative method of separation. This was accomplished in an atmosphere of helium or argon with the glass apparatus sketched in Fig. 21. The target block was unloaded through narrow-tipped glass tubing into a test tube connected to a water aspirator. About 30 mg of thallium carrier was added and part of the mixture was introduced into the cup A. Stopcock B was opened and Stopcock C closed. Approximately one oven load of material was drawn down by means of a hypodermic syringe attached to point D via rubber tubing. Stopcock B was closed and Stopcock C opened. The oven load was then forced into the tantalum oven mounted at E by pressure applied with the syringe. The induction coils F were energized and the temperature of the oven raised until all the mercury was evaporated from the oven, leaving the radioactive thallium behind. The process was repeated until all the mercury was evaporated. The separation was performed in the cave shown in Fig. 22.

Results

The electronic ground state of thallium is $^2P_{1/2}$ and therefore only one type of focusing transition exists. The $^2P_{3/2}$ state lies 7792 cm^{-1} above the $^2P_{1/2}$ state and is not appreciably excited at the oven temperature (800°C) required to produce a beam of thallium. For Tl^{200} and Tl^{202}, the transitions were found to be $F = 5/2$, $m_F = -3/2 \leftrightarrow -5/2$; for Tl^{201}, $F = 1$, $m_F = 0 \leftrightarrow -1$.

The results of one spin search are shown in Fig. 23. Spin buttons for $I = 1/2$ and $I = 2$ appear to have definite signals. The decays of the spins and full-beam buttons (A and B fields off, stop wire off the apparatus axis) are shown in Fig. 24. It is evident that the $I = 1/2$ sample contains a pure 3-day activity, Tl^{201}. The $I=2$ sample starts to decay faster than both the full beam and $I= 1/2$ samples, indicating the presence of Tl^{200}.

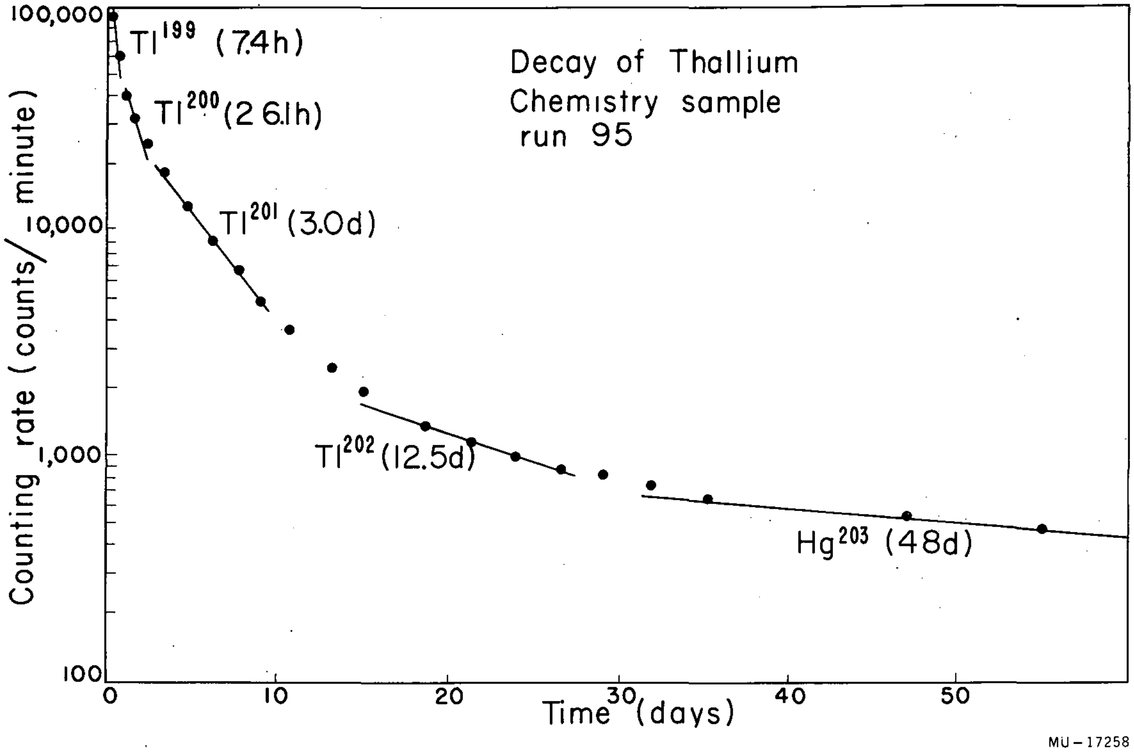

Fig. 20. Radioactive decay of a thallium chemistry sample.

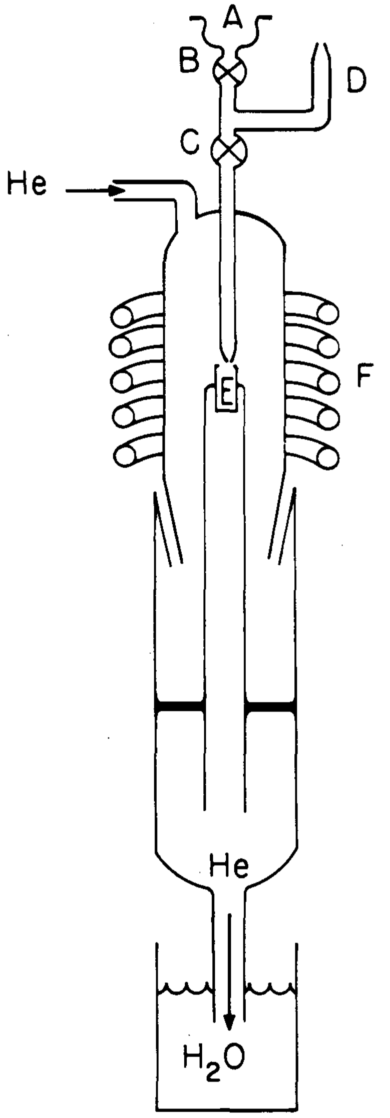

MU-17223

Fig. 21. Sketch of thallium-separation apparatus.

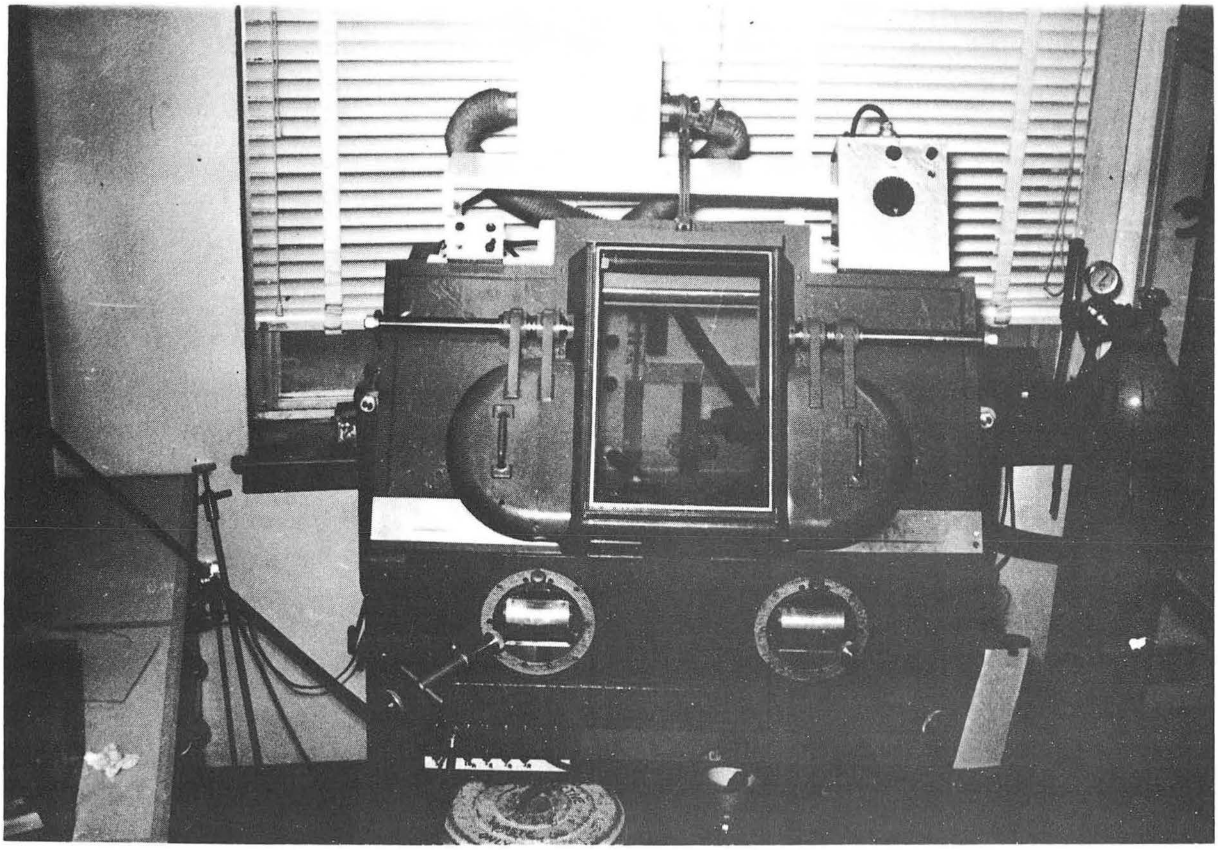

ZN-2136

Fig. 22. Cave used for the separation of thallium from mercury.

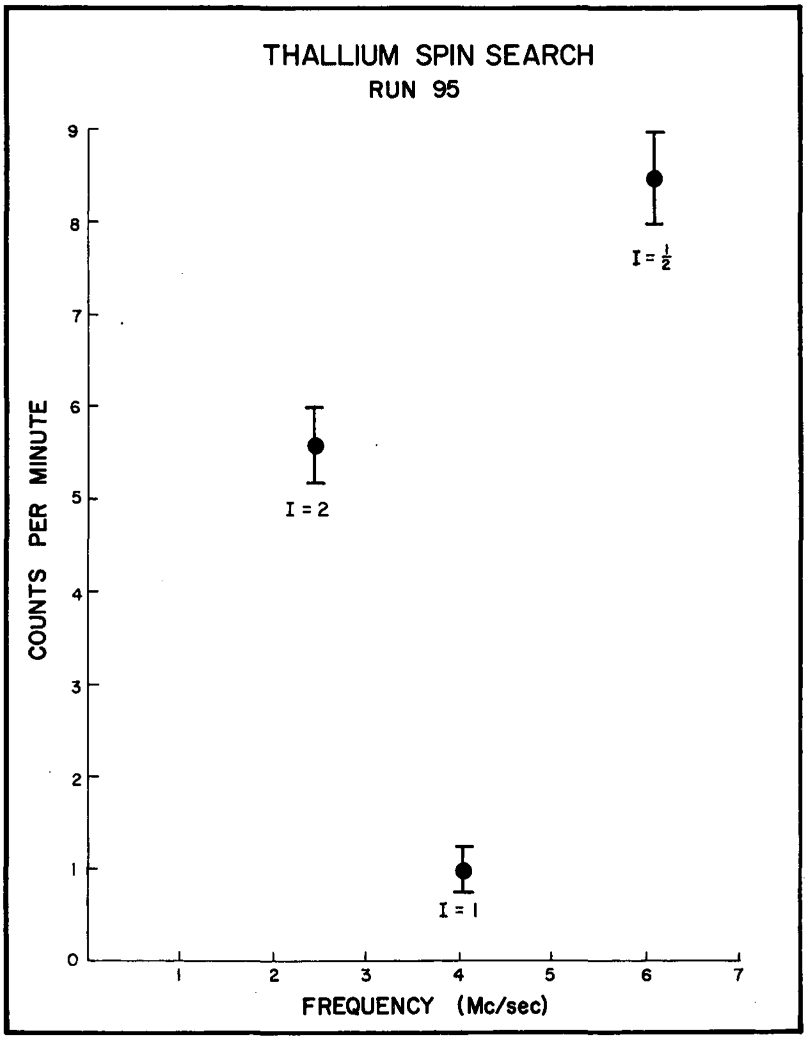

MU-15034

Fig. 23. Thallium spin search.

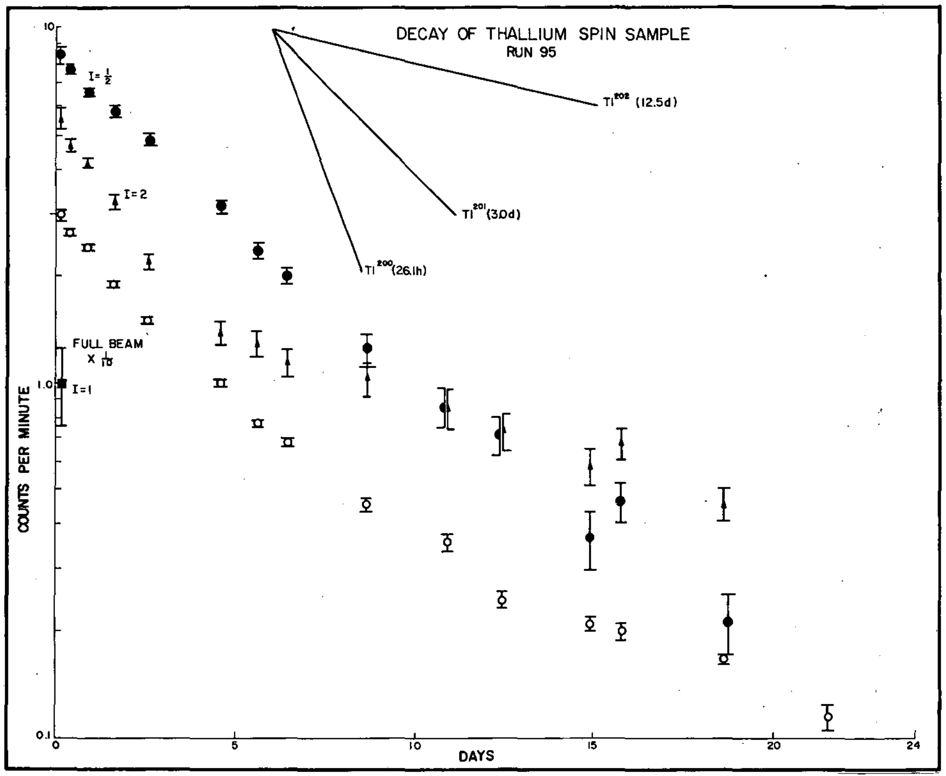

MU-17169

Fig. 24. Decay of thallium spin sample.

It then decreases and its curve crosses the curve for the I = 1/2 sample, suggesting the presence of Tl^{202}. This latter point was verified by increasing the cyclotron bombardment time and letting the target decay for 5 days before conducting the experiment. Figure 25 presents the results of this run. The enhancement of 12-day activity on the I = 2 sample compared with the half-beam sample (A and B field on, stop wire off the apparatus axis) is apparent. All spins were checked for at least two values of magnetic field. Table V presents the results of two runs, after a half-life analysis was performed on each spin button to determine the amount of each isotope present at a common time. This was done via a program constructed by H. B. Silsbee. The thesis of H. A. Shugart contains further details.[6]

Table V

Results of thallium spin searches (counts per minute)

Isotope and half life		Half beam	Spin			
			1/2	1	2	3
Run 95			(at 6.1 Mc)	(at 4.0 Mc)	(at 2.4 Mc)	
Tl^{200}	27 h	6.6(.6)	0.0(.4)	0.0(.2)	3.2(.3)	
Tl^{201}	3 d	18.5(.5)	7.9(.4)	0.0(.2)	0.7(.3)	
Tl^{202}	12 d	3.5(.1)	0.4(.1)	0.7(.1)	1.4(.1)	
Run 129				(at 8.2 Mc)	(at 4.9 Mc)	(at 3.5 Mc)
Tl^{201}	3 d	123.3(.5)		0.7(.1)	1.1(.1)	0.8(.1)
Tl^{202}	12 d	19.6(.2)		0.2(.1)	1.8(.1)	0.1(.1)
Hot-wire normalizations				1.2	1.0	1.0

From this table and the decay curves, it may be concluded that I = 2 for Tl^{200} and Tl^{202}, I = 1/2 for Tl^{201}.[24, 25] The measurement I = 1/2 for Tl^{201} is consistent with a $3s_{1/2}$ assignment for the 81st proton in Tl^{197} or Tl^{199},[26] in Tl^{203}, or in Tl^{205}. I = 2 for Tl^{200} and Tl^{202} may be predicted by coupling the 119th neutron in a $3p_{3/2}$ level to the 81st proton in the $3s_{1/2}$ level. This spin value is identical to that of Tl^{204} and Tl^{198}.[26, 27]

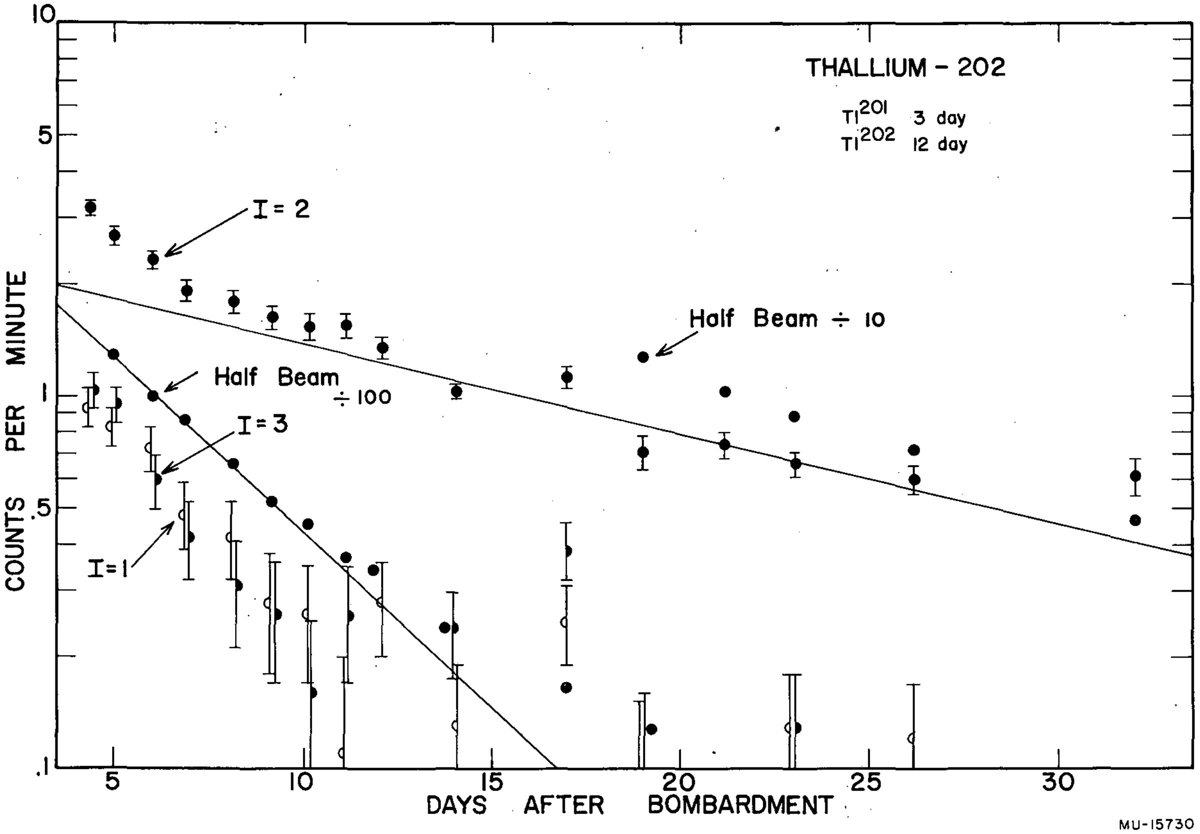

Fig. 25. Decay of Tl^{202} spin sample.

C. Indium

Isotope Production

The spins and the magnetic dipole and electric quadrupole moments were determined for (4.3-hr) In^{109},[28] (5.0-hr) In^{110m},[29] and (2.8-d) In^{111}.[30] Figures 26, 27, and 28 present the decay schemes of these isotopes.[10, 31-34] The isotopes were produced by bombarding 0.005- to 0.010-in. silver foil with 48-Mev α particles in the Crocker cyclotron. The target type is the same as that described in the bismuth investigation.

The reactions that occur are:

(49%) $Ag^{109}(\alpha, 2n)In^{111}$(2.8 d),

(49%) $Ag^{109}(\alpha, 3n)In^{110m}$(5 hr) and In^{110}(66 min),

(51%) $Ag^{107}(\alpha, 1n)In^{110m}$(5 hr) and In^{110}(66 min),

(49%) $Ag^{109}(\alpha, 4n)In^{109}$(4.3 hr),

(51%) $Ag^{107}(\alpha, 2n)In^{109}$(4.3 hr),

(51%) $Ag^{107}(\alpha, 3n)In^{108m}$(55 min) and In^{108}(40 min),

(51%) $Ag^{107}(\alpha, 4n)In^{107}$(30 min),

(49%) $Ag^{109}(\alpha, 1n)In^{112}$(21 min, 25 sec, 15 min).

A 90-μa beam was allowed to strike the target for 3 hours when an experiment with In^{109} or In^{110m} was being planned. For the experiments on In^{111} alone, the target was exposed for 10 hours. Before the separation procedure was initiated, the targets were allowed to decay so that the short-half-life components would not be present in large quantities. This lag time was about 1-1/2 hours for runs with In^{109} and In^{110m}, whereas for In^{111} experiments the target was not processed for about 1-1/2 days after bombardment.

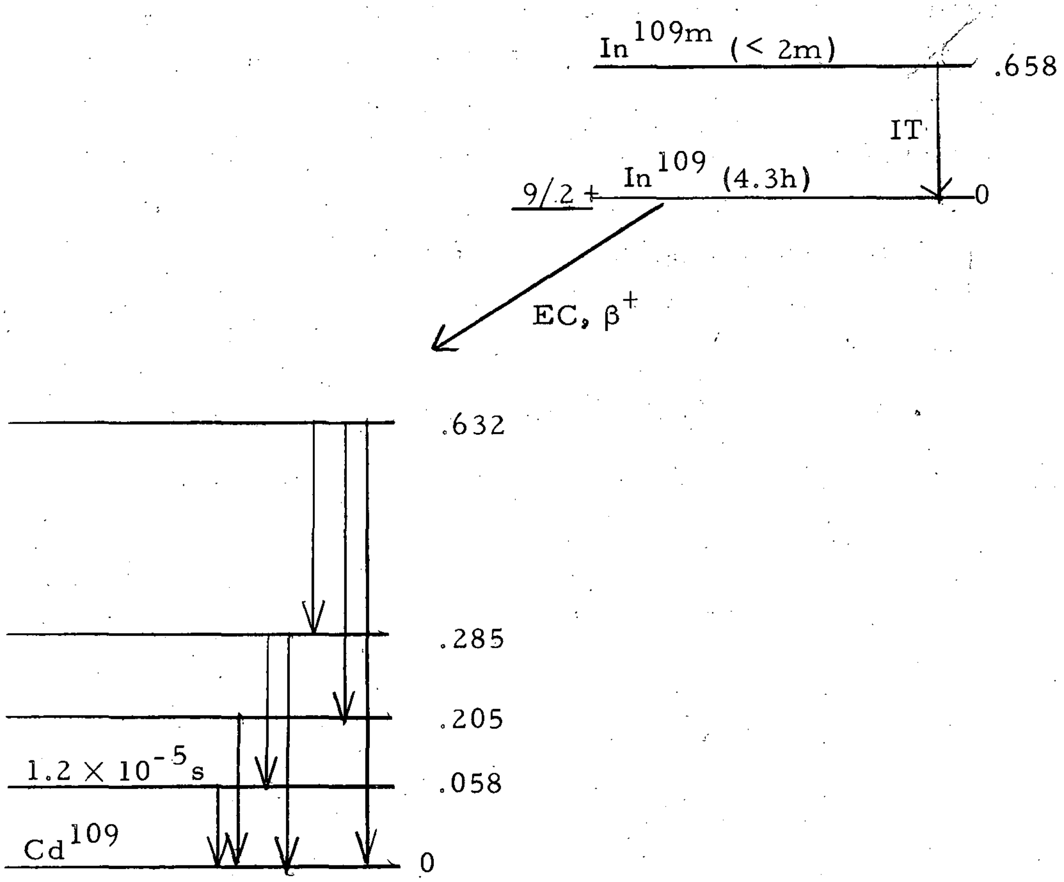

Fig. 26. Decay scheme of In^{109}.

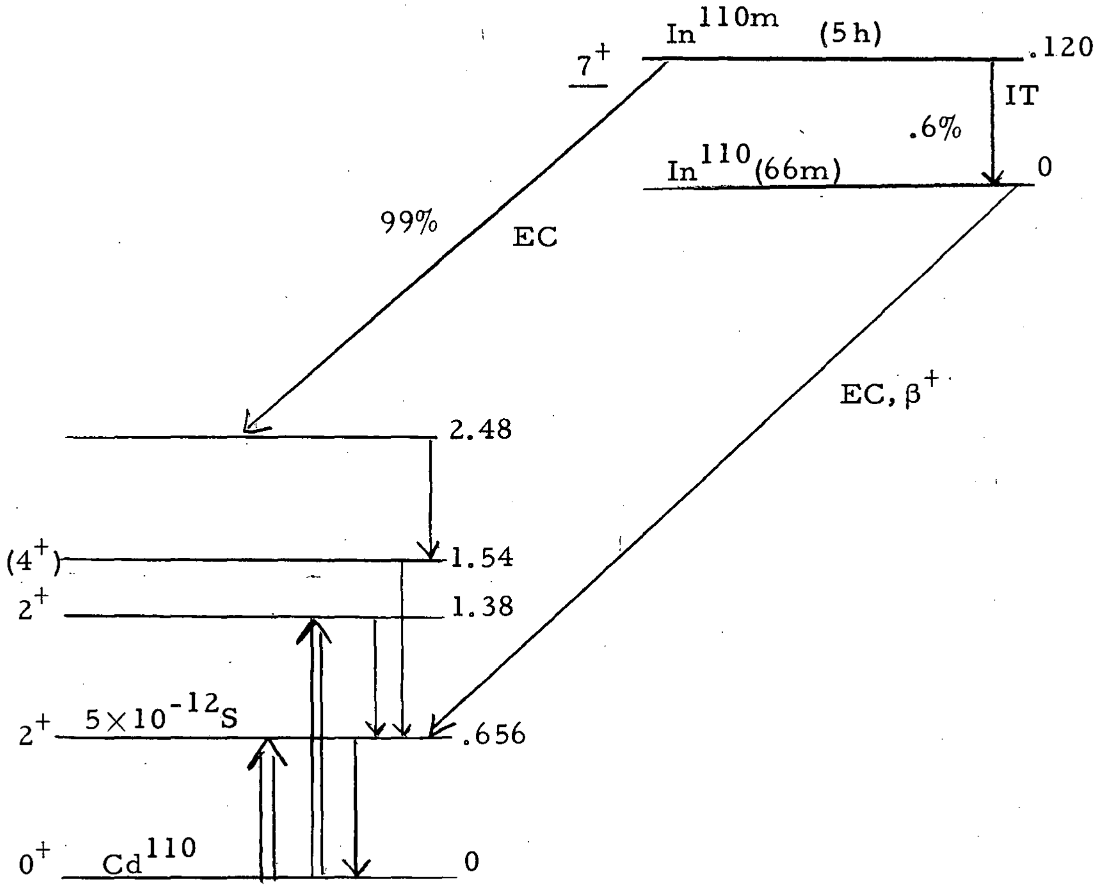

Fig. 27. Decay scheme of In^{110m}.

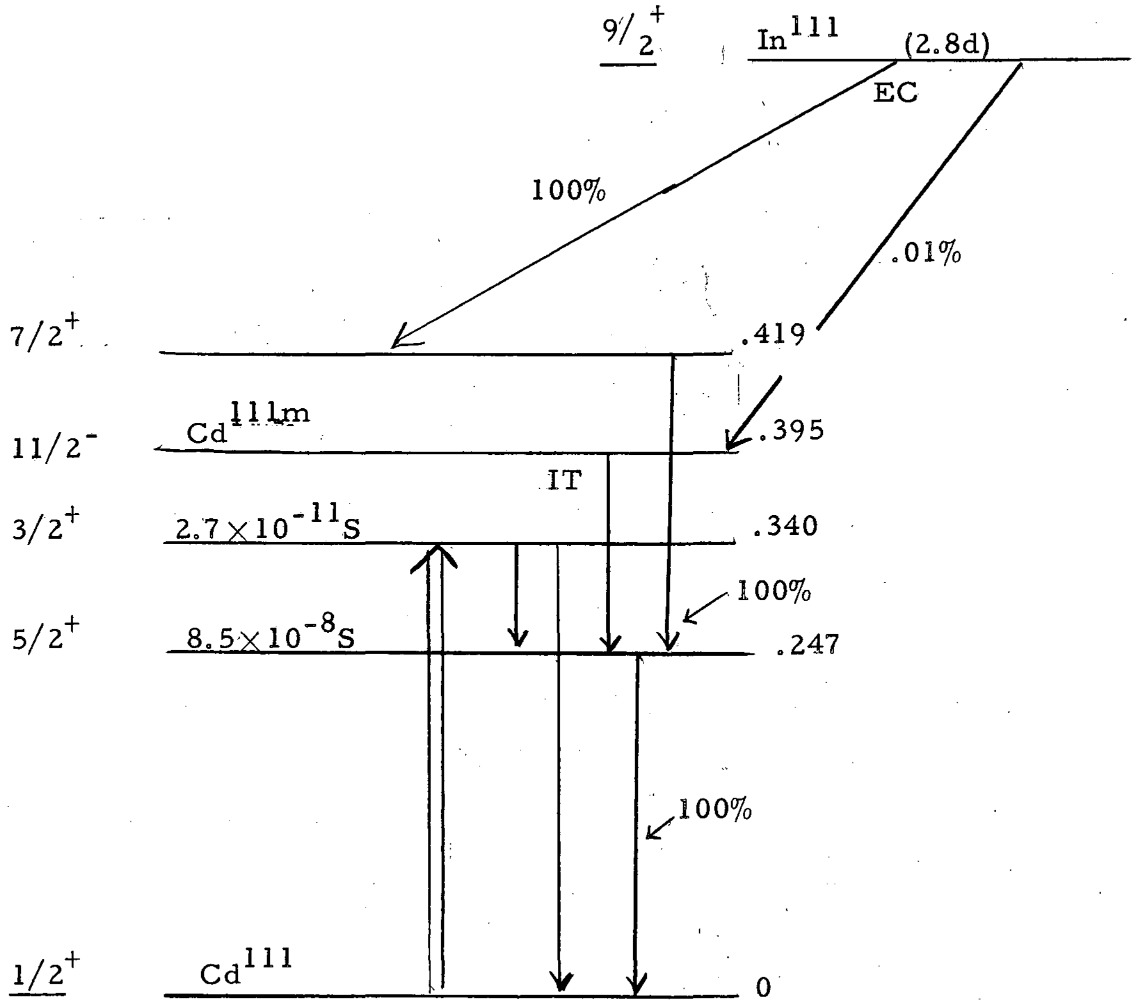

Fig. 28. Decay scheme of In^{111}.

Chemistry

Chemical separation was accomplished by dissolving the center portion punched from the silver foil and about 25 mg of indium carrier in concentrated nitric acid. The silver was precipitated as the chloride upon the addition of concentrated hydrochloric acid. After the precipitate was separated by centrifuging, about 15 mg of oxalic acid or potassium sodium tartrate was added to the supernatant for plating purposes. From a slightly acid solution, the indium was electroplated onto a platinum electrode with a 0.2-amp plating current (8 amp/in.^{2}). At first, the electrode was placed directly in either a carbon or a tantalum oven, which was then heated in the apparatus by electron bombardment. Later experimentation showed that a steadier beam resulted if the deposit was scraped from the electrode and placed in a carbon oven. A typical separation time was 1-1/2 hours. Recovery was about 50%.

This procedure was later modified to produce a better deposit and to improve the yield. The modification consisted of using a minimum amount of concentrated nitric acid to dissolve the target. This was evaporated to dryness and 10 ml of distilled water added. After separation by centrifuging, the indium was precipitated as the hydroxide by the drop-by-drop addition of concentrated ammonium hydroxide. After centrifugation and pouring off of the supernatent, concentrated hydrochloric acid was added drop-by drop until the precipitate dissolved. At this point, there was about 3 ml of solution. Two drops of formic acid were added and the indium was electroplated onto a platinum wire at 0.080 amp (3 amp/in^2). The separation time was about 3 hours and the recovery about 80%.

Results

The transitions observed for In^{109} and In^{111} were $F = 6$, $m_F = -4 \leftrightarrow -5$, and $F = 5$, $m_F = -3 \leftrightarrow -4$. For In^{110m}, the focusing transitions are $F = 17/2$, $m_F = -13/2 \leftrightarrow -15/2$, and $F = 15/2$, $m_F = -11/2 \leftrightarrow -13/2$. The electronic ground state is $^2P_{1/2}$ but larger resonances were observed in the $^2P_{3/2}$ state. The fine structure is 2212 cm^{-1}. At the oven temperature required for a stable beam, about 20% of the atoms were in the upper state. It is surmised that better results were obtained from this smaller portion of the beam because the g_F for the $^2P_{3/2}$ state is about 4/3, whereas for the $^2P_{1/2}$ state g_F is about 2/3. The ground-state properties of In^{115} are well known. The g_J is 1.3343 ± .0001.[35, 36, 37]

1. Indium-111 Spin Results

The results of spin searches are indicated in Table VI. Because Runs 88 and 93 were made several days after the bombardments, the shorter-lived isotopes had decayed, leaving relatively pure In^{111}. With only a single activity present in the beam, resonance indications must be determined on the basis of absolute counting rates. For Runs 88 and 93 the spin-9/2 signals are greater by an order of magnitude than those for other half-integral values. Decay curves for these resonances showed a single 2.8-day component which indicated that In^{111} was responsible for the signal. The In^{111} resonance has been observed from 4.8 to 7.8 Mc/sec to establish the linear Zeeman dependence of the resonance frequencies on the low-transition magnetic field.

2. Indium-110m Spin Results

When the target was processed immediately after bombardment, it contained in addition to In^{111} several other isotopes, including 4.3-hr In^{109} and 5.0-hr In^{110m}. Because of low counting rates, it is not possible to distinguish between 4.3 and 5.0 hours by decay alone. However, In^{109} must have half-integral spin while In^{110m} must have integral spin. This information along with an approximate half-life determination suffices to establish the identity of these short-lived isotopes.

Because in this work three isotopes contribute to the initial counting rates, each sample may be analyzed for the relative composition of short (4.3- and 5.0-hr) activity and long (2.8-day) activity. When this is done as shown in Table VII for Run 104, the ratio of short to long components of the counting rate on the "half-beam" sample (magnets on but stop wire removed) at zero time is 3.1.

Table VI

Table of initial counting rates of indium spin searches[a]

Run	Spin 1	2	5/2	7/2	4	9/2	5	11/2	6	7	8
88(In^{111}only)			0.5(1)	0.8(1)		5.2(2)					
93(In^{111}only)				0.6(1)		6.6(2)		0.4(1)			
96	0.9(3)[b]	0.5(1)		0.8(1)	0.4(1)	2.3(2)	0.7(2)		0.4(1)	1.6(2)	
104						8.2(3)	1.9(2)			4.5(2)	3.5(2)[c]

[a] These rates (in arbitrary units) are corrected for counter background and normalized for variations in beam intensity within a single run. All runs were performed at different values of magnetic field. (The numbers in parentheses are the errors in the last digit.)

[b] Poor normalization.

[c] The $^2P_{3/2}$, F = 5, $m_F = -3 \leftrightarrow -4$ transition for I = 9/2 occurs at the same frequency as the $^2P_{3/2}$, F = 19/2, $m_F = -15/2 \leftrightarrow -17/2$ transition for I = 8 within the line width.

Table VII

Composition analysis of samples from run 104.

Counting rates are not corrected for variations in beam intensity.

Sample	Short activity counts/min	Long activity counts/min	Ratio short/long
"Half-beam"	276 (3)	90 (2)	3.1 (2)
9/2	9.9 (7)	5.6 (4)	1.8 (2)
5	2.6 (4)	1.1 (2)	2.4 (6)
7	7.1 (1)	1.5 (2)	4.7 (8)

The spin-5 sample, though very small in absolute counting rate, shows a similar ratio (2.4) for an apparatus background sample, as would be expected. On the other hand, it is clear from Table VII that the spin-7 sample contains an enhanced short component (In^{110m}). In fact, the short component on the spin-7 sample is 2.7 times the apparatus background (spin-5 sample), while the long components are essentially equal (see Fig. 29). Further confirmation of spin 7 for In^{110m} comes from information on Run 96. In Run 96 (Table VI) the normalized counting rate for spin 7 is 3.7 times the average rate for the other integral spins. (In Run 104 the signal at "spin 8" is the $^2P_{3/2}$, $F = 5$, $m_F = -3 \leftrightarrow -4$ transition for the 9/2 material. This signal supports the 9/2 assignment of In^{109} and In^{111}.)

3. Indium-109 Spin Results

The spin 9/2 button of Run 104 (Table VII) shows significantly more short activity (9.9 counts/min) than a typical background sample, e. g., spin 5 with only 2.6 counts/min of short activity (also see Fig. 29). The exposures were roughly equal, therefore the enhancement by a factor 3.8 is attributed to a spin-9/2 signal from In^{109}. Likewise the composition of the $I = 9/2$ sample differs from that of the half-beam sample in such a way as to indicate the relative enrichment of In^{109} and In^{111} over In^{110m}.

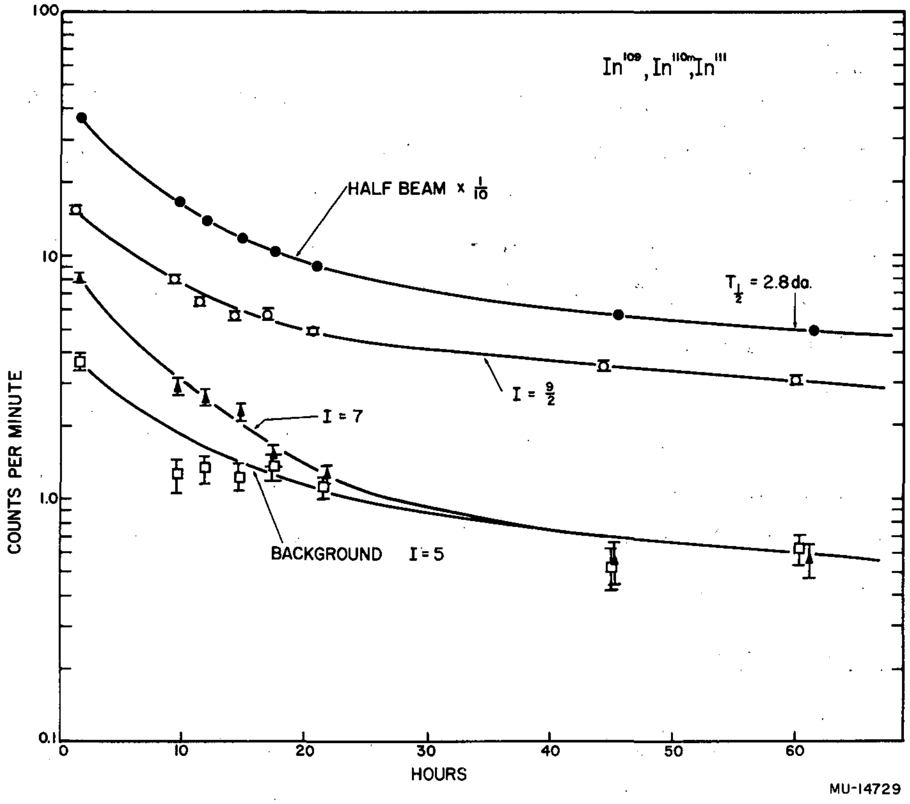

Fig. 29. Decay plot of spin samples from Run 104.

The signal also has about the expected magnitude, for if In^{109} and In^{110m} were produced more or less equally, the half-beam determination shows that each would contribute about 1.5 times as much initial activity as In^{111}. The observed ratio of In^{109} to In^{111} on the spin-9/2 sample is 1.8 before any apparatus background corrections.

4. Remarks

Spin 9/2 for In^{111} and In^{109} agrees with the simple shell-model prediction that the forty-ninth proton is in a $g_{9/2}$ state.[4, 38] Spin 7 for In^{110m} could arise from coupling of a $g_{9/2}$ proton and a $d_{5/2}$ neutron, which is predicted by the shell model in this region.[4, 38] The series from In^{110m}(I = 7) to In^{114m}(I = 5) and In^{116m}(I = 5)[39, 40] may then illustrate the transition from a $d_{5/2}$ to an $s_{1/2}$ level for the odd neutron.

The spins of all three isotopes were further confirmed by taking resonance sweeps at higher values of magnetic field. As indicated under "Numerical Methods," values of a and b may be obtained from these resonances.

5. Interaction Constants

a. In^{110m}

From the resonance curves in Figs. 30 to 35, the values of the interaction constants are obtained for In^{110m}. The sign of the nuclear magnetic moment was not determined.

For a positive magnetic moment we have

$$a = 291.4(1.2) \text{ Mc/sec},$$

$$b = -112(16) \text{ Mc/sec}.$$

From this, we may compute

$$\xi = -0.384(55),$$

$$\mu = +10.4(1) \text{ nm},$$

$$Q = -0.290 \times 10^{-24} \text{ cm}^2,$$

see Fig. 36 for an energy-level diagram for $\mu_I > 0$.

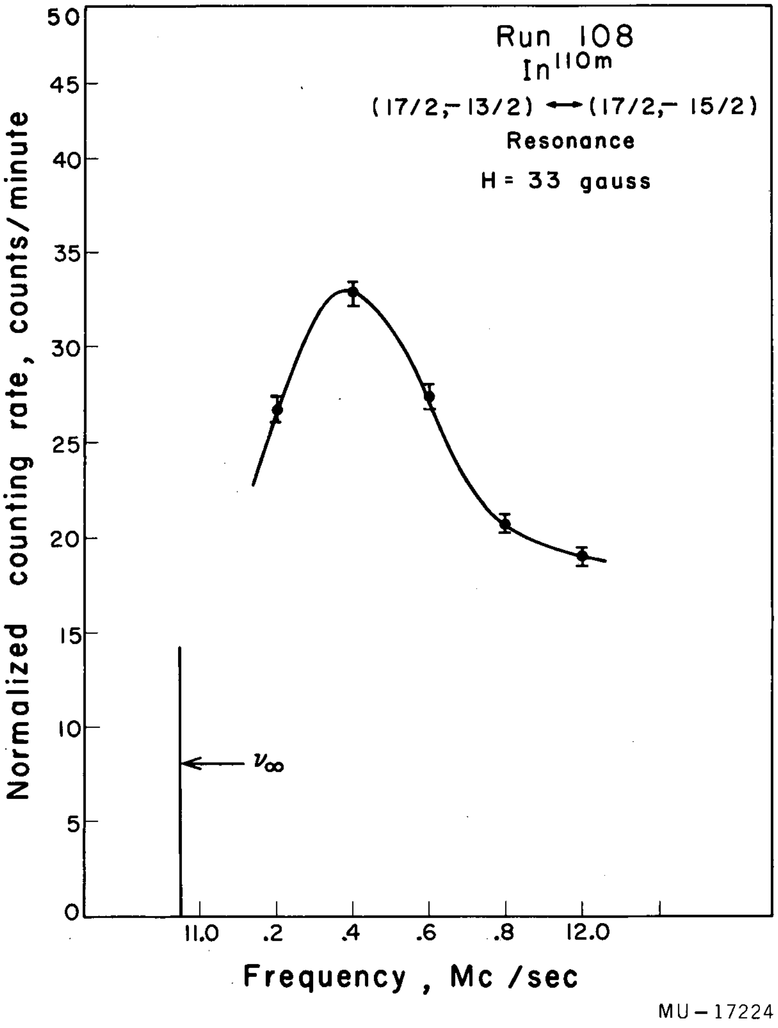

Fig. 30. In^{110m} (17/2, -13/2) ↔ (17/2, -15/2) resonance.

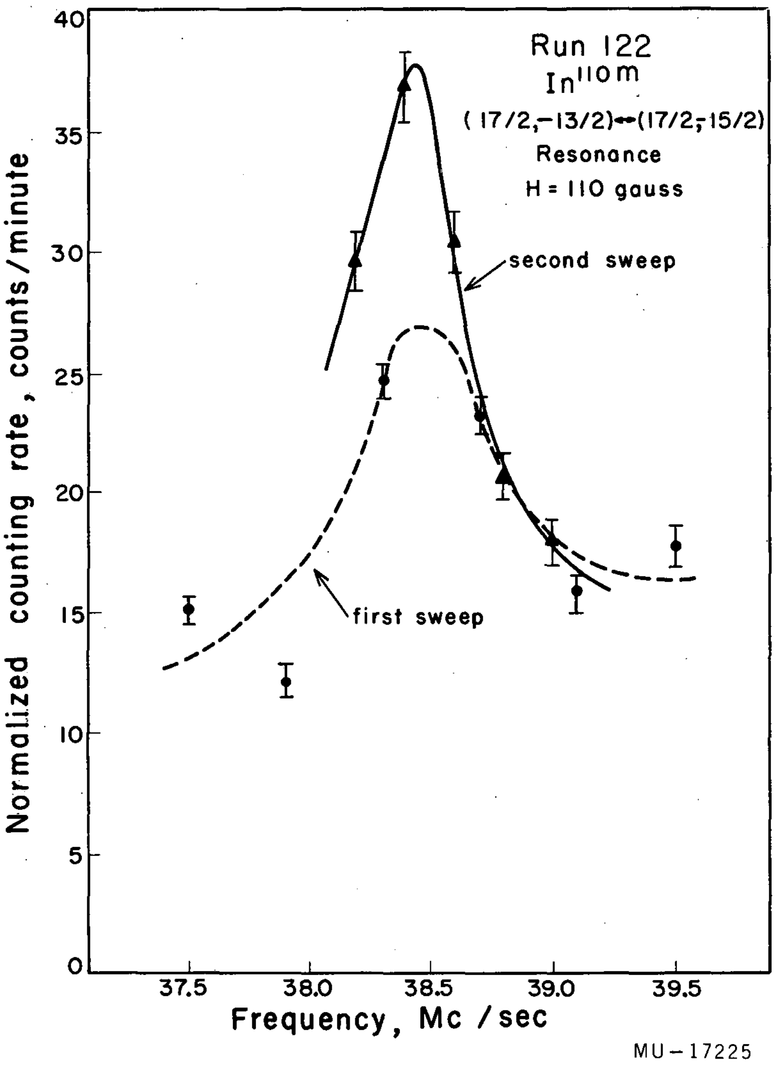

Fig. 31. In^{110m} (17/2, -13/2) ↔ (17/2, -15/2) resonance.

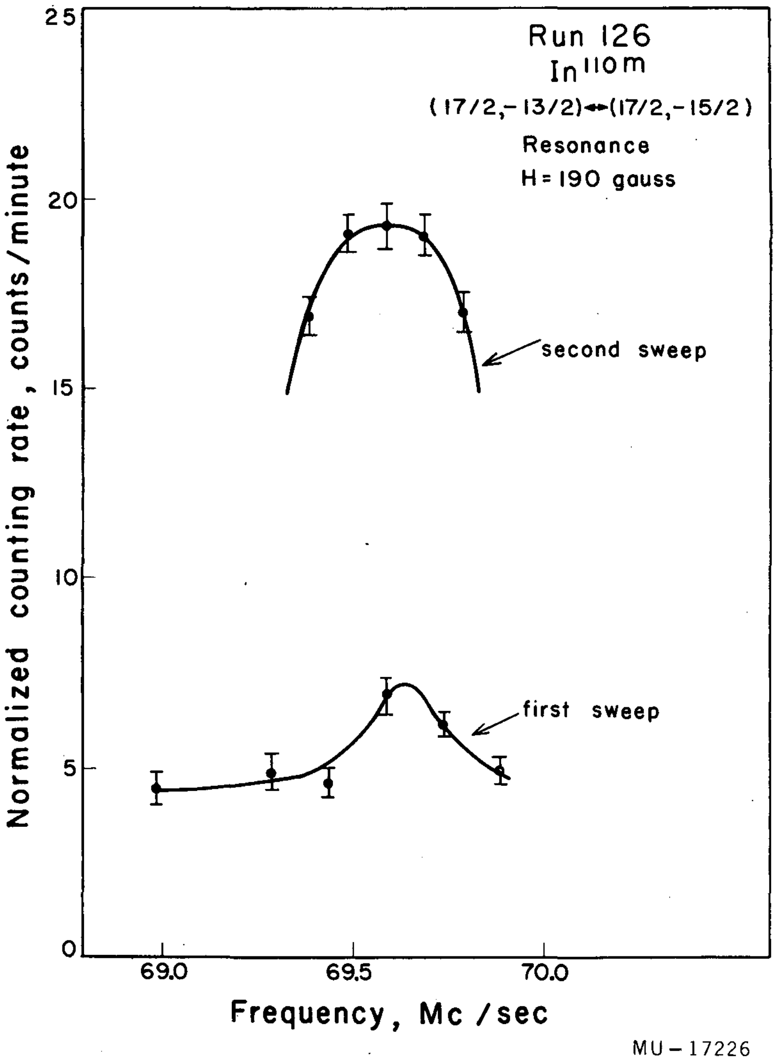

Fig. 32. In^{110m}(17/2, -13/2) ↔ (17/2, -15/2) resonance.

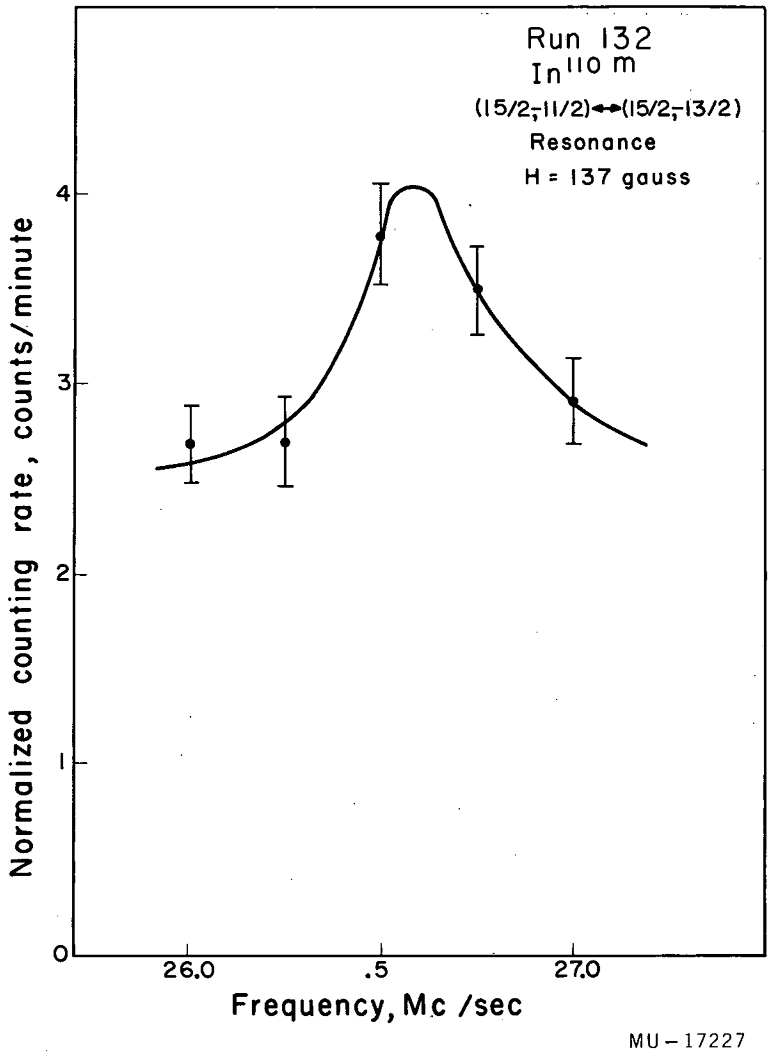

Fig. 33. In^{110m} (15/2, -11/2) ↔ (15/2, -13/2) resonance.

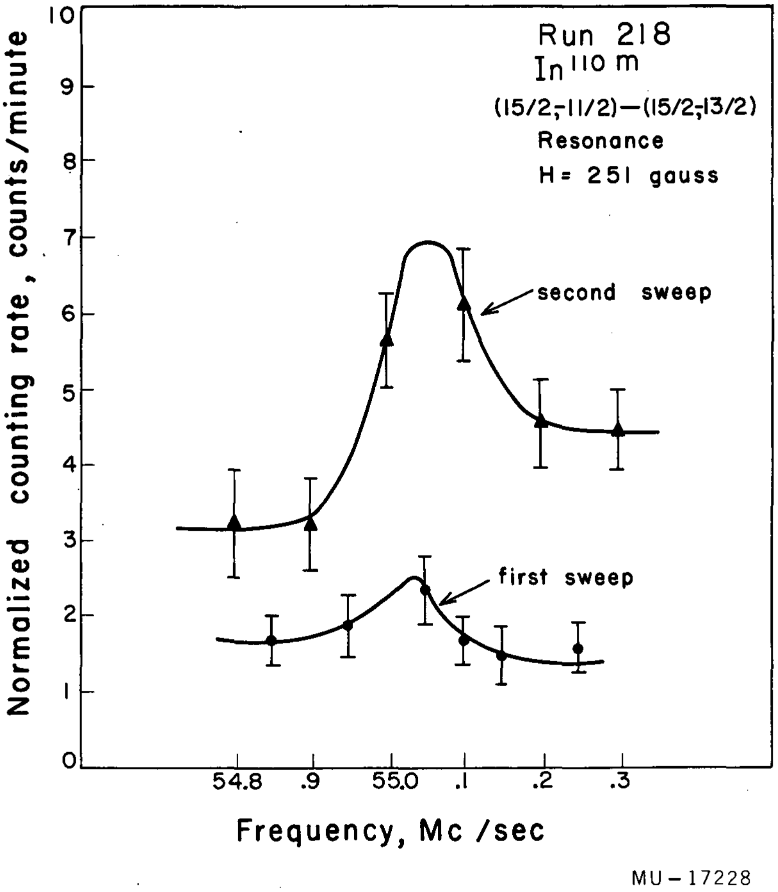

Fig. 34. In^{110m} (15/2, -11/2) ↔ (15/2, -13/2) resonance.

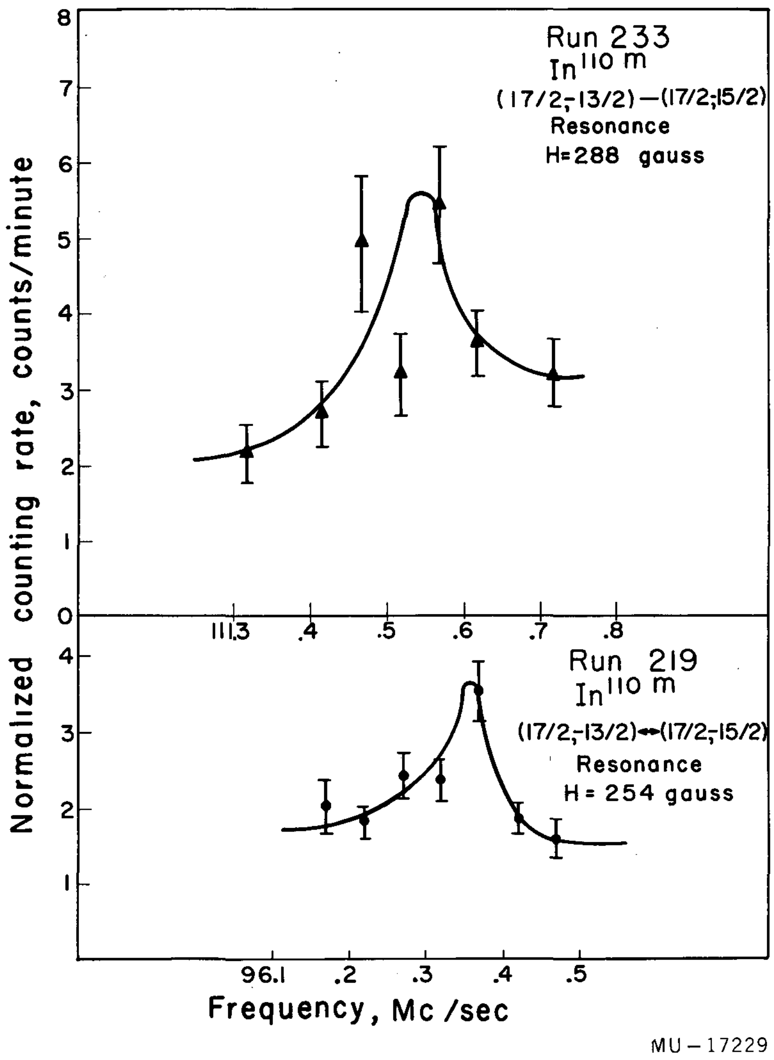

Fig. 35. In^{110m} (17/2, -13/2) ↔ (17/2, -15/2) resonances.

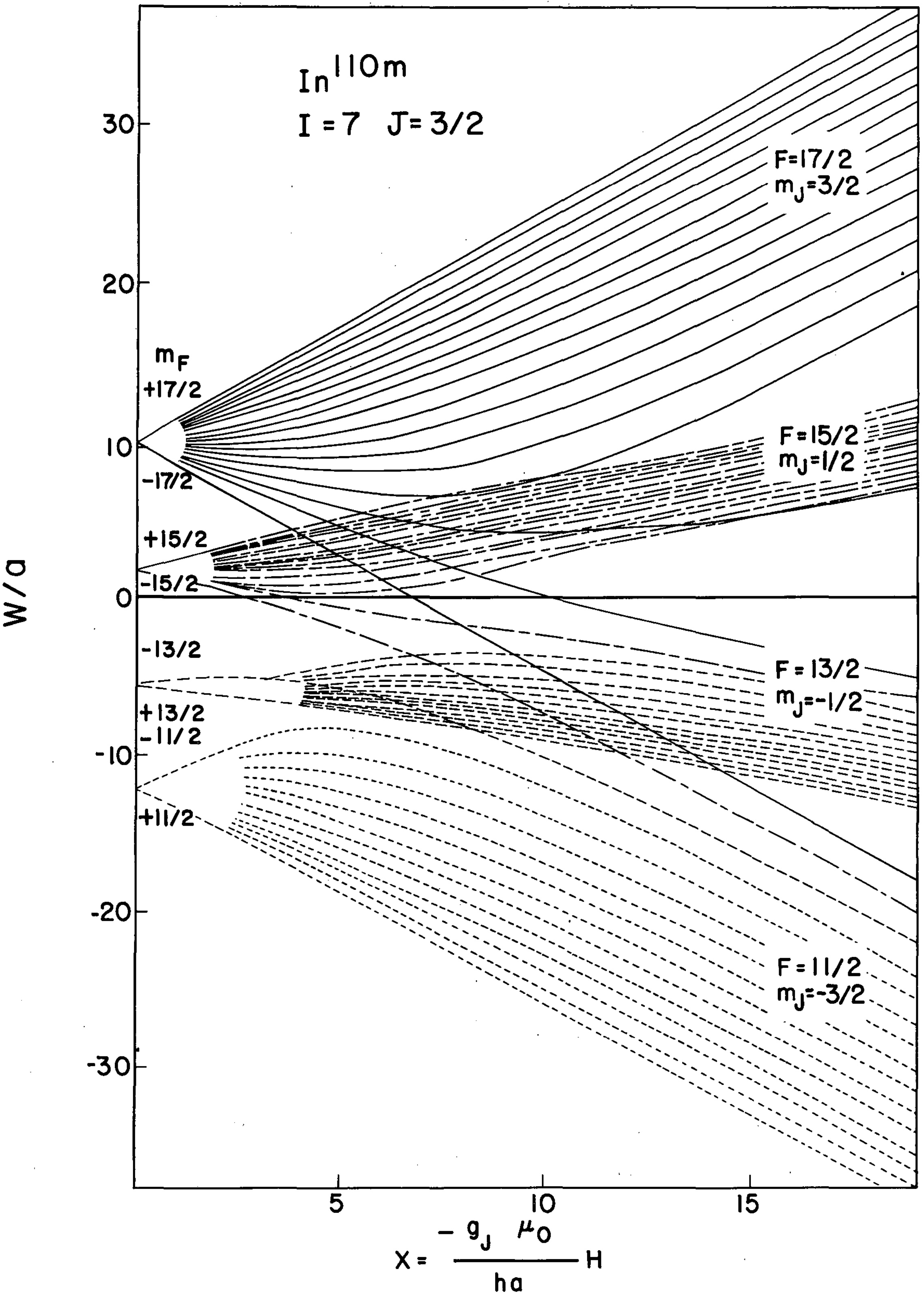

MUB-276

Fig. 36. Energy level diagram for In^{110m}.

For a negative magnetic moment the corresponding quantities are

$$a = -301.4(1.3) \text{ Mc/sec},$$

$$b = 120(17) \text{ Mc/sec},$$

$$\xi = -0.399(57) \qquad \mu = -10.7(1)\text{nm}, \qquad Q = +0.311\times 10^{-24} \text{cm}^2.$$

The resonances in Fig. 35 are not as "clean" as those preceding, but their inclusion or omission does not change the results significantly.

b. $\underline{\text{In}^{109}}$

Figures 37 to 42 present the data used to determine the interaction constants for In^{109}. Results are:

For a positive magnetic moment;

$$a = 242.38(56) \text{ Mc/sec},$$

$$b = 462.1(6.4) \text{ Mc/sec},$$

$$\chi^2 = 1.258,$$

$$\xi = +1.907(27),$$

$$\mu = +5.53(6) \text{ nm}$$

$$Q = +1.20 \times 10^{-24} \text{ cm}^2;$$

For a negative magnetic moment;

$$a = -243.79(57) \text{ Mc/sec},$$

$$b = -469.8(6.6) \text{ Mc/sec},$$

$$\chi^2 = 2.449,$$

$$\xi = +1.927(27),$$

$$\mu = -5.57(6) \text{ nm},$$

$$Q = -1.22\times 10^{-24}\text{cm}^2.$$

It is concluded from the χ^2 of fit that a positive moment best fits the data. The energy levels are plotted in Fig. 43 for μ_I positive.

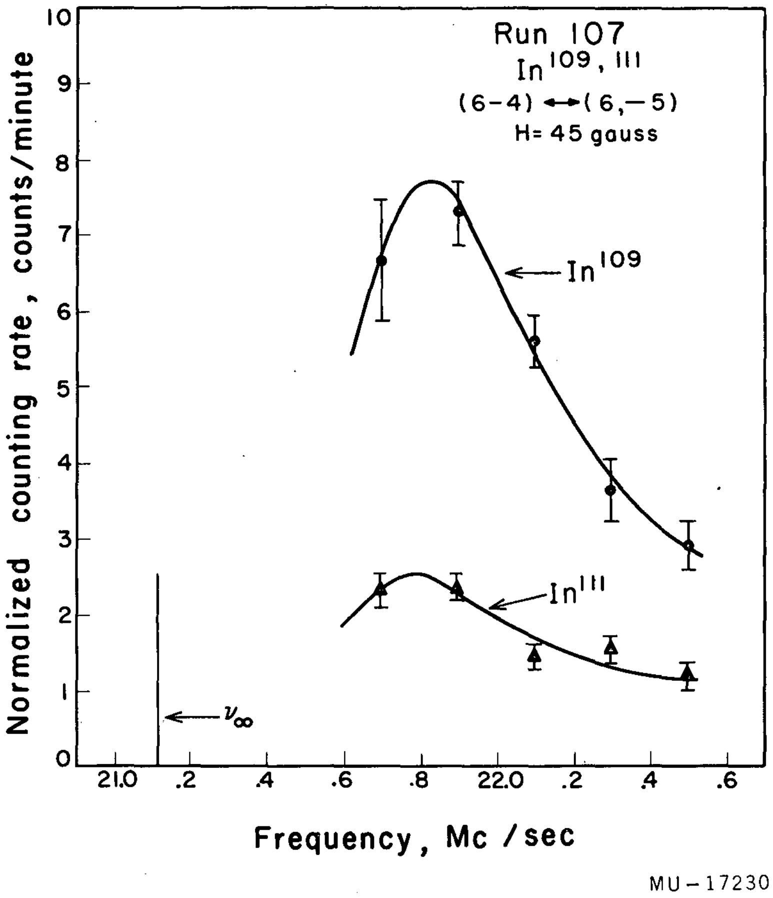

Fig. 37. $In^{109,111}$ (6, -4) ↔ (6, -5) resonance.

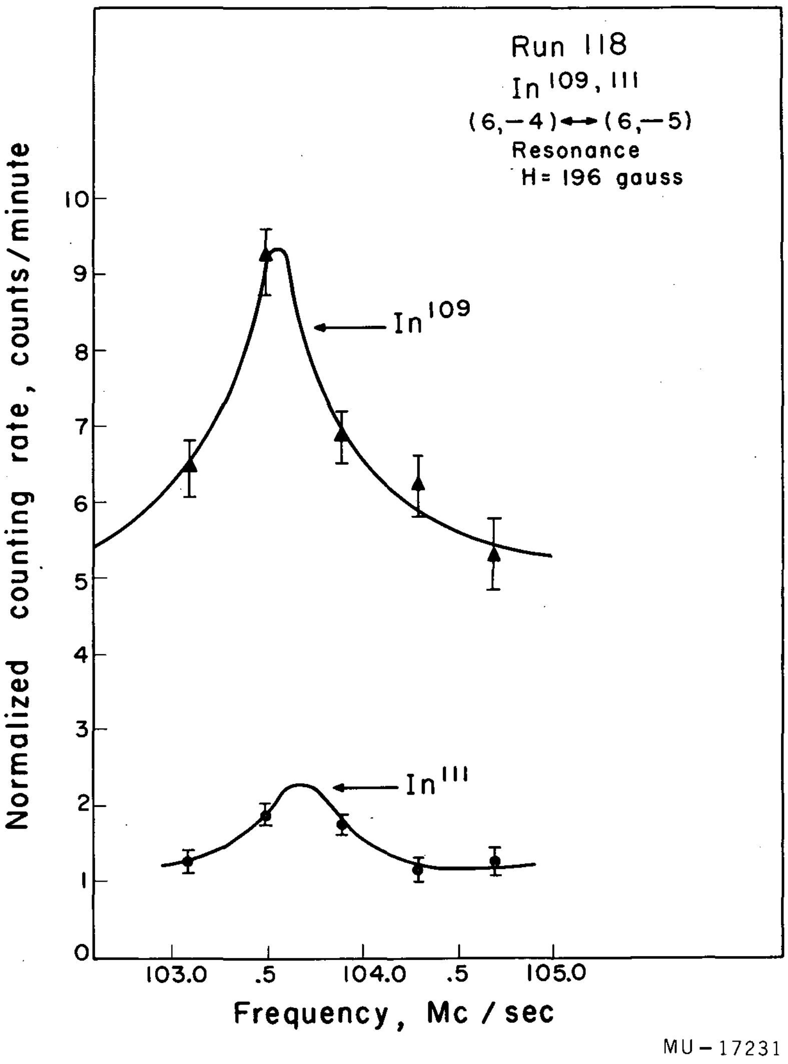

Fig. 38. $In^{109,111}$(6, -4) ↔ (6, -5) resonance.

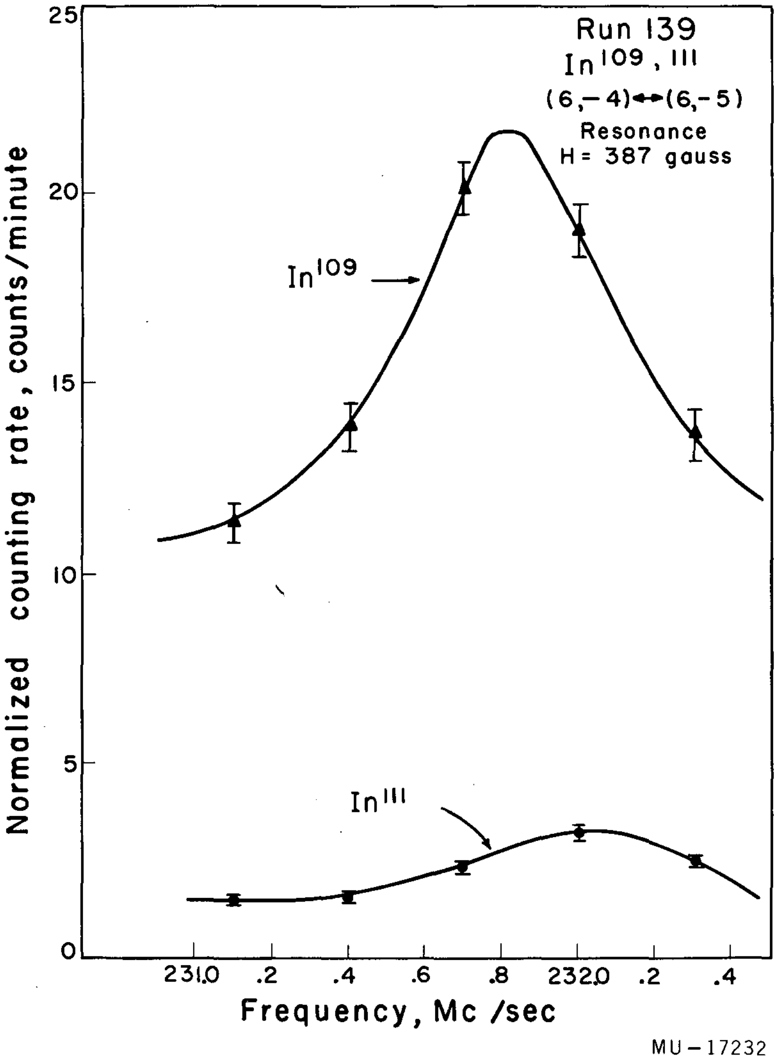

Fig. 39. $In^{109, 111}$ (6, -4) ↔ (6, -5) resonance.

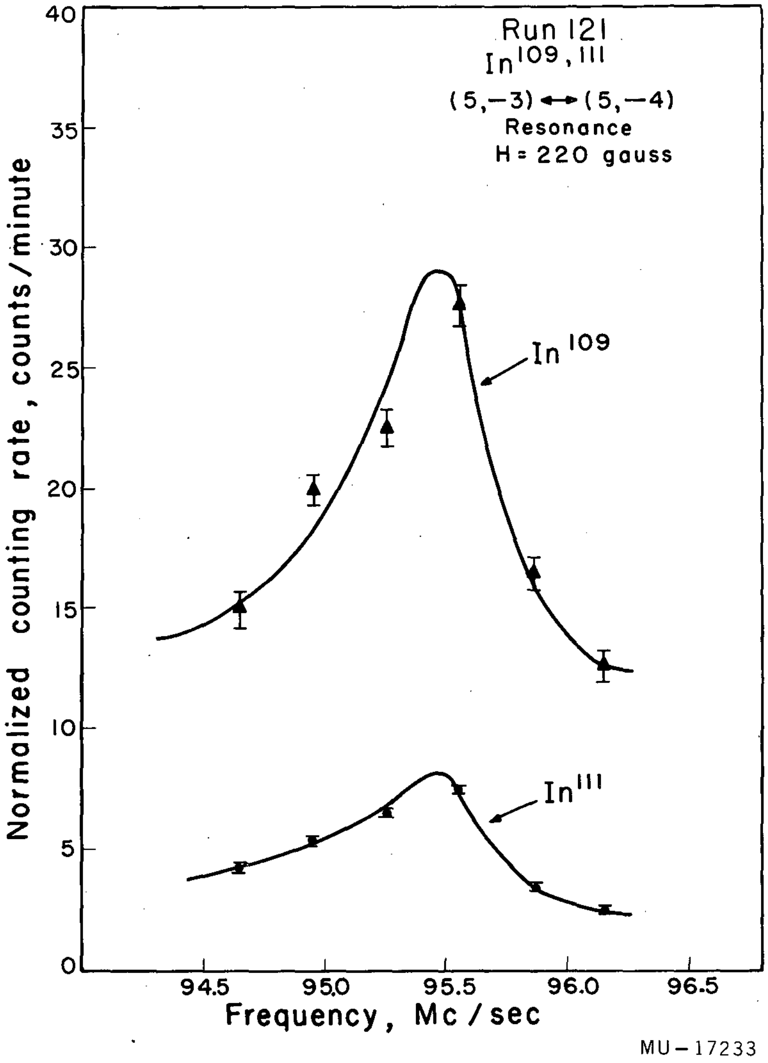

Fig. 40. $In^{109, 111}$(5, -3) ↔ (5, -4) resonance.

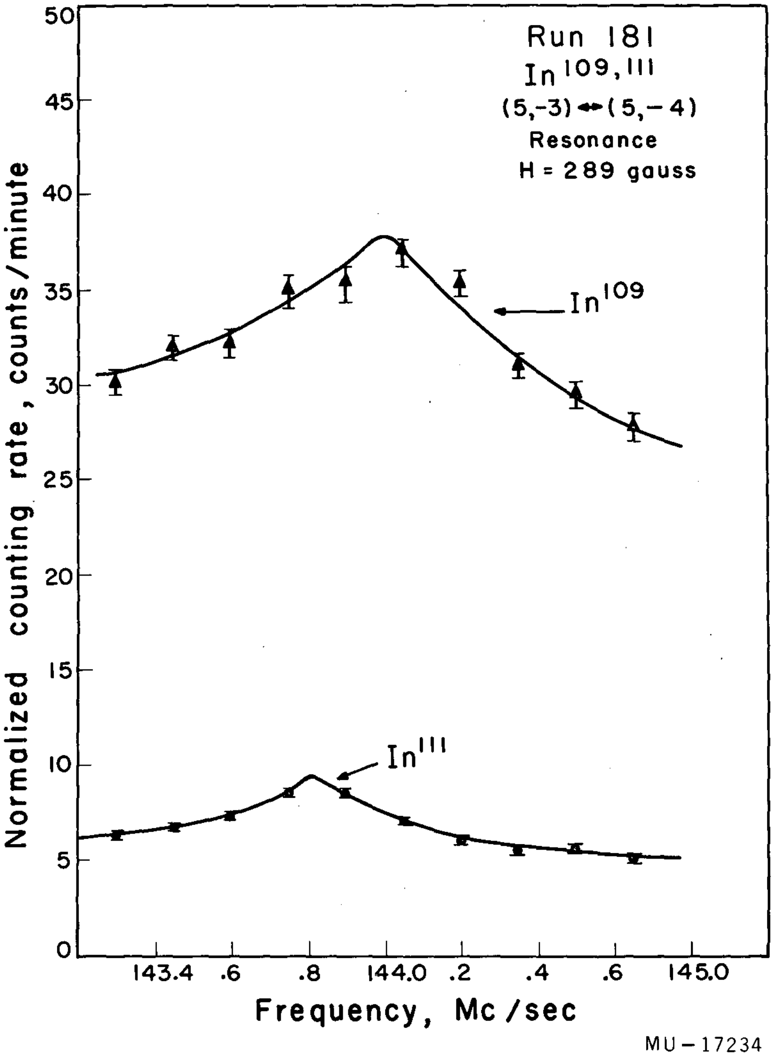

Fig. 41. $In^{109,111}$(5, -3) ↔ (5, -4) resonance.

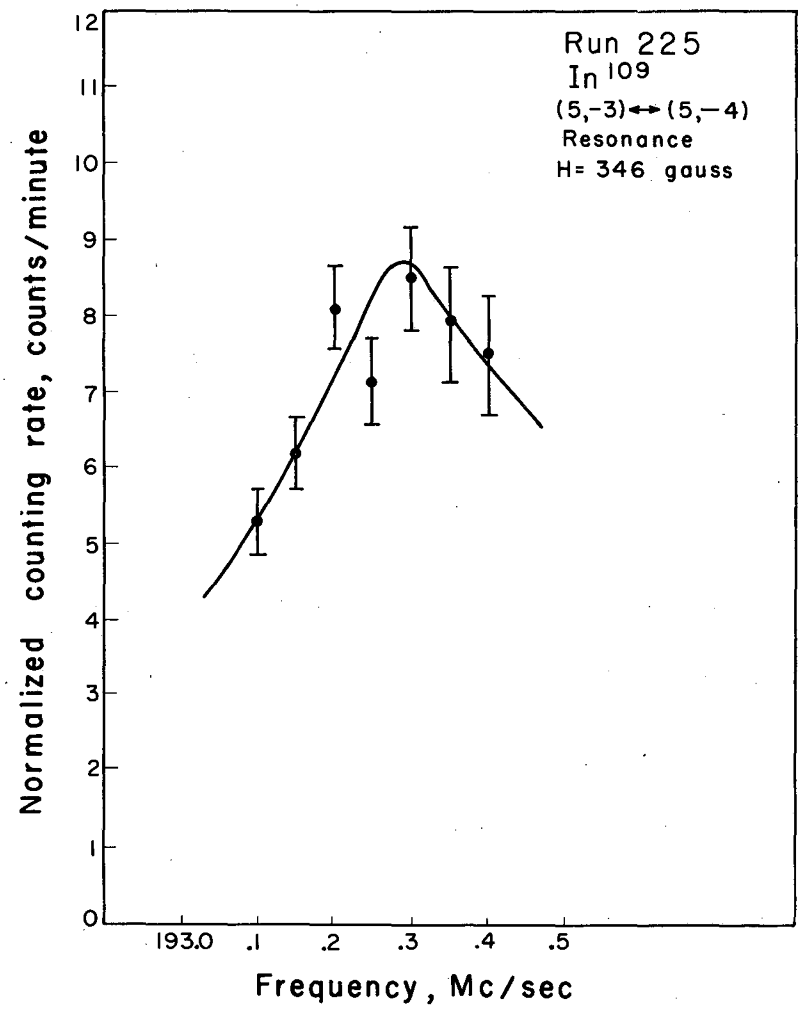

MU-17235

Fig. 42. In^{109} (5, -3) ↔ (5, -4) resonance.

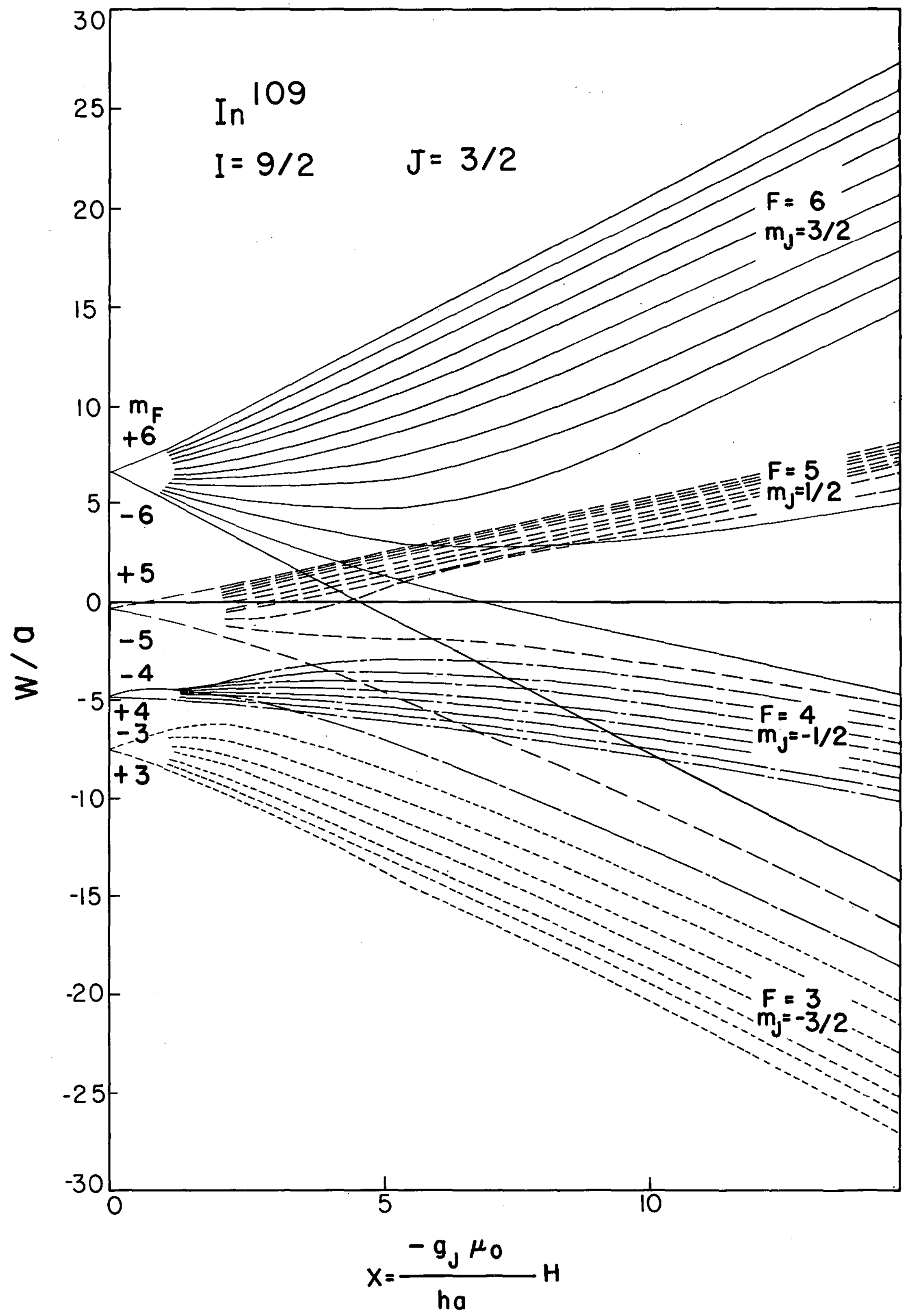

MUB-275

Fig. 43. Energy level diagram for In^{109}.

c. In^{111}

The experimental data for In^{111} are presented in Figs. 37 through 41 and 44 through 46. The In^{111} resonances in Fig. 37 through 41 were obtained by "decaying" the In^{109} resonances. In Fig. 37, the resonances are unresolved at 45 gauss. In Figs. 38 and 39, the In^{111} resonance is shifted upward in frequency from the In^{109} resonance curve. The lower resonance shown in Fig. 40 is unresolved. In Fig. 41, the In^{111} resonance is shifted downward in frequency from the In^{109} resonance. Figures 44 through 46 present the results of runs on essentially pure In^{111}. Resonance half widths vary considerably due to changes in the hairpin during the course of the investigation. Results are:

For a positive magnetic moment

$a = 241.78(30)$ Mc/sec,

$b = 455.3(3.4)$ Mc/sec,

$\chi^2 = 0.921$,

$\xi = +1.883(14)$,

$\mu = +5.53(6)$ nm,

$Q = +1.18 \times 10^{-24}\ \mathrm{cm}^2$;

For a negative magnetic moment

$a = -243.22(30)$ Mc/sec,

$b = -465.9(3.5)$ Mc/sec,

$\chi^2 = 1.219$,

$\xi = +1.916(15)$,

$\mu = -5.56(6)$ nm,

$Q = -1.21 \times 10^{-24}\ \mathrm{cm}^2$.

A positive magnetic moment fits the data best.

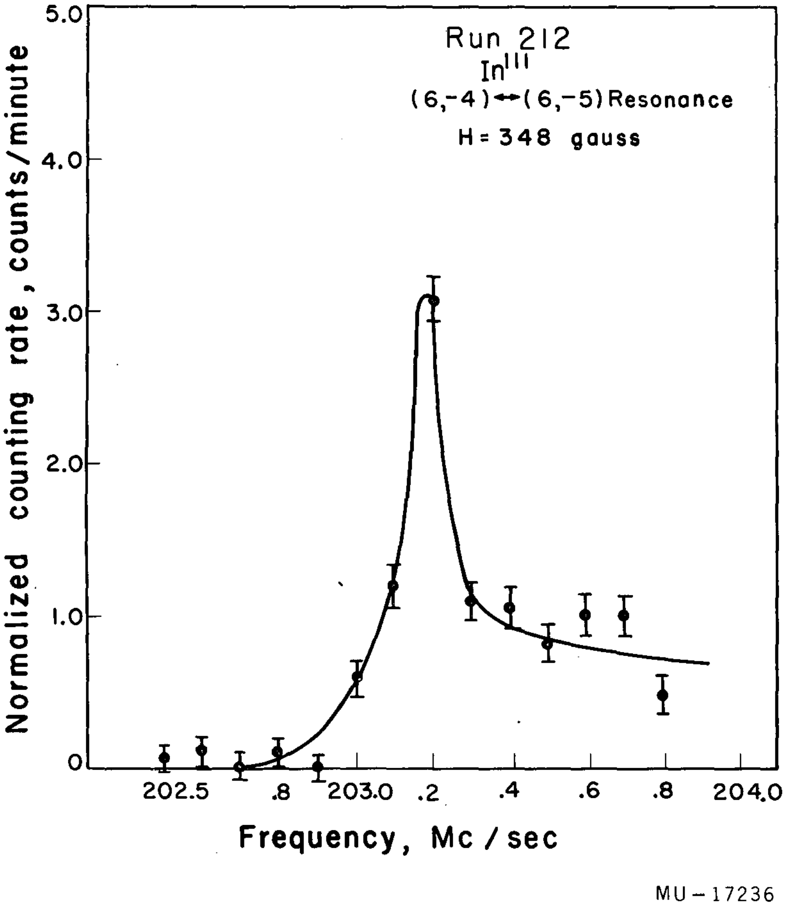

Fig. 44. In^{111} (6, -4) ↔ (6, -5) resonance.

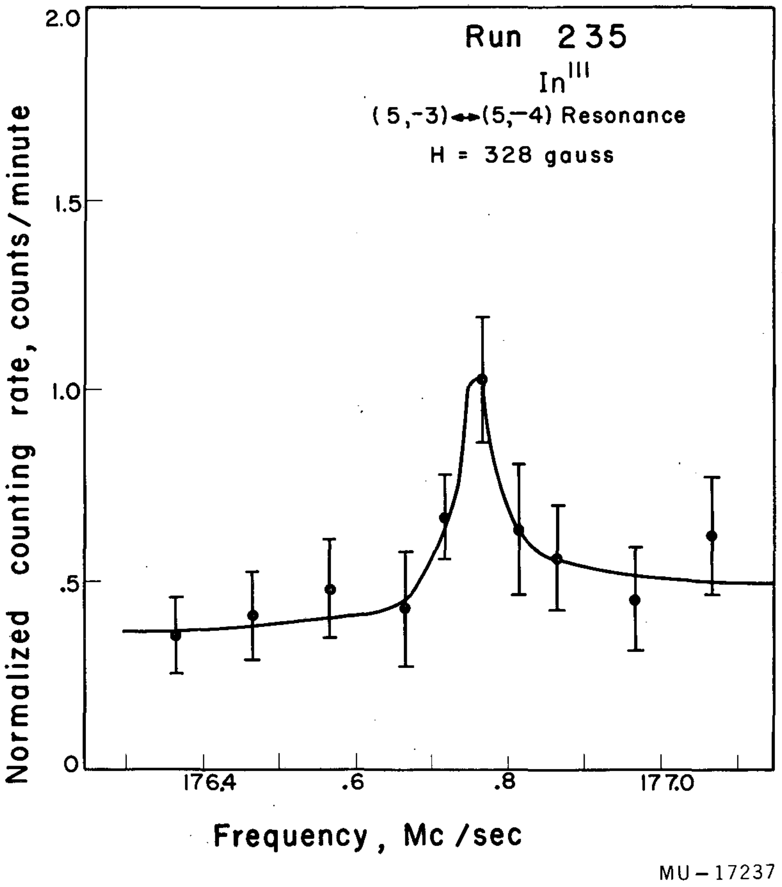

Fig. 45. In^{111}(5, -3) ↔ (5, -4) resonance.

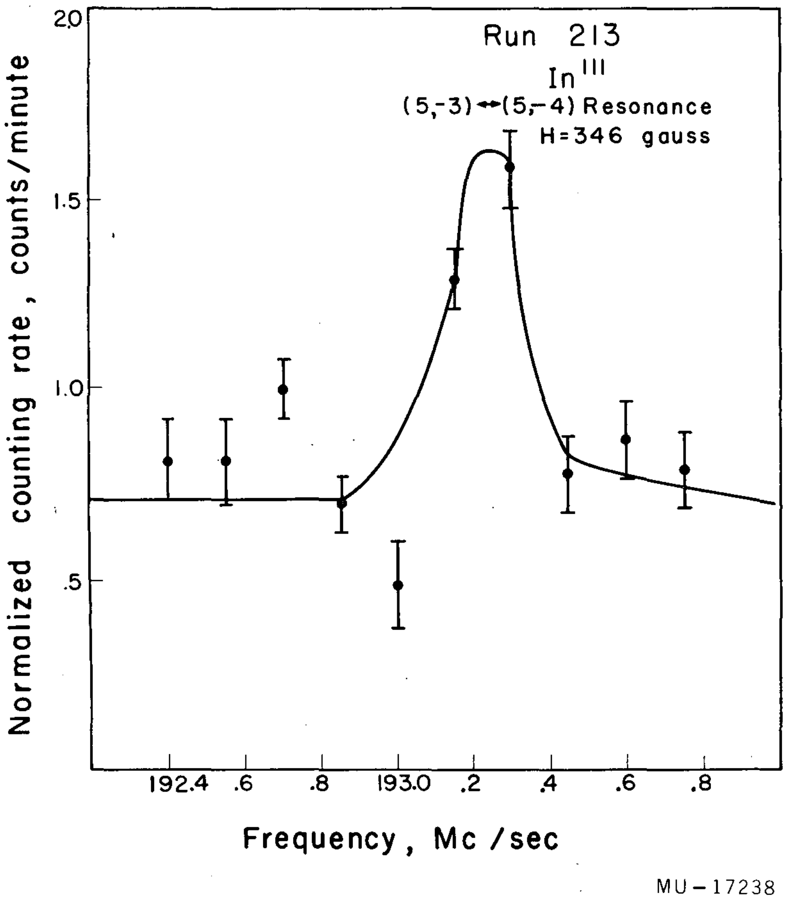

Fig. 46. In^{111} (5, -3) ↔ (5, -4) resonance.

The moments of the above three isotopes were calculated from Eqs. (92) and (93) by using the following data:

<u>In^{115}</u>

$a = 242.164807(23)$ Mc/sec,[41]

$b = 449.54568(21)$ Mc/sec,[41]

$\mu = +5.53441(66)$[1],

$Q = 1.166 \times 10^{-24}$ cm^2,[42, 37]

$I = 9/2$,

<u>In^{113}</u>

$a = 241.641040(58)$ Mc/sec,[41]

$b = 443.41568(52)$ Mc/sec,[41]

$\mu = 5.52317(54)$ nm,[1]

$Q = 1.144 \times 10^{-24}$ cm^2,[42, 37]

$I = 9/2$,

<u>In^{114m}</u>

$\mu = 4.7$ nm,[39]

$I = 5$,[40]

<u>In^{116m}</u>

$\mu = 4.4$ nm,[39]

$I = 5$.[40]

ACKNOWLEDGMENTS

It is a pleasure to acknowledge my indebtedness to Professor W. A. Nierenberg. His boundless energy and enthusiasm have been a constant source of inspiration. I also wish to thank Professor H. A. Shugart for being always available for discussion and assistance during the entire course of the research. I am certain that his generous advice saved many hours of fruitless endeavor. Many hours were spent in discussion and conducting experiments with W. B. Ewbank, F. R. Petersen, and V. Ehlers.

I must express gratitude to my wife for so patiently enduring the trying life of a graduate student's wife and for her supporting courage when mine faltered.

Thanks also go to my mother for nurturing my original interest in higher education.

This work was made possible through the financial assistance of the U. S. Atomic Energy Commission.

APPENDIX I:

Properties of Matrices Used in Atomic Beams

1. Size: $(2J+1)(2I+1)$.
2. Size of largest submatrix: $(2J+1)$.
3. Number of elements of largest submatrix connected by $\Delta F = 0$: $(2J+1)$.
4. Number of elements of largest submatrix connected by $\Delta F = \pm 1$: $4J$.
5. Total number of nonzero elements of largest submatrix: $6J+1$.
6. Total number of zero elements of largest submatrix: $2J(2J-1)$.
7. Equivalent size of the doubly repeated submatrices: $2J(2J+1)$.
8. Total number of elements in all the doubly repeating submatrices: $\frac{2J(2J+1)(4J+1)}{3}$.
9. Number of elements of all the doubly repeated submatrices connected by $\Delta F = 0$: $2J(2J+1)$.
10. Number of elements of all the doubly repeated submatrices connected by $\Delta F = \pm 1$: $4J(2J-1)$.
11. Total number of nonzero elements in all the doubly repeated submatrices: $2J(6J-1)$.
12. Total number of zero elements in all the doubly repeated submatrices:
$$\frac{2J}{3}\left[(2J+1)(4J+1) - 3(6J-1)\right].$$
13. Equivalent size of the largest repeating submatrices: $(2J+1)[2(I-J)+1]$.
14. Number of largest submatrices: $2(I-J)+1$.
15. Total number of nonzero elements in the entire matrix: $2I(6J+1) + 2J+1$.
16. Total number of zero elements in the entire matrix: $(2J+1)[(2J+1)(2I+1)^2 - 1] - 2I(6J+1)$.

All the above is for the case $J < I$. For $I < J$, replace I by J and J by I.

APPENDIX II:

Zero-External Field Curves of W' vs ξ

Zero-external-field curves of W' vs ξ for $J = 3/2$, $I = 1$ to $I = 9$ are shown in Figs. A1 through A17.

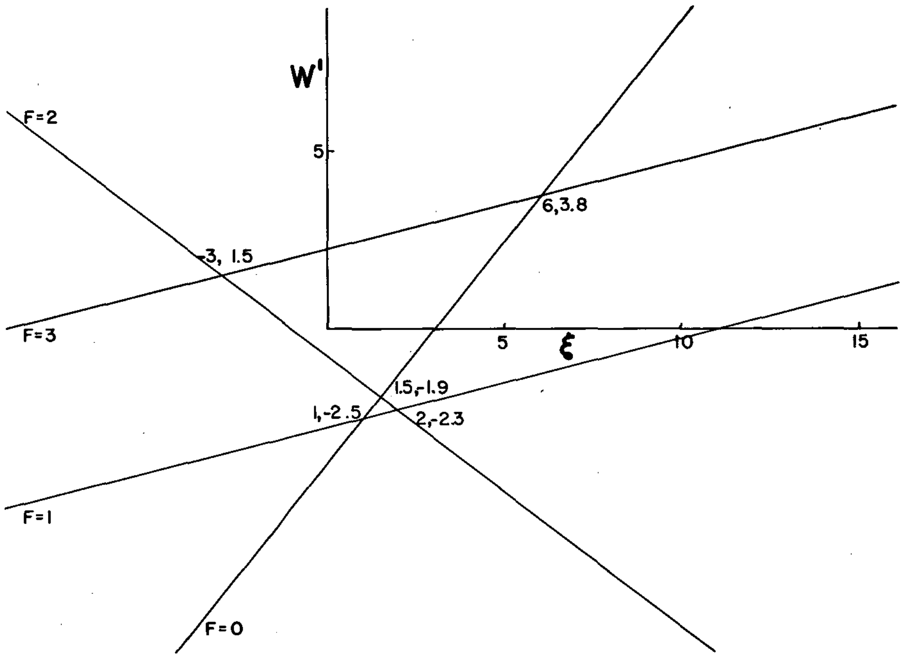

MU-17203

Fig. A1. $I = 3/2$, $J = 3/2$.
Note: Intersections to nearest 10th. For exact numbers see Table II.

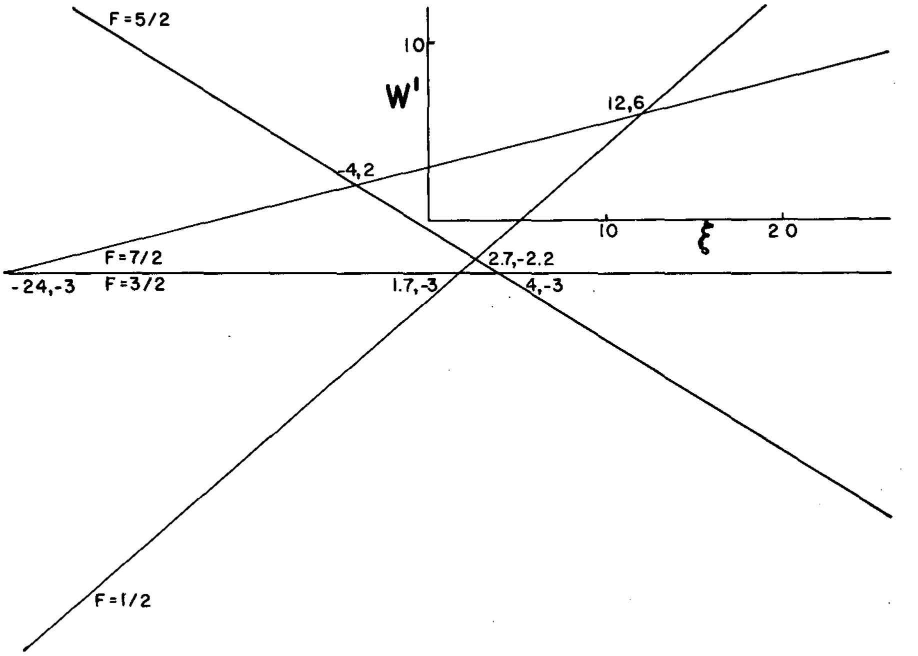

MU-17204

Fig. A2. I = 2, J = 3/2.

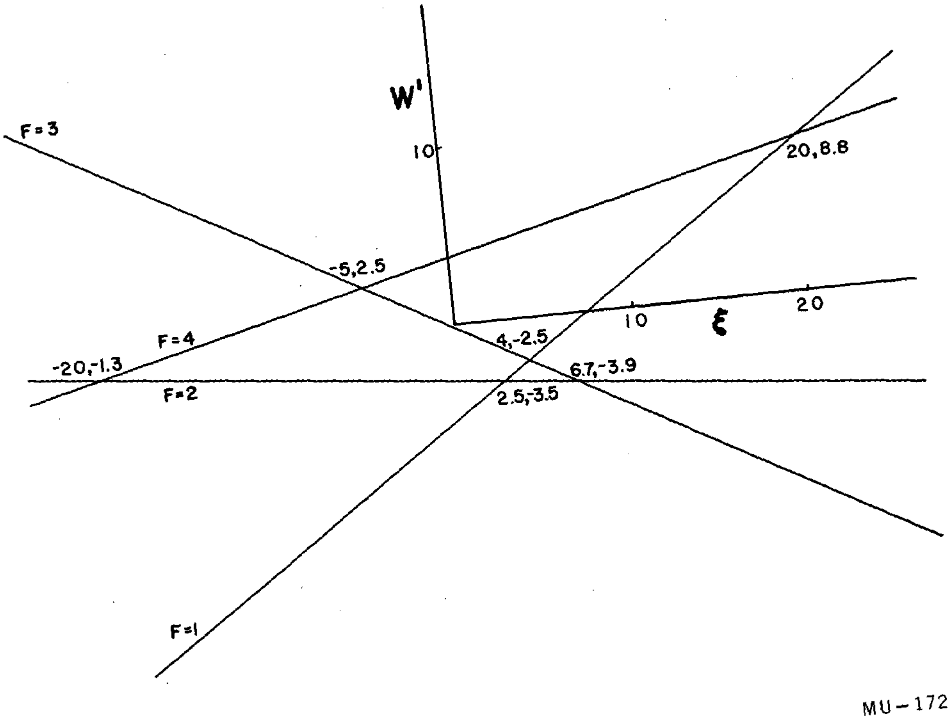

Fig. A3. I = 5/2, J = 3/2.

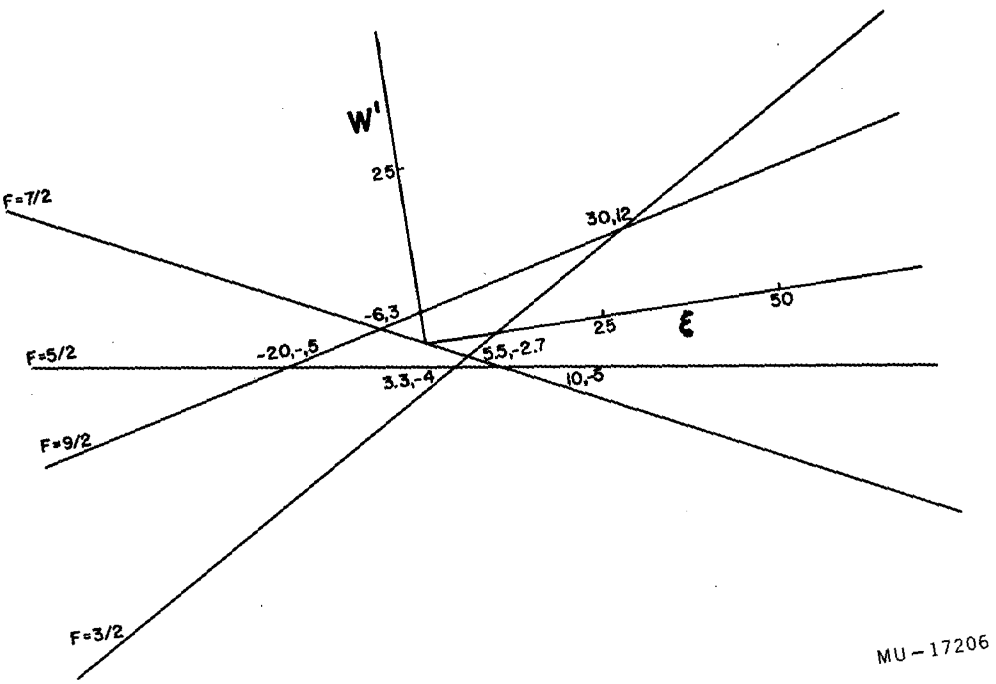

Fig. A4. I = 3, J = 3/2.

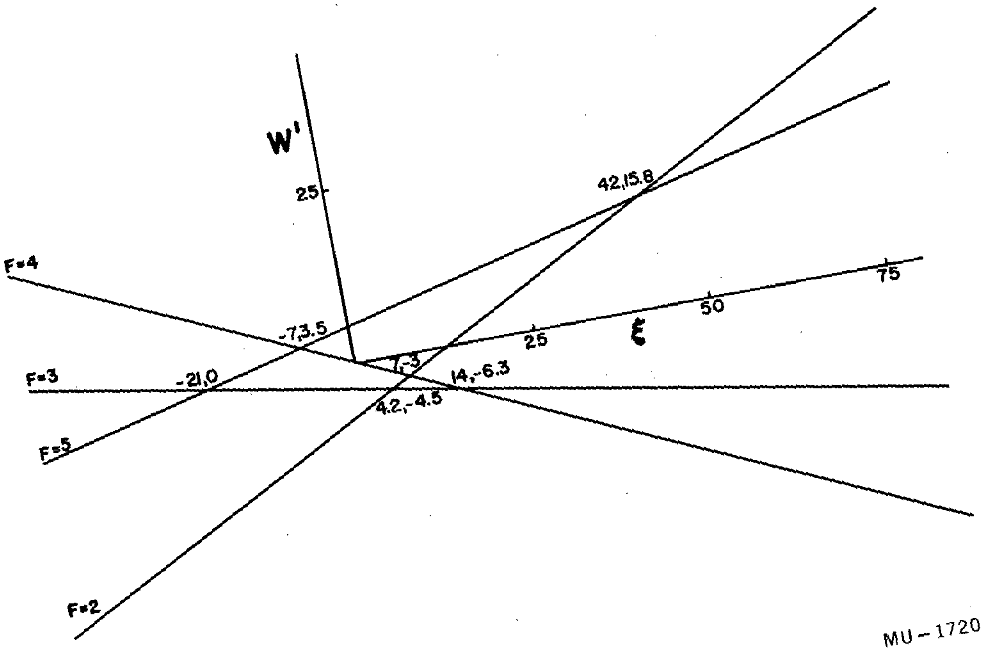

MU-17207

Fig. A5. I = 7/2, J = 3/2.

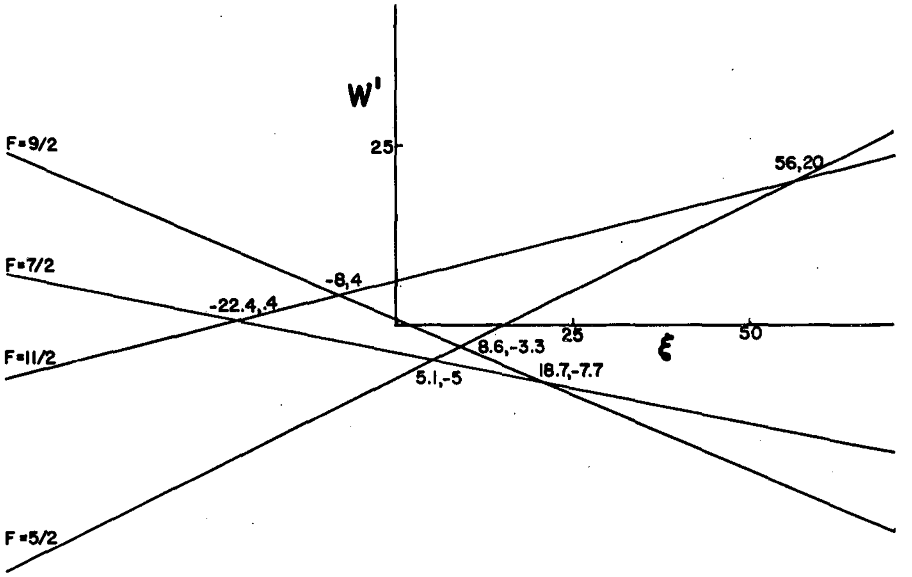

MU-17208

Fig. A6. I = 4, J = 3/2.

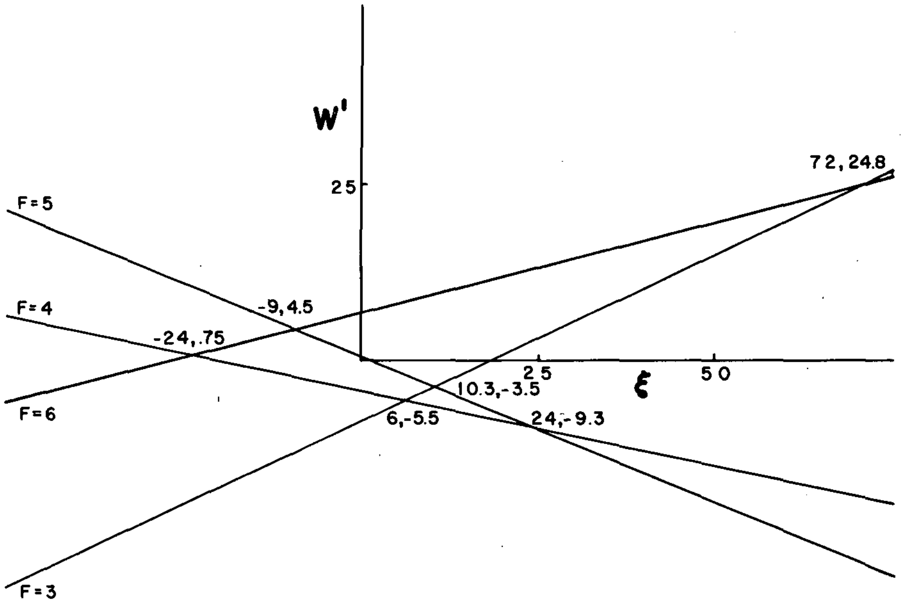

MU-17209

Fig. A7. I = 9/2, J = 3/2.

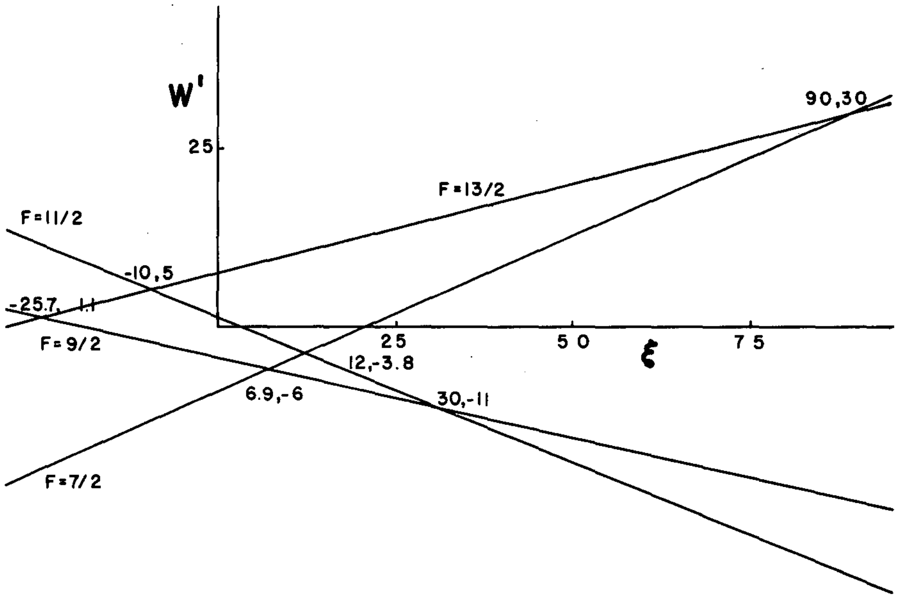

MU-17210

Fig. A8. I = 5, J = 3/2.

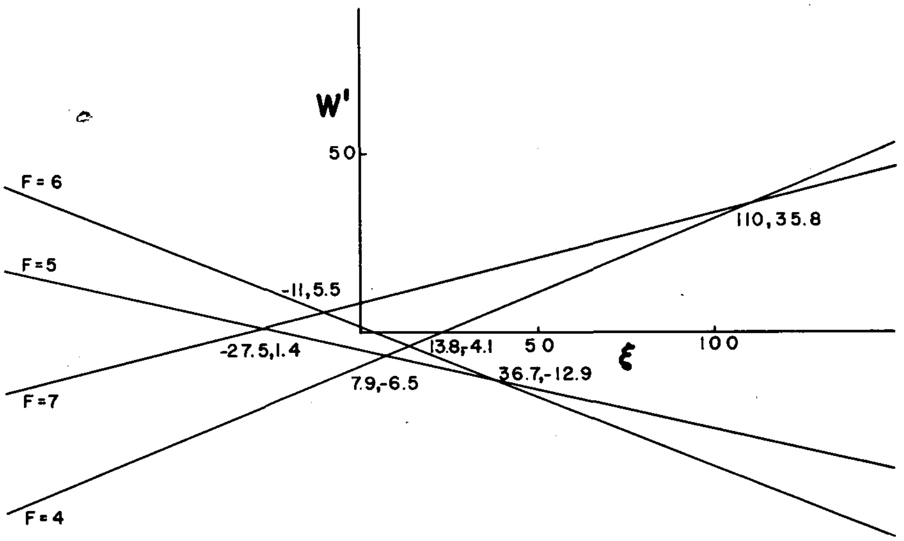

MU-17211

Fig. A9. I = 11/2, J = 3/2.

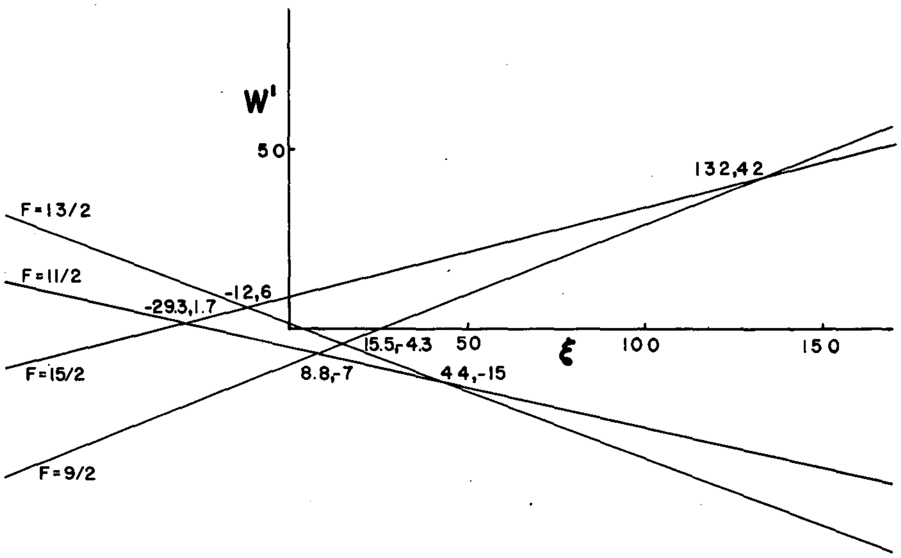

MU-17212

Fig. A10. I = 6, J = 3/2.

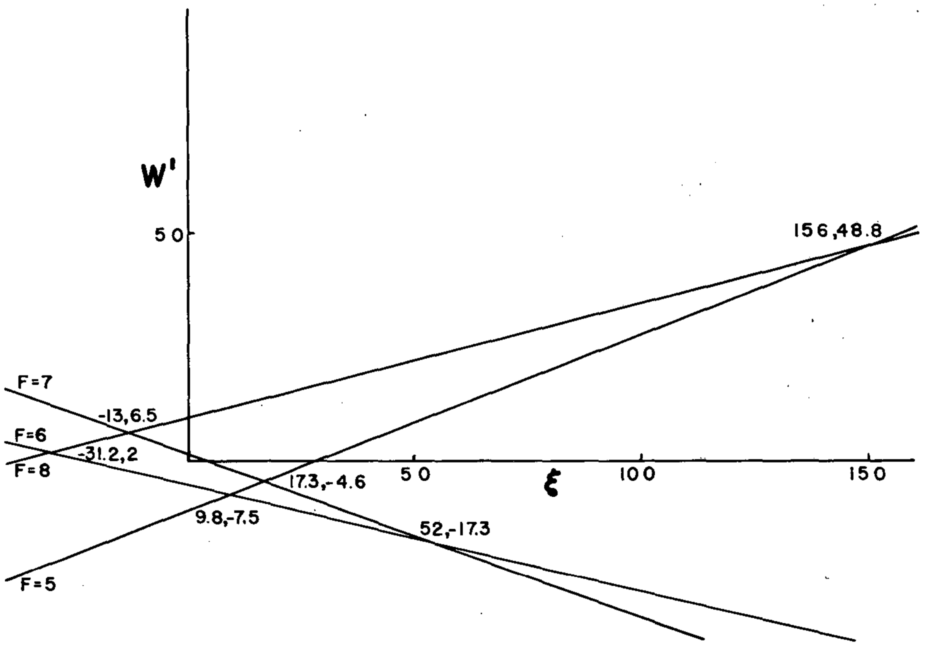

MU-17213

Fig. A11. I = 13/2, J = 3/2.

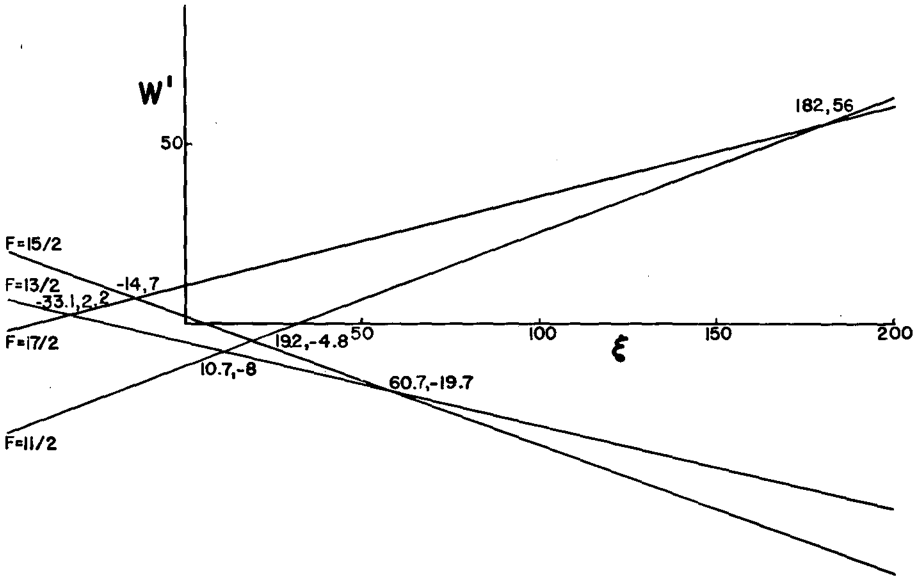

MU-17214

Fig. A12. I = 7, J = 3/2.

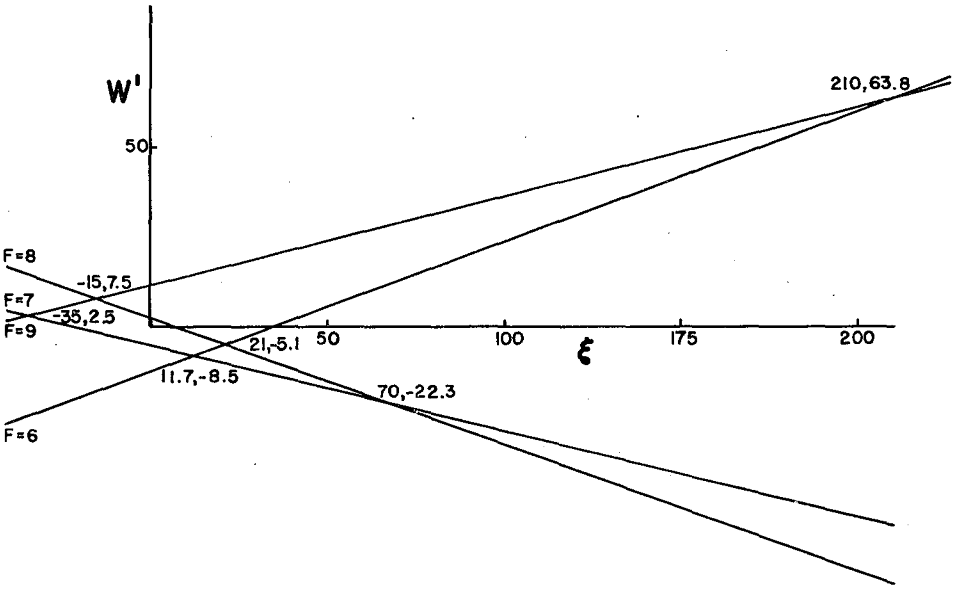

MU-17215

Fig. A13. I = 15/2, J = 3/2.

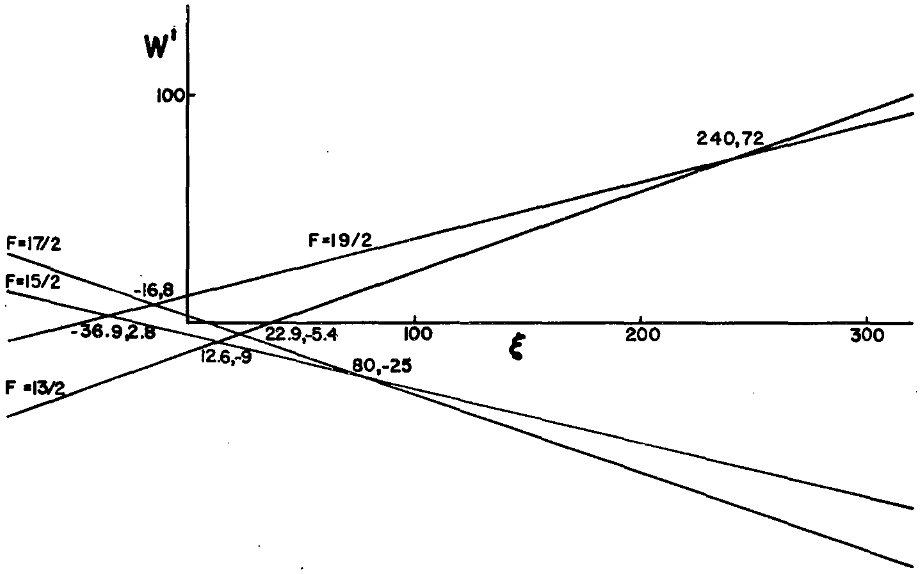

MU-17216

Fig. A14. I = 8, J = 3/2.

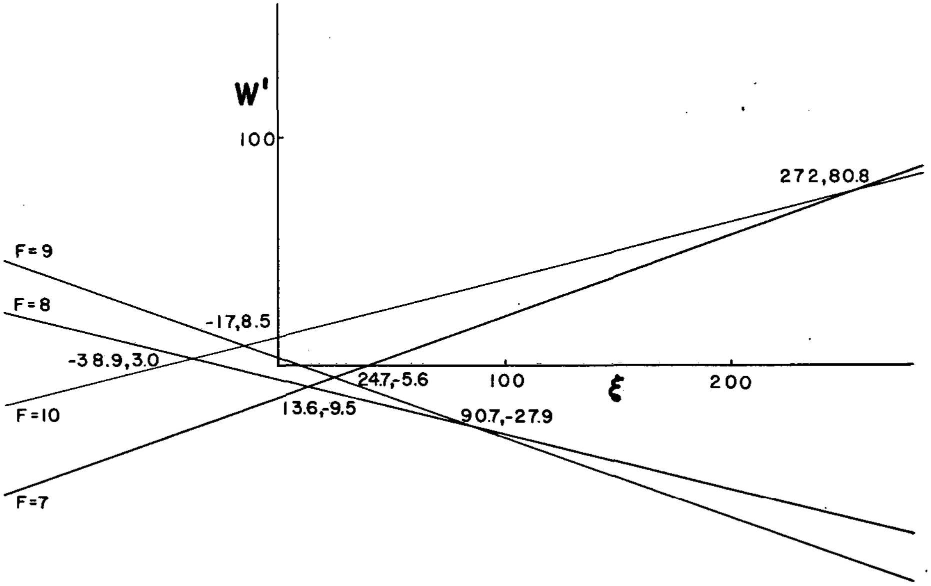

MU-17217

Fig. A15. I = 17/2, J = 3/2.

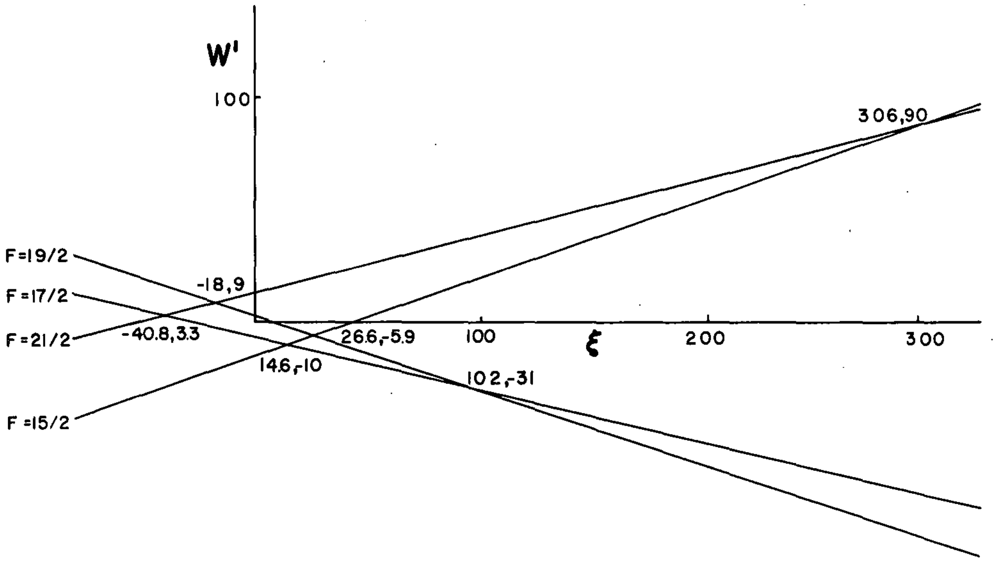

MU-17218

Fig. A16. I = 9, J = 3/2.

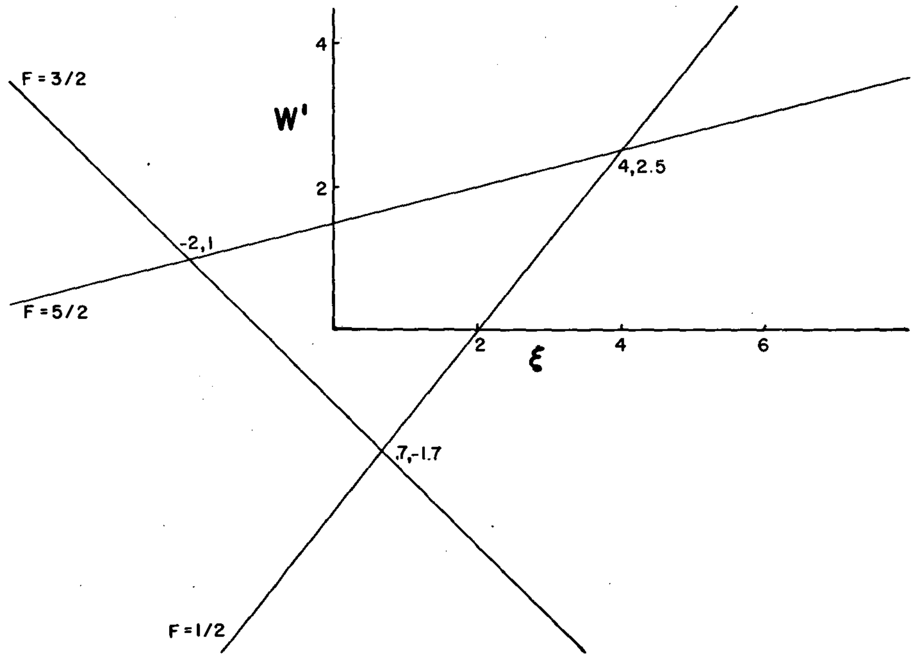

MU-17219

Fig. A17. I = 1, J = 3/2.
Note: Intersections to nearest 10th. For exact numbers see Table III.

APPENDIX III:

Transition Probability for a Spin-1/2 System

In this section, an attempt is made to gain some insight into the concept of a resonant frequency causing the transition of a system from one quantum state to another. The system is a very simple one consisting of a particle whose angular momentum I = 1/2 may be aligned either parallel or antiparallel to a magnetic field H. The treatment follows that by Ramsey.[1, 8]

Classical Treatment

The particle precesses about H, due to the torque exerted, according to

$$\hbar \frac{d\vec{I}}{dt} = \vec{\mu} \times \vec{H} = \gamma_I \hbar \vec{I} \times \vec{H}, \tag{A1}$$

where all symbols have been defined previously.

A transformation may be made to a coordinate system rotating about the field H via the equation

$$\frac{d\vec{I}}{dt} = \frac{\partial \vec{I}}{\partial t} + \vec{\omega} \times \vec{I}, \tag{A2}$$

where the left side refers to the fixed system and the right side to the rotating system; ω is the angular velocity with which the coordinate system rotates.

Equations (A1) and (A2) may be combined to give

$$\frac{\partial \vec{I}}{\partial t} = \gamma_I \vec{I} \times \left(\vec{H} + \frac{\vec{\omega}}{\gamma_I} \right) = \gamma_I \vec{I} \times \vec{H}_e , \tag{A3}$$

where $\vec{H}_e = \vec{H} + \dfrac{\vec{\omega}}{\gamma_I}$ is the effective field seen in the rotating system. We now specify H more carefully. It is composed of two parts. One part is the external C field H_0, the other is a magnetic field rotating with angular velocity $\vec{\omega}$ and is similar to the field in the radiofrequency hairpin; $\vec{\omega}$ is chosen to rotate in the same direction as the spin precession. In a coordinate system fixed with respect to H_1 there is no time variation of the magnetic field H_1. Thus we have

$$\vec{H} = \vec{H}_0 + \vec{H}_1 = H_0\,\vec{k} + H_1\,\vec{i}, \tag{A4}$$

$$\vec{\omega} = -\omega\vec{k}.$$

The above relations are illustrated in Fig. A18.

Therefore, the effective field becomes

$$\vec{H}_e = (H_0 - \frac{\omega}{\gamma_I})\,\vec{k} + H_1\,\vec{i}, \tag{A5}$$

$$\left|\vec{H}_e\right| = \sqrt{(H_0 - \frac{\omega}{\gamma_I})^2 + (H_1)^2} = \frac{b}{\gamma_I}, \tag{A6}$$

where $b = \sqrt{(\omega_0 - \omega)^2 + \omega_1{}^2}$ is the precession frequency of the particle about the effective field.

Then we have $\omega_1 = \gamma_I H_1$ and $\omega_0 = \gamma_I H_0$ = Lamour frequency of precession of the particle about H_1 and H_0 respectively (Fig. A19a).

We can also write

$$\cos\theta = \frac{\omega_0 - \omega}{b}, \qquad \sin\theta = \frac{\omega_0(H_1/H_0)}{b}. \tag{A7}$$

At $\omega = \omega_0$, $\theta = 90^\circ$ and $H_e = H_1$, therefore I precesses only about H_1 and may change its orientation from "spin up" to "spin down." By transforming to another coordinate system rotating about H_e with angular velocity = a, it is possible to preserve the spin direction constant in space. The resultant quantities are shown in Fig. A19b. At resonance $\vec{H}_e{}' = 0$, $\gamma_I H_e = a$ and $a = b$.

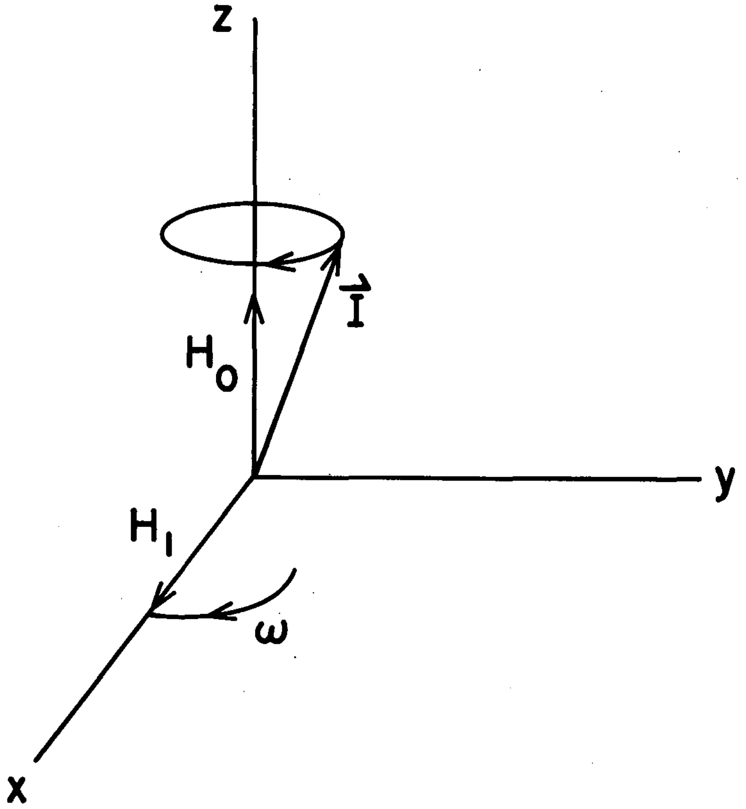

MU-17239

Fig. A18. H_1 rotates with angular velocity $\vec{\omega}$, where $\vec{\omega}$ is in the direction of rotation of the rotating coordinate system.

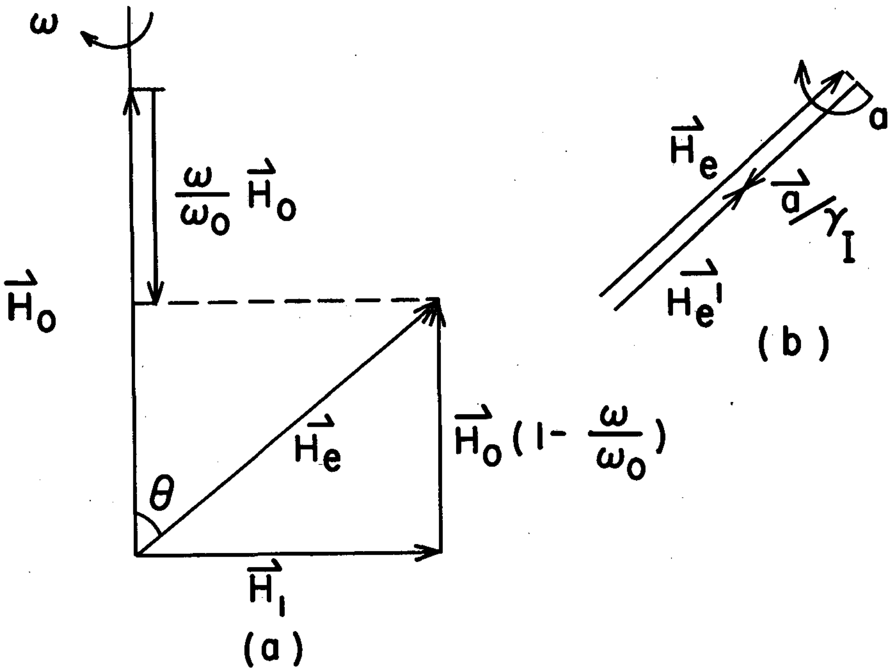

MU-17240

Fig. A19. Effective magnetic field in first rotating coordinate system (a) and the second rotating coordinate system (b).

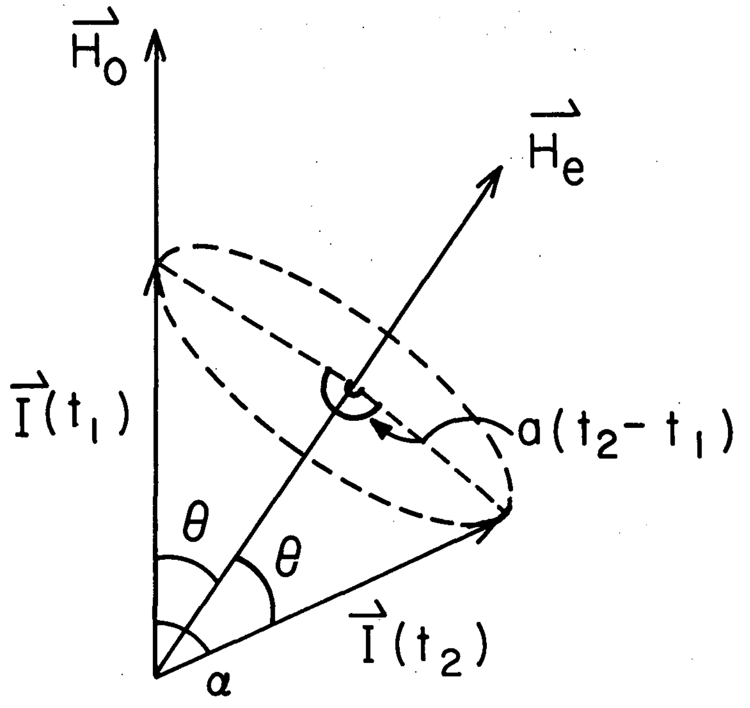

MU-17241

Fig. A20. Time variation of I in its precession about the effective magnetic field H_0. The precession velocity is a.

Variation of the Precession as a Function of Time

At time t_1, I is parallel to H_0. At time t_2, I has precessed α degrees from H_0 (Fig. 20). Setting $\theta_1 = \theta_2 = 0$ and $\phi_1 - \phi_2 = a\ (t_2 - t_1)$ in the well known relation

$$\cos\alpha = \cos\theta_1 \cos\theta_2 + \sin\theta_1 \sin\theta_2 (\cos\phi_1 \cos\phi_2 + \sin\phi_1 \sin\phi_2),$$

we have

$$\cos\alpha = \cos^2\theta + \sin^2\theta \quad \cos[a(t_2 - t_1)] \quad . \tag{A8}$$

Equation (A8) may be placed in the form

$$\cos\alpha = 1 - 2\sin^2\theta \sin^2\left[\frac{a(t_2 - t_1)}{2}\right].$$

We may also write

$$\left.\begin{aligned} P_{1/2,\,1/2} + P_{1/2,\,-1/2} &= 1, \\ P_{1/2,\,1/2} - P_{1/2,\,-1/2} &= \cos\alpha, \end{aligned}\right\} \tag{A9}$$

where $P_{1/2,\,1/2}$ is the probability that the particle starts with spin up and still has its spin up after a time $t_2 - t_1$.

Equations (A7), (A8) and (A9) yield

$$\left.\begin{aligned} P_{1/2,\,-1/2} &= \frac{\omega_1^{\;2}}{\omega_1^{\;2} + (\omega_0 - \omega)^2} \sin^2 \frac{a(t_2 - t_1)}{2}, \\ P_{1/2,\,1/2} &= 1 - \frac{\omega_1^{\;2}}{\omega_1^{\;2} + (\omega_0 - \omega)^2} \sin^2 \frac{a(t_2 - t_1)}{2} . \end{aligned}\right\} \tag{A10}$$

Quantum-Mechanical Treatment

The Hamiltonian used is

$$\mathcal{H} = -g_I \mu \vec{I} \cdot \vec{H}, \tag{A11}$$

where

$$\vec{H} = H_0 \vec{k} + H_1(\vec{i} \cos \omega t + \vec{j} \sin \omega t) \tag{A12}$$

and

$$\vec{I} = \sigma_x \vec{i} + \sigma_y \vec{j} + \sigma_z \vec{k}. \tag{A13}$$

Here

$$\sigma_x = 1/2 \begin{pmatrix} 0 & 1 \\ 1 & 0 \end{pmatrix}, \quad \sigma_y = 1/2 \begin{pmatrix} 0 & -i \\ i & 0 \end{pmatrix}, \quad \sigma_z = 1/2 \begin{pmatrix} 1 & 0 \\ 0 & -1 \end{pmatrix}. \tag{A14}$$

The primary equation comes from the formalism of time-dependent perturbation theory,

$$i\hbar \frac{\partial \psi}{\partial t} = \mathcal{H} \psi, \tag{A15}$$

where ψ is a two-component eigenvector. That is,

$$\psi = \begin{pmatrix} a_{1/2} \\ a_{-1/2} \end{pmatrix} . \tag{A16}$$

Thus, Eq. (A15) becomes

$$i\hbar \begin{pmatrix} \dot{a}_{1/2} \\ \dot{a}_{-1/2} \end{pmatrix} = \frac{-g_I \mu}{2} \begin{vmatrix} H_0 & H_1 e^{-i\omega t} \\ H_1 e^{i\omega t} & -H_0 \end{vmatrix} \begin{pmatrix} a_{1/2} \\ a_{-1/2} \end{pmatrix} . \tag{A17}$$

Equation (A17) may be reduced to the form

$$\left. \begin{aligned} \dot{a}_{1/2} &= -\frac{i}{2} (\omega_0 a_{1/2} - \omega_1 e^{-i\omega t} a_{-1/2}), \\ \dot{a}_{-1/2} &= \frac{i}{2} (\omega_1 e^{i\omega t} a_{1/2} + \omega_0 a_{-1/2}); \end{aligned} \right\} \tag{A18}$$

substituting

$$\left.\begin{aligned} a_{1/2} &= A_{1/2}(t)\, e^{\frac{-i\omega_0 t}{2}}, \\ a_{-1/2} &= A_{-1/2}(t)\, e^{\frac{i\omega_0 t}{2}} \end{aligned}\right\} \text{ into Eq. (A18)} \qquad \text{(A19)}$$

results in

$$\dot{A}_{1/2} = (i/2)\omega_1 e^{-i(\omega-\omega_0)t} \; A_{-1/2}, \qquad \text{(A20)}$$

$$\dot{A}_{-1/2} = (i/2)\omega_1 e^{i(\omega-\omega_0)t} \; A_{1/2}. \qquad \text{(A21)}$$

$A_{1/2}$ may be solved for by substituting $A_{1/2} = e^{nt}$ in the second derivative of Eq. (A20) and solving the indicial equation for n.

The result is

$$A_{1/2}(t) = C_+ e^{-i\left(\frac{\omega-\omega_0}{2}\right)t + (i/2)\sqrt{\omega_1{}^2 + (\omega-\omega_0)^2}\; t} \qquad \text{(A22)}$$

$$+ C_- e^{-i\left(\frac{\omega-\omega_0}{2}\right)t - (i/2)\sqrt{\omega_1{}^2 + (\omega-\omega_0)^2}\; t} \quad .$$

One may evaluate C_+ and C_- by recalling that at $t = 0$, $A_{1/2} = 1$, $A_{-1/2} = 0$, and therefore $C_+ + C_- = 1$ and $\dot{A}_{1/2}(t = 0) = 0$.

The result is

$$\left.\begin{aligned} C_+ &= 1/2 \left(1 + \frac{\omega - \omega_0}{\sqrt{\omega_1{}^2 + (\omega-\omega_0)^2}}\right) \\ C_- &= 1/2 \left(1 - \frac{\omega - \omega_0}{\omega_1{}^2 + (\omega-\omega_0)^2}\right) \quad . \end{aligned}\right. \qquad \text{(A23)}$$

Putting Eqs. (A22) and (A23) into (A19) results, after some manipulation, in

$$\left| a_{1/2} \right|^2 = 1 - \frac{\omega_1^2}{\omega_1^2 + (\omega_0 - \omega)^2} \sin^2 \left[\frac{\sqrt{\omega_1^2 + (\omega_0 - \omega)^2}\, t}{2} \right],$$

(A24)

$$\left| a_{-1/2} \right|^2 = \frac{\omega_1^2}{\omega_1^2 + (\omega_0 - \omega)^2} \sin^2 \left[\frac{\sqrt{\omega_1^2 + (\omega_0 - \omega)^2}\, t}{2} \right].$$

It may be observed by comparing Eqs. (A10) and (A24), that the classical and quantum-mechanical methods yield the same results.

The progression of the probabilities as the resonance condition $\omega = \omega_0$ is approached is presented in Fig. A21. In Fig. A21a, the frequency ω is far off resonance, and it can be seen that the probability of the spin's starting and remaining in the spin-up state is unity (shown by the dotted line). Of course then the probability of the spin's starting in the spin-up state and ending in the spin-down state is 0 (represented by the solid line).

The probabilities for I arbitrary were first calculated by Majorana.[43]

Equations (A10) are not applicable as such to the beam of atoms effusing from the oven. To make them so, the probabilities must be averaged over the velocity distribution of atoms in the beam. This distribution is written as

$$I(v) = 2I_0 \left(\frac{m}{2kT} \right)^2 v^3 e^{\frac{-mv^2}{2kT}}, \tag{A25}$$

where I(v) is the intensity of atoms with velocity v and I_0 is the full beam intensity,

$$I_0 = \int_0^\infty I(v)\, dv. \tag{A26}$$

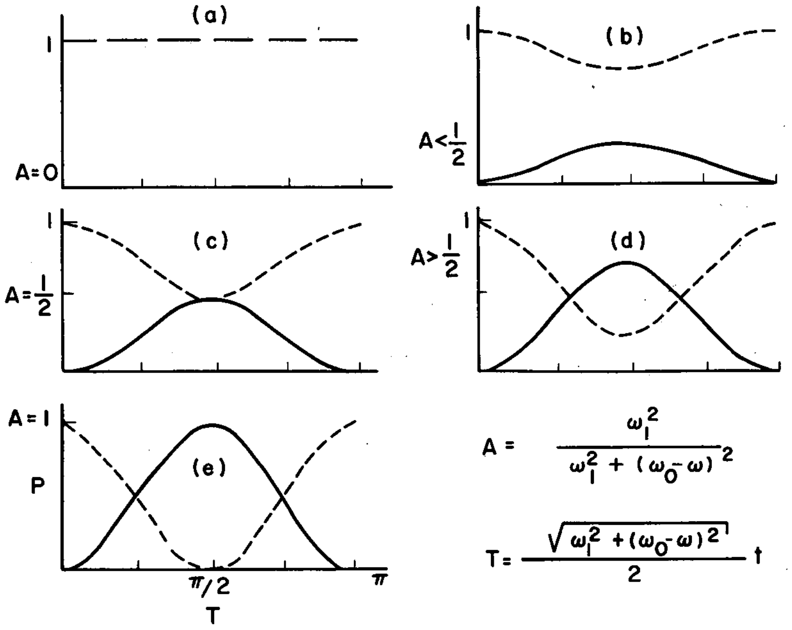

MU-17256

Fig. A21. Transition probabilities as the resonance condition is approached. The dotted curve represents the probability of the spin's starting in the spin-up state and remaining in the spin-up state after a time t The solid curve represents the probability of the spin starting in the spin up state and ending in the spin down state after a time t.

From Eqs. (A7) and (A10) we have

$$P_{1/2,\,-1/2} = \sin^2\theta \, \sin^2\left(\frac{a\,\ell}{2\,v}\right) , \tag{A27}$$

where ℓ is the effective length of the oscillatory field region. Therefore

$$P_{1/2,\,-1/2} = \int_0^\infty 2I_0 \left(\frac{m}{2kT}\right)^2 v^3 \, e^{-\frac{mv^2}{2kT}} \sin^2\theta \, \sin^2\left(\frac{a\,\ell}{2\,v}\right) dv \quad . \tag{A28}$$

Letting $\alpha = \sqrt{\frac{2kT}{m}}$ and $y = \frac{v}{\alpha}$, one may integrate Eq. (A28) to yield

$$P_{1/2,\,-1/2} = I_0 \sin^2\left\{ \theta \left[1/2 - I(x) \right] \right\} , \tag{A29}$$

where

$$I(x) = \int_0^\infty y^3 e^{-y^2} \cos\left(\frac{x}{y}\right) dy \tag{A30}$$

and $x = \frac{a\ell}{\alpha}$.

A table of I(x) may be found in Ramsey.[1] Figure A22 computed from that table, shows that there is an optimum value of field for which the probability of a transition is a maximum. For the theory and similar curves for $I > 1/2$, the reader is referred to the thesis of R. Marrus.[44]

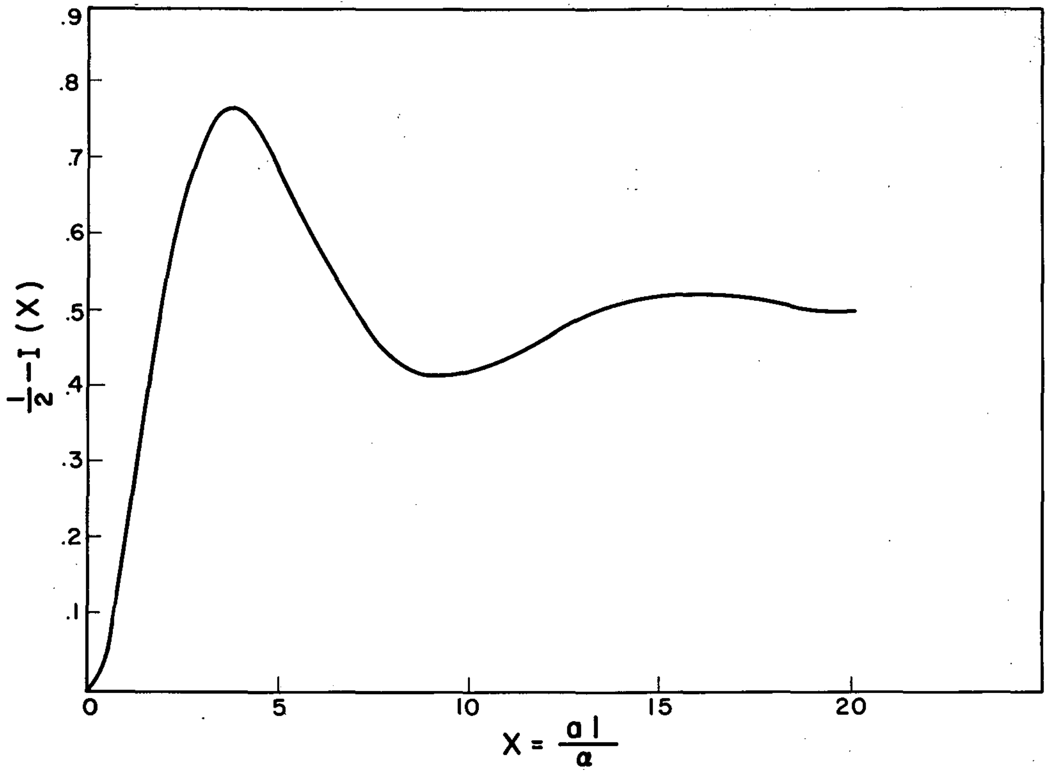

MU-17242

Fig. A22. Transition probabilities as a function of magnetic field.

References

1. N. F. Ramsey, Molecular Beams (Oxford, Clarendon Press, 1956.
2. W. A. Nierenberg (Univ. of Calif.), private communication.
3. W. A. Nierenberg, A Method for Minimizing a Function of *n* Variables, UCRL-3816, June 1957.
4. M. G. Mayer and J. H. D. Jensen, Elementary Theory of Nuclear Shell Structure (John Wiley and Sons, Inc. New York, 1955).
5. E. Feenberg, Shell Theory of the Nucleus (Princeton University Press, Princeton, 1955).
6. H. A. Shugart, The Nuclear Spins, Hyperfine-structure Separations, and Magnetic Moments of Cs^{127}, Cs^{129}, Cs^{130}, and Cs^{132} (Thesis), UCRL-3770, May 1957.
7. R. J. Sunderland, The Nuclear Spins of Rb^{82}, Rb^{83}, and Rb^{84} (Thesis) Univ. of Calif., June 1956.
8. N. F. Ramsey, Nuclear Moments (John Wiley and Sons, Inc., New York (1953).
9. R. S. Krishnan and E. A. Nahum, Proc. Cambridge Phil. Soc. 36, 490 (1940).
10. Strominger, Hollander, and Seaborg, Revs. Modern Phys. 30, 585 (1958).
11. D. E. Alburger and M. H. L. Pryce, Phys. Rev. 95, 1482 (1954).
12. H. J. S. Sand, Analyst 55, 309-312, 1930.
13. K. F. Smith, Second Brookhaven Conference on Molecular Beams, 1956.
14. S. Wahlborn, Nuclear Physics 3, 644-648 (1957).
15. I. Lindgren and C. M. Johansson, Third Brookhaven Conference on Molecular Beams, 1957.
16. Marino, Ewbank, Nierenberg, Shugart, and Silsbee, Bull. Am. Phys. Soc., Ser II, 2, 383 (1957).
17. C. J. Herrlander and T. R. Gerholm, Nuclear Phys. 3, 161 (1957).
18. H. M. Neumann and I. Perlman, Phys. Rev. 78, 191 (1950).
19. H. C. Martin and B. C. Diven, Phys. Rev. 86, 565 (1952).
20. C. J. Herrlander and T. R. Gerholm, Nuclear Phys. 3, 161 (1957).

21. Bergkvist, Bergstrom, Herrlander, Hultberg, Slatis, Sokolowski, Wapstra, and Wiedling, Phil. Mag. 46, 61, 65 (1955).
22. Bergstrom, Hill, and de Pasquali, Phys. Rev. 92, 918 (1953).
23. Kramer, Hamers, and Meijer, Physica 22,208 (1956).
24. Marino, Brink, Ewbank, Shugart, and Silsbee, Bull. Am. Phys. Soc. Ser. II, 3, 186 (1958).
25. Marino, Ewbank, Shugart, and Silsbee, Bull. Am. Phys. Soc. Ser. II, 3, 319 (1958).
26. Brink, Hubbs, Nierenberg, and Worcester, Phys. Rev. 107, 189 (1957).
27. Lindgren, Johansson, and Axensten, Phys. Rev. Lett. 1, No. 12, 473 (1958).
28. E. C. Mallory and M. L. Pool, Phys. Rev. 76, 1454 (1949.
29. C. L. McGinnis, Phys. Rev. 81, 734 (1951).
30. A. Maier and K. P. Meyer, Helv. Phys. Acta 30, 611 (1957).
31. M. D. Petroff, Bull. Am. Phys. Soc. Ser. II, 1, 389 (1956); Radioactivity of Indium-109 and Tin-109 (Thesis), UCRL-3538, Oct. 1956.
32. Bleuler, Blue, Chowdary, Johnson, and Tendam, Phys. Rev. 90, 464 (1953).
33. M. Goldhaber and R. D. Hill, Revs. Modern Phys. 24, 179 (1952).
34. C. L. McGinnis, Phys. Rev. 83, 686 (1951).
35. N. Taub and P. Kusch, Phys. Rev. 75, 1481 (1949).
36. P. Kusch and H. M. Foley, Phys. Rev. 74, 250 (1948).
37. A. K. Mann and P. Kusch, Phys. Rev. 77, 427 (1950).
38. Marino, Ewbank, Nierenberg, Shugart, and Silsbee, Phys. Rev. 111, 286 (1958).
39. L. S. Goodman and S. Wexler, Phys. Rev. 100, 1245 (1955); 100, 1796 (1955); 108, 1524 (1957).
40. P. B. Nutter, Phil. Mag. 1, 587 (1956).
41. T. G. Eck, P. Kusch, Phys. Rev. 106, 958 (1957).
42. Davis, Feld, Zabel, and Zacharias, Phys. Rev. 76, 1076 (1949).
43. E. Majorana, Nuovo cimento 9, 43, (1932).
44. Richard Marrus, Hyperfine Structure Investigations of Some Transuranium Elements (Thesis) UCRL-8547, Nov. 1958.